ENGINEERING RESEARCH AND INNOVATIONS

Table of Contents

CHAPTER 1

Advanced Materials Engineering

Effect of Temperature and Heating Time on Conventional Pyrolysis of Fresh Fruit Bunch (FFB)

Effect Of Activated Carbon & Metal Susceptor on Microwave Pyrolysis of Empty Fruit Bunch

Developing Carbon Capture Material from Polymer

Effect Of Activated Carbon on Microwave Pyrolysis of Fresh Fruit Bunch

Fouling Mitigation of Calcium Carbonate on Heat Exchangers Using C-GNP/C-MWCNT Hybrid Nanofluid

Zeolite-Supported Alkali and Alkali Earth Metal Oxides for CO_2 Capture

Preface

The global pursuit of sustainable development, efficient energy use, and climate change mitigation drives innovation in material science and engineering. This compilation of studies exemplifies diverse approaches to addressing environmental and industrial challenges, providing new insights into biomass valorization, carbon capture, and energy efficiency. The first study investigates the pyrolysis of fresh fruit bunches (FFB), a byproduct of Malaysia's palm oil industry, to produce biochar and bio-oil. By examining the effects of temperature and heating duration on the pyrolysis process, the research offers a pathway for converting agricultural waste into valuable biofuels, contributing to cleaner energy alternatives and waste management strategies. In the second study, the focus shifts to microwave pyrolysis of empty fruit bunches (EFB). By optimizing power settings, material ratios, and other parameters, the research demonstrates how microwave pyrolysis can enhance carbon yields and calorific values, paving the way for more efficient and scalable biochar production methods. The third study takes on the challenge of carbon dioxide emissions by developing polymer-based composite membranes for carbon capture. Using a blend of polyvinyl alcohol (PVA) and polysulfone (PSF), the research highlights significant advances in CO_2 separation efficiency, emphasizing the role of innovative materials in tackling climate change. The fourth study continues the exploration of pyrolysis, analyzing the effects of microwave power and material mixtures on the yield and properties of bio-oil and biochar. By leveraging techniques such as FTIR and SEM, the research contributes to a deeper understanding of how process parameters influence product quality, advancing renewable energy solutions. Fouling in heat exchangers, a common industrial issue, is the subject of the fifth study. By introducing a hybrid nanofluid of clove-functionalized graphene nanoplatelets and carbon nanotubes, the research presents a novel solution to reduce calcium carbonate deposition, enhancing heat transfer efficiency without compromising environmental safety. Finally, the sixth study tackles the critical issue of CO_2 capture using zeolite-supported alkali earth metal oxides. Against the backdrop of escalating global temperatures and environmental degradation, this research explores the potential of adsorbents to sequester carbon effectively, highlighting the urgency of developing scalable and sustainable carbon capture technologies. Each of these studies exemplifies the ingenuity and determination of researchers striving to address pressing environmental and industrial challenges. Together, they underscore the transformative potential of scientific innovation in creating a cleaner, more sustainable future.

EFFECT OF TEMPERATURE AND HEATING TIME ON CONVENTIONAL PYROLYSIS OF FRESH FRUIT BUNCH (FFB)

Abstract: Malaysia, a leading palm oil exporter, supplies major buyers such as China, India, and the European Union. This study investigates the pyrolysis of fresh fruit bunches (FFB), a thermochemical process that converts biomass into biofuels, focusing on the effects of temperature and heating time on the resulting biochar and bio-oil. Fresh fruits from a Malaysian plantation were processed by separating the mesocarp fiber from the kernel and then shredding them for pyrolysis. The experiment was conducted at 200°C, 300°C, 400°C and 500°C for 30, 60 and 90 minutes with a heating rate of 10°C per second. The produced biochar and bio-oil underwent material characterization using a bomb calorimeter, Scanning Electron Microscopic (SEM) and Fourier-Transform Infrared Spectroscopy (FTIR), respectively.

1. Research Background

Malaysia is one of the world's largest palm oil exporters, with major consumers including China, India, and the European Union. In 2018, Malaysia accounted for 33% of global crude palm oil exports and 28% of its production. The oil palm tree was introduced to Malaysia by British colonizers in the 1870s as an ornamental plant from West Africa. Since the 1960s, efforts to reduce dependence on tin and rubber have led to the growth of oil palm cultivation, making it a major commodity in Malaysia. By 2017, Malaysia had about 5.8 million hectares of oil palm plantations, producing approximately 23 million tons of crude palm oil and 2.5 million tons of palm kernel oil annually. Under the Third Industrial Master Plan (2006-2020), the focus is on developing oleochemicals, biodiesel, bio-products, and biogas, and exploring new markets for Malaysian palm oil.

The fruit's pulp consists of the exocarp and mesocarp, containing palm oil, while the central nut includes the shell (endocarp) and an edible kernel with palm kernel oil. Both oils are significant in global trade. There are three primary varieties of oil palm: Dura, Pisifera, and Tenera. Only Dura and Tenera fruits are processed into the two edible oils, as Pisifera fruits lack a shell and are not commercially viable. Dura fruits have a pulp content of 35-55%, with kernels making up 7-20% of the fruit weight, and thick shells (2-8 mm). Pisifera, with high female sterility, is not used commercially. Tenera fruits have a pulp content of 55-96% and are identified by a distinct fiber ring near the shell when cut transversely. The Tenera shell is 0.5-4 mm thick, and the kernel makes up 3-15% of the fruit weight. Due to its high palm oil content, Tenera is preferred for industrial and commercial applications and is widely adopted by farmers.

2. Methodology

2.1 Sample Preparation

The fresh fruit bunches (FFB) were labeled as raw sample material for the experiment. Purchased from a reputable supplier on Shopee, the FFB were at peak ripeness, ensuring high quality for the finished goods. The loose FFB, recently harvested, were divided into ripe and overripe groups. They were cleaned with a towel to remove visible contaminants. Approximately 1.5 kg of ripe FFB were gathered for this semester's experiment. The mesocarp fiber (flesh) of the FFB was separated from the kernel and

shell, then crushed into smaller pieces. The sample was placed inside an alumina boat and weighed using an electric balance, recording a weight.

2.2 Product Collection

In general, pyrolysis yielded three distinct products: biogas, bio-oil, and char. However, in the experiment, primary product that has to be collected is the bio-oil, biochar is the byproduct and syngas would not be collected. The bio-oil gathered in the conical flask was pour into sampling bottle once the experiment was completed. After that, the generated bio-oil is weight was measured, tagged, and stored for characterization. The biochar also being collected from the alumina boat and transfer into another sampling bottle. After that, the weight of the biochar and bio-oil formed was noted and stored for material characterisation.

2.3 Material Characterisation

The collected bio-oil would then be submitted for characterization using Fourier-transform infrared spectroscopy (FTIR) to determine their chemical composition and properties. The characterization of the biochar would involve the use of a Scanning Electron Microscope (SEM) and Energy-dispersive X-ray spectroscopy (EDX) to look at its surface composition and structure. The calorific value of the biochar and bio-oil would be using a bomb calorimeter.

3. Results and Discussions

3.1 Collection of biochar and bio-oil

3.2 Product Yield

Table 1: Yield percentage of Biochar and Bio-oil

Temperature (°C)	Heating time (min)	Biochar production (%)	Bio-oil production (%)
200	30	77.53	0.00
	60	76.53	0.00
	90	68.49	0.00
300	30	53.41	14.73
	60	54.55	17.20
	90	56.32	16.95
400	30	37.16	18.16
	60	44.87	15.95
	90	44.80	14.70
500	30	43.93	14.86
	60	41.28	19.24
	90	41.74	14.38

3.3 Biochar Characterisation

3.3.1 Bomb Calorimeter

2: Calorific Value of Biochar For Different Time Taken and Temperature

Temperature (°C)	Heating time	Biochar production
200		
300		
400		
500		

3.3.2 SEM and EDX Analysis

The SEM image of biochar produced shows a highly porous structure with cavities and channels, typical of pyrolyzed biochar. This structure results from the volatilization of organic compounds during pyrolysis, leaving a carbon-rich matrix with a large surface area, which is beneficial for applications in adsorption, soil amendment, and catalysis. Energy Dispersive X-ray Spectroscopy (EDX) complements SEM by providing the biochar's elemental composition. EDX reveals a high carbon content, indicating successful carbonization, along with oxygen from partial oxidation and functional groups like hydroxyls, carbonyls, and carboxyls. Inorganic elements such as potassium, calcium, magnesium, phosphorus, and silicon, originating from the biomass, are also present, influencing the biochar's pH, nutrient content, and catalytic properties.

The pyrolysis process at 500°C involves dehydration, volatilization, and carbonization stages. Dehydration removes water, while volatilization breaks down hemicellulose and some cellulose, releasing

volatile compounds and leaving a carbon-rich solid.

The variations in carbon, boron, and oxygen content in biochar at different temperatures are due to the effects of pyrolysis on the fresh fruit bunches. At lower temperatures (e.g., 200°C), pyrolysis is incomplete, leaving significant amounts of original organic compounds, resulting in lower carbon content. Higher temperatures (400°C to 500°C) lead to more thorough decomposition, driving off volatiles and increasing carbon concentration. Oxygen content decreases with increasing temperatures as oxygen-containing functional groups are broken down and volatilized, forming more stable carbon structures.

3.4 Bio-oil Characterisation

3.4.1 FTIR Analysis

The FTIR spectrum of bio-oil from pyrolyzed Fresh Fruit Bunches (FFB) reveals its chemical composition by identifying functional groups. A broad peak around 3400 cm^{-1} indicates hydroxyl groups, suggesting alcohols and phenols. Peaks around 2900 cm^{-1} correspond to C-H stretching, showing the presence of alkanes. A prominent peak near 1700 cm^{-1} signifies carbonyl groups, indicating compounds like ketones, aldehydes, carboxylic acids, or esters, common in bio-oils from the breakdown of cellulose and hemicellulose. Peaks between 1600 cm^{-1} and 1500 cm^{-1} indicate C=C stretching, suggesting unsaturated hydrocarbons and aromatic compounds from lignin degradation. Peaks between 1250 cm^{-1} and 1000 cm^{-1} indicate C-O stretching, pointing to ethers, alcohols, esters, or carboxylic acids. Thus, the bio-oil contains a mix of hydroxyl groups, saturated hydrocarbons, carbonyl compounds, unsaturated hydrocarbons, aromatic compounds, and various oxygenated functional groups, typical of biomass pyrolysis products.

4. Conclusions

Both temperature and heating time significantly influence the calorific value of biochar from FFB pyrolysis. Higher temperatures generally improve the calorific value by enhancing carbon content and reducing volatile matter. However, there is an optimal heating time (typically around 60 minutes for higher temperatures), beyond which the calorific value declines due to over-carbonization or increased ash formation. These insights are essential for optimizing pyrolysis conditions to produce high-quality, energy-dense biochar. The pyrolysis of FFB at higher temperatures and optimal durations substantially enhances the calorific value of the resultant biochar, far exceeding the energy content of raw biomass types.

The FTIR spectrum indicates that the bio-oil from the pyrolysis of FFB contains a complex mixture of hydrocarbons and oxygenated compounds. The presence of O-H, C-H, C=O, C=C, and C-O groups suggests a diverse composition with potential applications in various chemical industries

References

1. Idris, S. S., Rahman, N. A., Ismail, K., Mohammed, Yunus, M. F., & Mohd Hakimi, N.N. (2022). Microwave-Assisted Pyrolysis of Oil Palm Biomass: Multi-Optimisation of Solid Char Yield and Its Calorific Value Using Response Surface Methodology. Frontiers in Chemical Engineering. 10.3389/fceng.2022.864589

2. Li, Y., Zhang, G., Liu, J., Li, G., & Wang, Y. (2023). Optimized preparation of multi-matrix activated carbon for CO2 capture by response surface methodology: The advantages of co- pyrolysis of biomass and plastics. Journal of the Energy Institute, 111, 101415. https://doi.org/10.1016/j.joei.2023.1014 15

EFFECT OF ACTIVATED CARBON & METAL SUSCEPTOR ON MICROWAVE PYROLYSIS OF EMPTY FRUIT BUNCH

Abstract: This study investigates the effects of microwave power, heating time, and material ratios on carbon yield during the microwave pyrolysis of Empty Fruit Bunches (EFB). Results showed that 300W microwave power achieved a 30.37% carbon yield, while increasing activated carbon from 5g to 15g enhanced yield, peaking at 37.40%. Optimal conditions for EFB content (4g) and metal susceptor length (3cm) produced yields of 58.50% and 27.10%, respectively. Calorific value and pore diameter analyses identified the highest values at 28.369 kJ/kg and 8.564 µm. EDX analysis confirmed varying carbon percentages, underscoring effective carbonization. This study highlights optimal conditions for efficient biochar production using microwave pyrolysis.

1. Research Background

1.1 Introduction

This research focuses on using microwave pyrolysis to convert Empty Fruit Bunches (EFB) into biochar, managing palm oil waste and contributing to renewable energy. The study aims to optimize parameters affecting carbon yield, calorific value, and biochar pore structure to enhance biomass conversion efficiency [3].

1.2 Background of the Material Used

EFB, a fibrous palm oil industry byproduct, is rich in carbon but poses environmental challenges when discarded. Pyrolyzing EFB into biochar addresses these issues and provides valuable agricultural and energy applications. Activated carbon, with its high porosity, enhances carbon yield and biochar's structural properties [6]. Metal susceptors absorb microwave energy, converting it into heat to efficiently achieve desired pyrolysis temperatures [11]. This study examines the impact of different metal susceptorlengths on pyrolysis efficiency.

1.3 Analysis Methods Microwave

Pyrolysis uses microwave energy to heat biomass in the absence of oxygen, offering faster and more uniform heating than conventional methods. Biochar's energy content was measured using a bomb calorimeter, with higher calorific values indicating better energy efficiency. Scanning Electron Microscopy (SEM) analyzed the biochar's pore structure, providing images of surface morphology and average pore diameter, which are crucial for adsorption and filtration applications. EDX determined the carbon content, providing essential data on the biochar's quality and effectiveness.

2. Methodology

Experimental Setup: A modified microwave oven (2.45 GHz) was used with nitrogen gas to create an inert atmosphere. Two experimental phases were conducted: Phase 1: Varying microwave power (100W and 300W) with fixed material ratios (1g EFB, 1g activated carbon, 5cm metal susceptor). Phase 2: Using 300W power, varying EFB, activated carbon, and metal susceptor lengths (refer to Tables 3.1, 3.2, and 3.3). All experiments maintained a 10- minute carbonization time, with materials placed in an alumina boat to prevent glassware breakage. This structured approach ensured thorough investigation of optimal conditions for carbonization.

Table 3.1 Activated Carbon as Manipulated Variable

Sample	Empty Fruit Bunch (g)	Activated Carbon (g)	Metal Susceptor (cm)
A	2	5	5
B	2	10	5
C	2	15	5

Table 3.2 Empty Fruit Bunch as Manipulated Variable

Sample	Empty Fruit Bunch (g)	Activated Carbon (g)	Metal Susceptor (cm)
B	2	10	5
E	4	10	5
F	6	10	5
G	8	10	5

Table 3.3 Metal Susceptor as Manipulated Variable

Sample	Empty Fruit Bunch (g)	Activated Carbon (g)	Metal Susceptor (cm)
H	2	10	1
I	2	10	3
B	2	10	5
J	2	10	7

3. Results and Discussions

The findings revealed that microwave power significantly influenced carbon yield, with 300W resulting in a 30.37% yield (Figure 4.1), providing the requisite temperature for effective pyrolysis. Increasing activated carbon amounts (up to 15g) improved carbon yield, with sample C reaching 37.40% (Figure 4.6), attributed to enhanced surface area and heat distribution. Optimal EFB content at 4g yielded 58.50% (Figure 4.6), ensuring sufficient biomass without overwhelming the system. A metal susceptor length of 3cm was found to be the most effective, as seen in sample I with a 27.10% yield (Figure 4.6), ensuring efficient heat absorption and distribution. The calorific value peaked at 28.369 kJ/kg in sample I, highlighting the significance of precise material ratios for high energy content (Figure 4.7). Pore diameter analysis showed that higher activated carbon ratios increased pore size, with sample B having the highest diameter at 8.564 µm (Figure 4.8), attributed to more nucleation sites. EDX results confirmed small change carbon weight percentages, with activated carbon averaging 0.48% to 6.79%, with only one outlier value of 15.9% (Table 4.4).

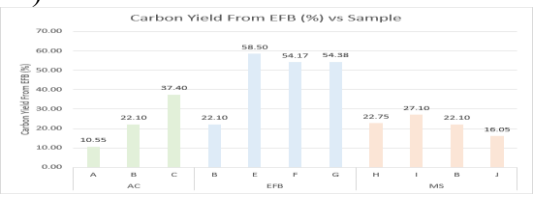

Figure 4.6 Carbon Yield from EFB (%) vs Sample

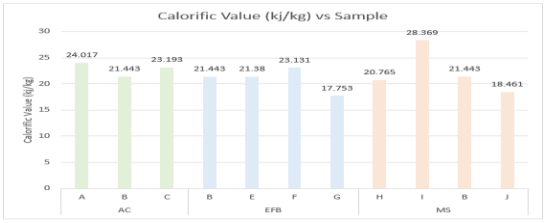

Figure 4.7 Calorific Value (kJ/kg) vs Sample

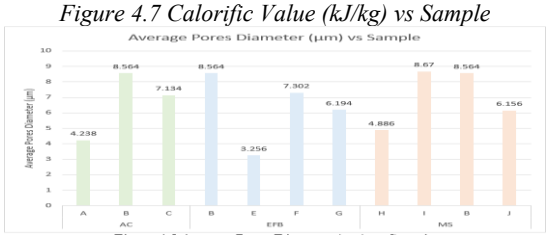

Figure 4.8 Average Pores Diameter (µm) vs Sample

Table 4.4 Average Percentage of Carbon

Variable	Average Weight of Carbon (%)	Percentage Difference (%)
AC	53.90	4.34
		6.79
		0.89
EFB		6.79
		6.33
		4.80
		4.19
MS		0.48
		15.69
		6.79
		5.66

4. Conclusions

The study successfully identified the optimal conditions for maximizing carbon yield and energy content in the microwave pyrolysis of EFB. The findings emphasize the critical roles of microwave power, heating time, and material ratios, contributing to the advancement of sustainable biomass utilization and efficient biochar production

References

1. Rosli, E. N. S. B. E. (2023). Effect of power and heating time on carbonization of empty fruit bunch. University of Malaya.
2. Lee, S. N. Y., & Voon, C. H. (2019). The utilisation of palm oil and oil mill waste. Journal of Oil Palm Research, 31(1), 1-143.
3. Putra, P. H. M., Rozali, S., Patah, M.F. A., & Idris, A. (2022). Microwave Pyrolysis of Polypropylene with Iron Susceptor. Proceedings of TECH POST 2022, Universiti Malaya. AIJR Publisher.

DEVELOPING CARBON CAPTURE MATERIAL FROM POLYMER

Abstract: The increasing levels of carbon dioxide emissions from fossil fuel use pose a significant threat to global climate stability. This study focuses on developing a polymer-based carbon capture material, specifically a composite membrane consisting of polyvinyl alcohol (PVA) and polysulfone (PSF). The synthesis process involved dissolving PVA in deionized water at different concentrations (5 wt%, 10 wt%, and 15 wt%), enhancing hydrophilicity with sodium dodecyl sulfate (SDS), and coating a PSF support layer. Characterization included FTIR spectroscopy, FESEM-EDX, and DSC to assess structural, morphological, and thermal properties. FTIR analysis confirmed successful PVA coating on the PSF substrate. FESEM analysis revealed varied surface morphologies based on PVA concentration, while DSC showed distinct thermal transitions. CO_2 separation tests indicated the formation of bicarbonate groups, with increased CO_2 capture efficiency at higher PVA concentrations, highlighting the potential of PVA/PSF composite membranes for carbon capture applications. The study underscores the promising structural, chemical, and thermal properties of these composite membranes, making them effective materials for reducing carbon emissions.

1. Research Background

Approximately 272.9 million metric tons of carbon dioxide were released into the atmosphere by Malaysia's energy usage in 2022, with coal being the primary source of electricity generation, contributing 76.4 terawatt-hours, followed by natural gas with 68.4 terawatt-hours [1]. This reliance on fossil fuels highlights the urgent need for effective carbon capture and storage (CCS) technologies to mitigate CO_2 emissions and combat climate change.

Various CCS methods have been developed, including chemical absorption, physical adsorption, membrane-based separation, and cryogenic processes. Advanced materials like Metal-Organic Frameworks (MOFs), zeolites, and silica-based materials have demonstrated significant potential in enhancing CO_2 capture efficiency. Among these, composite membranes stand out due to their ability to combine the benefits of different materials [2], offering improved gas separation performance.Composite membranes made from PVA and PSF offer a promising approach for CO_2 capture.

PVA provides hydrophilicity and excellent film-forming properties, while PSF offers thermal stability and mechanical strength [3]. This combination enhances the membrane's selectivity and permeability for CO_2, making it more effective than single-material membranes. The structural, morphological, and thermal properties of these membranes are critical to their performance and will be thoroughly investigated in this study.

2. Methodology

The thin films were developed using the solution casting method. PSF was dissolved in dimethylformamide to create a slurry, which was then spread onto a petri dish and dried. The dried PSF layer was washed with warm tap water and deionized water.

PVA powder was dissolved in deionized water at concentrations of 5 wt%, 10 wt%, and 15 wt%, with Sodium Dodecyl Sulfate (SDS) added to improve hydrophilicity. The PSF support layer was coated with PVA by immersing it in the PVA solution,

removing excess solution and drying it in an oven at 45°C overnight.

Characterization included Fourier Transform Infrared (FTIR) spectroscopy to confirm functional groups, Field Emission Scanning Electron Microscopy with Energy Dispersive X-ray (FESEM-EDX) to examine surface morphology, and Differential Scanning Calorimetry (DSC) to study thermal properties.

The membrane's performance for CO_2 separation was tested in a glove box. CO_2 gas was introduced at a controlled flow rate and pressure. FTIR analysis was used again to monitor changes in functional groups after CO_2 exposure.

3. Results and Discussions

The solution casting method was employed to fabricate pure PSF and PVA/PSF composite membranes. Four samples were synthesized: pure PSF, 5 wt%, 10 wt%, and 15 wt%, each cut into a 4 cm diameter circle for uniform surface area.

FESEM analysis revealed that pure PSF membranes exhibited a smooth, uniform surface with consistent micro-scale pores [4]. The 5 wt% PVA/PSF composite membrane showed a generally smooth surface with fewer pores and minimal irregularities, indicating successful coating and good compatibility between PVA and PSF. The 10 wt% PVA/PSF composite membrane demonstrated an even smoother and more uniform surface with further reduced porosity. However, the 15 wt% PVA/PSF composite membrane displayed increased porosity due to phase separation and micro void formation at higher PVA concentrations. Despite this, the overall smoothness and uniformity were maintained.

EDX analysis confirmed the elemental composition of the membranes. Carbon and oxygen were the primary elements, with sodium and sulfur present due to the inclusion of SDS. The introduction of PVA and SDS resulted in slight changes in the elemental composition compared to pure PSF, with higher PVA concentrations showing increased oxygen content.

Table 1: EDX Analysis element percentage

PVA Concentration (wt%)	%wt (percentage by weight)	%at (percentage by atomic composition
0.0	C 80.12% O 19.88%	C 83.59% O 16.41%
5.0	C 72.07% O 19.47% Na 0.50% S 7.96%	C 80.14% O 16.25% Na 0.29% S 3.31%
10.0	C 73.45% O 19.77% Na 0.57% S 6.20%	C 80.79% O 16.33% Na 0.33% S 2.55%
15.0	C 68.68% O 24.93% Na 0.89% S 5.50%	C 76.38% O 21.82% Na 0.52% S 2.29%

DSC analysis indicated distinct thermal transitions. Pure PSF had a glass transition temperature (Tg) of approximately 30.01°C and an endothermic peak at 64.53°C. The Tg values for the composite membranes varied with PVA concentration: 39.01°C for 5 wt%, 31.07°C for 10 wt%, and 34.34°C for 15 wt%. The endothermic peaks at higher temperatures suggested significant thermal relaxation phenomena.

FTIR analysis before CO_2 testing confirmed the presence of characteristic functional groups from both PVA and PSF. After CO_2 exposure, new peaks around 1400 cm^{-1} indicated the formation of bicarbonate groups, showing successful chemical interactions between CO_2 and the composite membrane [5]. The effectiveness of CO_2 capture increased with higher PVA concentrations, as evidenced by more pronounced bicarbonate peaks in the composite membranes compared to pure PSF.

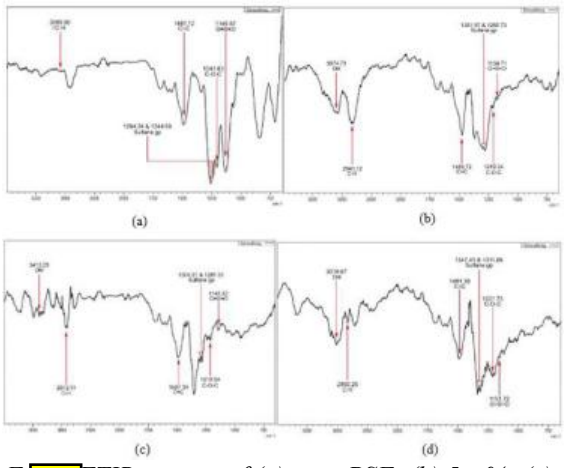

Fig 1: FTIR spectra of (a) pure PSF; (b) 5wt%; (c) 10wt%; (d) 15wt% PVA/PSF before testing

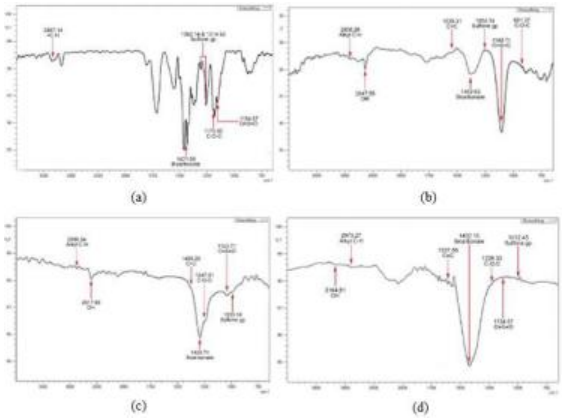

Fig 2: FTIR spectra of (a) pure PSF; (b) 5wt%; (c) 10wt%; (d) 15wt% PVA/PSF after testing

4. Conclusions

This research successfully developed and analyzed pure PSF and PVA/PSF composite membranes using the solution casting method to improve CO_2 capture efficiency. The objectives were achieved by examining the membranes' structure, morphology, and thermal properties. FESEM analysis showed that PVA coating reduced porosity and improved surface smoothness. EDX confirmed the successful integration of PVA and SDS, while DSC indicated thermal changes due to PVA content. FTIR analysis revealed bicarbonate group formation after CO_2 exposure, proving effective CO_2 capture. The study found that higher PVA concentrations increased CO_2 capture efficiency, demonstrating the potential of PVA/PSF composite membranes in carbon capture applications.

References

1. Statista. (2023, September 26). CO2 emissions from energy use in Malaysia 2013-2022. https://www.statista.com/statistics/1394260/malaysia-co2-emissions-from-energy-use/
2. Han, Y., & Ho, W. W. (2018). Recent advances in polymeric membranes for CO2 capture. Chinese Journal of Chemical Engineering, 26(11), 2238–2254. https://doi.org/10.1016/j.cjche.2018.07.010
3. Bleckmann, K. (2021, June 23). Polysulfone Tubing: Versatility based on resistance. PBS Plastics. https://www.pbsplastics.com/polysulfone-tubing-versatility-based-on-resistance/
4. Pandele, A. M., Serbanescu, O. S., & Voicu, S. I. (2020). Polysulfone Composite Membranes with Carbonaceous Structure. Synthesis and Applications. Coatings, 10(7), 609. https://doi.org/10.3390/coatings10070609
5. Liu, M., Nothling, M. D., Zhang, S., Fu, Q., & Qiao, G. G. (2022). Thin film composite membranes for postcombustion carbon capture: Polymers and beyond. Progress in Polymer Science, 126, 101504. https://doi.org/10.1016/j.progpolymsci.2022.101504

EFFECT OF ACTIVATED CARBON ON MICROWAVE PYROLYSIS OF FRESH FRUIT BUNCH

Abstract: This study explores the effects of varying microwave power settings and different mixture ratios of palm oil fruit to activated carbon on the pyrolysis process and resultant bio-oil and biochar yields. The objective is to analyze the characteristics of bio-oil and biochar produced using FTIR, SEM, and EDS. It investigates how activated carbon impacts heating efficiency and yield content. Fresh palm fruit was procured online, and activated carbon was obtained from a local fish shop. The materials were prepared by removing the nut from the fresh fruit, meshing it into smaller pieces, grinding the activated carbon, and mixing both at fixed ratios. The parameters set were 350W, 450W, and 550W; mixture ratios of 7:3, 8:2, and 9:1; and a heating time of 30 minutes. Results show that bio-oil yield increases with power and a constant 8:2 mixture ratio. FTIR analysis indicates similar bio-oil content across settings, and SEM/EDS analysis shows increased carbon content in biochar with power.

1. Research Background

The oil palm industry is a significant contributor to the global economy, especially in regions like Southeast Asia [1]. With the increasing demand for sustainable and efficient energy sources, the conversion of biomass into biofuels through processes such as pyrolysis has gained attention. This research focuses on the microwave pyrolysis [2] of fresh fruit bunches (FFB) from palm oil to produce bio-oil and biochar, with an emphasis on the role of activated carbon in enhancing the efficiency and yield of the process. The use of activated carbon as a microwave absorber aims to optimize the pyrolysis conditions and improve the quality of the bio-oil and biochar produced.

2. Methodology

The experiment involved preparing the materials by removing the nuts from the palm fruits, slicing the flesh into small pieces, and grinding activated carbon into fine particles. The palm fruit and activated carbon were then mixed in ratios of 7:3, 8:2, and 9:1. The mixture was placed in a microwave pyrolysis reactor as shown in Figure 1.1 and was subjected to microwave pyrolysis at power settings of 350W, 450W, and 550W for 30 minutes.

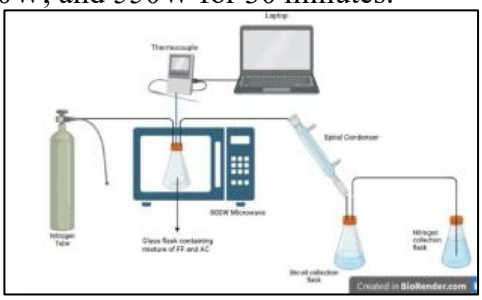

Figure 1 Schematic diagram of experimental set up

The bio-oil was analyzed using Fourier Transform Infrared Spectroscopy (FTIR) to identify its chemical composition by the presence of various functional groups in the bio-oil. The biochar was analyzed using Scanning Electron Microscopy (SEM) to determine its structural through imaging and Energy Dispersive X-ray Spectroscopy (EDS) to identify its elemental composition.

3. Results and Discussions

3.1 Product yield

The pyrolysis process produces three main products: biochar (solid phase), bio-oil (liquid phase), and syngas (gas phase).

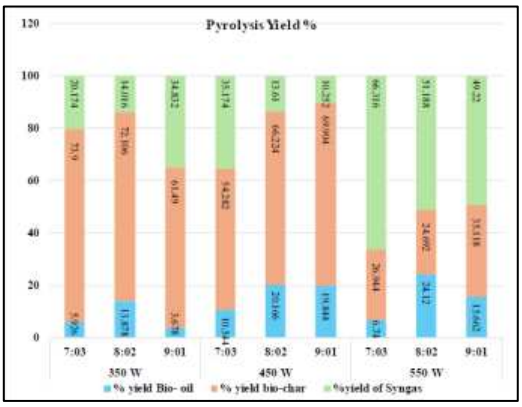

Figure 2 Percentage yield across all parameters

Figure 2 shows the bio-oil yield from microwave pyrolysis at various ratios and power levels, with the highest yield of 24.12% at 550W and 8:2 ratio. The yield increased with higher microwave power, with the 8:2 ratio being optimal. These results are similar to Chuayjumnong S[illegible] al. [3], who achieved the highest yield at 500°C with a 7:3 oil palm shell (OPS) to AC ratio. The difference is due to the higher moisture content in fresh palm fruit bunch (FFB) compared to OPS.

3.2 Temperature profile

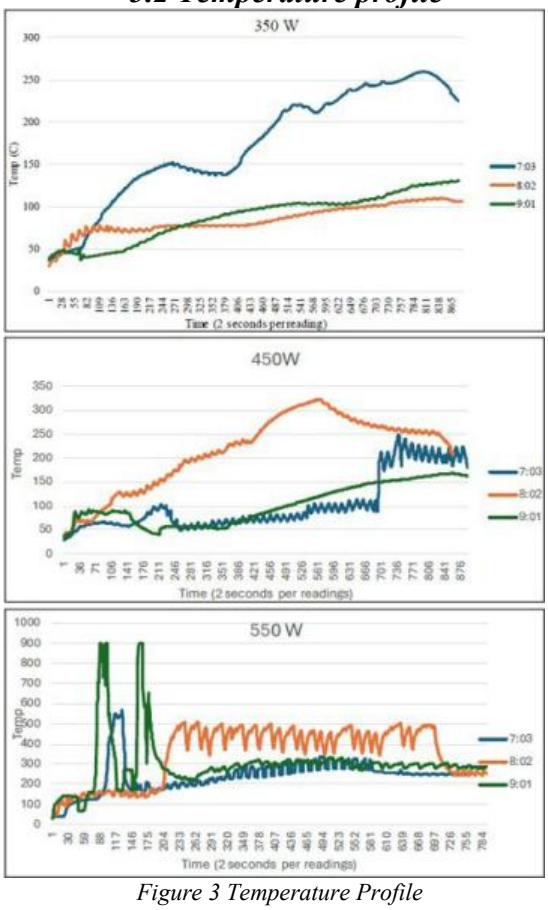

Figure 3 Temperature Profile

One of the aims of this study is to investigate the effect of activated carbon on heating efficiency. The temperature profile during pyrolysis was recorded for each power setting as shown in Figure 3. The 7:3 ratio heats quickly but is unstable, while the 9:1 ratio exhibits extreme, unstable heating, possibly due to inefficient energy absorption. The 8:2 ratio is the most effective for microwave pyrolysis across all power levels, achieving the highest and most stable temperatures.

The profiles showed a consistent rise in temperature with increasing power levels, which correlates with the increased yield of bio-oil as higher temperature facilitated the breakdown of biomass into bio-oil and biochar more efficiently

3.3 Bio-Oil chemical composition (FTIR)

FTIR analysis indicated that the bio-oil contained similar functional groups (O-H, O=C=O, C=C, N-O) across all settings, showing consistent chemical composition. This consistency suggests that the basic chemical structure of the bio-oil is not significantly affected by changes in microwave power or mixture ratios.

Table 1 FTIR peak assignment

Wavenumber [cm^{-1}]	Functional Group	
3800-3584	O-H	Alcohol(free)
3550-3200		Alcohol (intermolecular bonded)
3200-2700		
2400-2000	O=C=O	Carbon dioxide
1662-1626	C=C	Alkene (cis)
1550-1500	N-O	Nitrogen

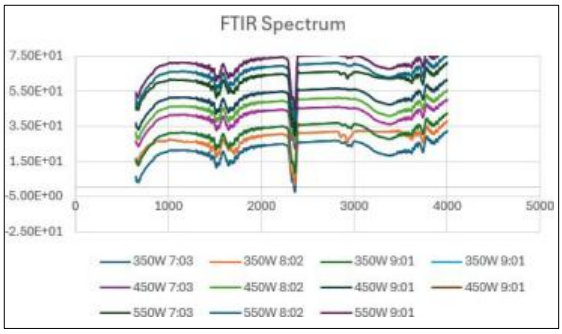

Figure 4 FTIR spectrum

3.4 SEM and DTS analysis

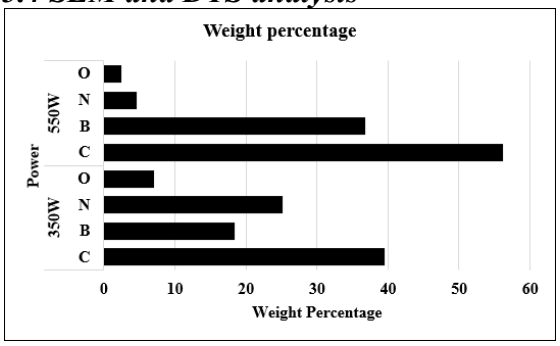

Figure 5 Element weight percentage EDS

Figure 5 above reveals differences in the elemental composition of biochar produced at 350W and 550W, both with an 8:2 ratio of palm oil fruit to activated carbon. The oxygen content is significantly higher in the 350W biochar due to lower pyrolysis temperatures, which are less effective at breaking down oxygen-containing functional groups and can result in incomplete pyrolysis. The nitrogen content is also higher in the 350W biochar because lower temperatures preserve more nitrogen, and the palm oil fruit may not have been as fresh, leading to higher nitrogen content through microbial decomposition. The boron content is much higher in the 550W biochar. Lastly, the carbon content is higher in the 550W biochar due to higher temperatures leading to greater thermal decomposition of volatile compounds, leaving a more carbon-rich residue.

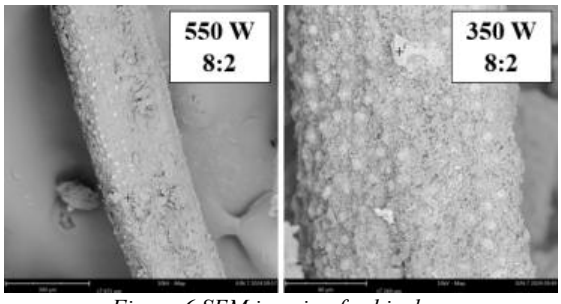

Figure 6 SEM imaging for biochar

4. Conclusions

This study examined the impact of different microwave power settings and palm oil fruit to activated carbon ratios on pyrolysis. The optimal parameters were found to be 550W power and an 8:2 ratio, yielding the highest bio-oil output at 24.12%. This indicates that higher microwave power and the optimal carbon ratio significantly enhance bio-oil production. The 8:2 ratio achieved the most stable and high temperatures across all power levels, and while bio-oil characteristics were similar across settings, EDS analysis revealed significant differences in the elemental composition of biochar produced at different power levels. Thus, activated carbon improves heating efficiency and yield, with the 8:2 ratio and 550W power proving most effective. Activated also influences the composition of the bio-oil and biochar, contributing to higher yields and higher carbon content biochar.

References

1. Tukiran, Z., Husodo, B. T., Susanti, D., & Pambudi, N. A. (2017). Catalytic cracking of palm oil into biofuel using ZSM-5 catalysts: Characterization and catalytic performance. *Indonesian Journal of Chemistry, 17*(1), 57-66. https://doi.org/10.22146/ijc.25460
2. Motasemi, F., & Afzal, M. T. (2013). A review on the microwave-assisted pyrolysis technique. *Renewable and Sustainable Energy Reviews, 28*, 317–330. https://doi.org/10.1016/j.rser.2013.08.008
3. Chuayjumnong, S., Karrila, S., Jumrat, S., & Pianroj, Y. (2020). Activated carbon and palm oil fuel ash as microwave absorbers for microwave-assisted pyrolysis of oil palm shell waste. *RSC Advances, 10*(53), 32058–32068. https://doi.org/10.1039/d0ra04966b

FOULING MITIGATION OF CALCIUM CARBONATE ON HEAT EXCHANGERS USING C-GNP/C-MWCNT HYBRID NANOFLUID

Abstract: Fouling in heat exchangers refers to the accumulation of undesirable materials on heat transfer surfaces, affecting efficiency and requiring maintenance. This study focused on mitigating calcium carbonate fouling in heat exchangers by dispersing hybrid nanofluid consisting of clove-functionalized graphene nanoplatelets (C-GNP) and multi-walled carbon nanotubes (C-MWCNT) to the solution. Unlike previous research using only C-GNP and only C-MWCNT, this study used a hybrid nanofluid to improve heat transfer and reduce $CaCO_3$ deposition and fouling resistance. The experiment simulated fouling by submerging a test section in $CaCO_3$ solution for 72 hours, maintaining fouling concentration with EDTA complex titration. Solutions included untreated $CaCO_3$ at 0.3g/L and treated with 0.0036%, 0.0053%, and 0.0071% weight concentration of C-GNP/C-MWCNT hybrid nanofluid. The deposition is then observed under FESEM, with the temperature measurements used to calculate the fouling resistance and overall heat transfer coefficient. Results showed a 19.33% improvement in mitigating $CaCO_3$ formation without causing corrosion or environmental hazards.

1. Research Background

This study is designed to address the critical issue of fouling of inverse soluble salts in heat exchanger through the addition of ecofriendly additives in the heat transfer. The deposition of the salts results in a substantial decline in overall performance of the heat exchanger, since it increases the heat transfer resistance and reduces the rate of heat transfer.

Hence, this research project seeks to investigate and develop effective strategies for the mitigation of fouling in heat exchangers by employing ecofriendly additives. The rate of formation of undesired materials before and after the addition of the developed ecofriendly additives were analyzed, and comparisons of performance were made between the newly developed ecofriendly additives and the existing fouling additives.

2. Methodology

The experimental setup used as shown in Fig. 1 replicate the heat transfer in a heat exchanger's tubes, where material of SS316L is used for this study. The experiment is conducted for 72 hours, with different weight concentrations of additives being dispersed as the manipulated variable. The temperatures of hot and cold water were kept constant at 60°C and 25°C respectively, with the hot water outlet being measured periodically using the installed thermocouples and data logger.

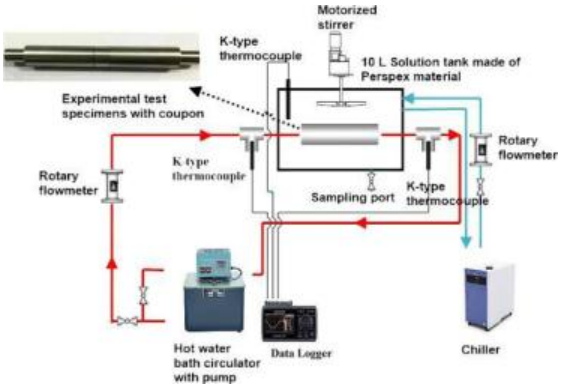

Fig. 1: Schematic diagram for experimental setup [1]

Both of GNP and MWCNT were functionalized by method proposed by previous research [1] as shown in Fig. 2, but with both GNP and MWCNT being sonicated together in the clove extract solution. After the solution was refluxed for 16 hours and dried in the oven for 36 hours, the nanofluid was prepared at weight

concentrations of 0.0036%, 0.0053% and 0.0071%.

Fig. 2: Preparation of C-GNP [1]

To ensure the concentration of the $CaCO_3$ was maintained at 0.3 ± 0.025 g/L, EDTA complex titration is conducted every 6 hours and small amount of calcium carbonate is added to compensate for the reduction in the $CaCO_3$ solution. At the end of each experiment, the test specimen was let dry at room temperature for a day.

The middle part of the test section was used to measure the weight of the $CaCO_3$ deposition with and without the disperse of the additives, whereas the connector part was scanned using FESEM to observe the crystal morphology of the deposits. Using the temperature data over the 72 hours period, we calculated the fouling resistance and heat transfer coefficient, and obtained the fouling curve with and without the disperse of additives.

3. Results and Discussions

As shown in Table 1, we observed a massive reduction in the amount of deposition when dispersing the hybrid C-GNP/C-MWCNT additives, with a trend of decreasing mass of deposits as we increase the weight concentration of the additives.

Table 1: Mass of deposition with untreated and treated solutions

Solution	Mass of $CaCO_3$ deposition (g)	Percentage of reduction in deposition (%)
Untreated	0.1652	-
Treated with 0.0036 wt% additives	0.0787	52.36
Treated with 0.0053 wt% additives	0.0587	64.47
Treated with 0.0071 wt% additives	0.0448	72.88

More interestingly, compared to the C-GNP and C-MWCNT being dispersed as the only additives instead of a hybrid nanofluid, we observed a further reduction up to about 19.3% at weight concentration of 0.0071 wt%. According to research [1], as the concentration of additives is increased, the chance of sequestration of Ca^{2+} is increased. The functionalization process towards GNP and MWCNT using clove also helped to reduce the reactivity of the Ca^{2+}. The presence of carboxylate groups on both C-GNP and C-MWCNT, especially at higher concentrations of the additives, helped to prolong the initiation period of the crystallization fouling due to its ability to absorb the calcium cation.

As for the fouling resistance, we observed a typical fouling curve for inverse soluble salts, where it started with negative fouling resistance, followed by a linear rise and asymptotic trend in alternate, as shown in Fig. 3. This trend was also observed in previous research on C-GNP [1] and C-MWCNT [2]. On the other hand, the fouling resistance with additives dispersed, for all concentrations, were observed to be negligible.

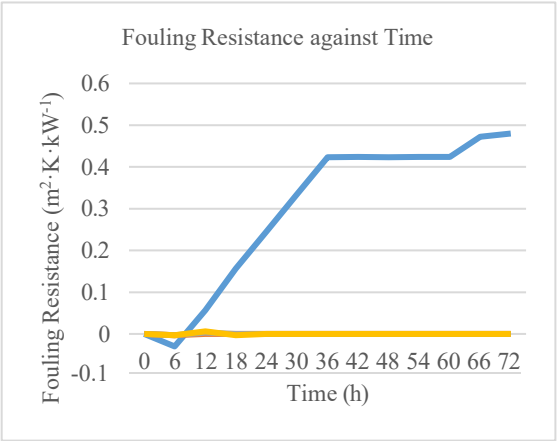

Fig. 3: Graph of fouling resistance against time for different concentrations of C-GNP/C-MWCNT hybrid nanofluid.

On the other hand, we observed a significant improvement in the heat transfer coefficient as shown in Fig. 4, with the 0.0071 wt% concentration achieving the highest heat transfer coefficient. This is because the additives enhanced the Brownian motion of the suspended nanoparticles [1,3], as well as the improvement in thermal conductivity [1].

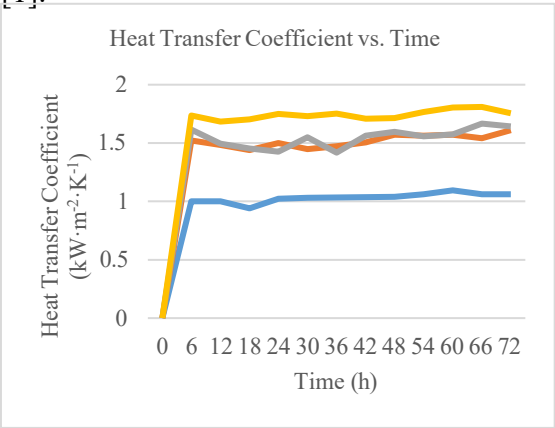

Fig. 4: Graph of heat transfer coefficient over the course of 72 hours of experimentation.

The crystal morphology also showed that the formation of $CaCO_3$ were reduced when the hybrid nanofluid is dispersed as the calcite crystals formed were distorted and irregular in shape, and can be described as amorphous, as shown in Fig. 5, compared to a consistent, orthorhombic shape usually associated with calcite crystals.

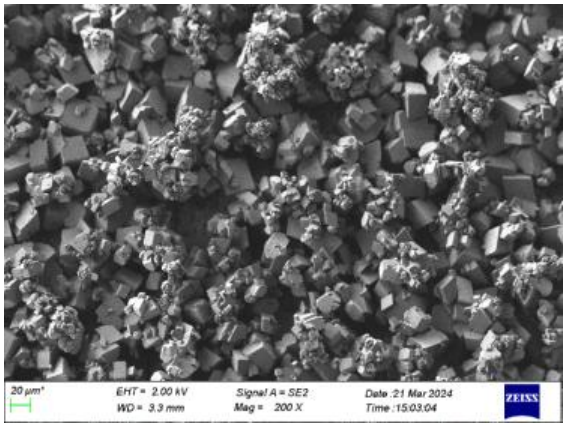

Fig. 5: $CaCO_3$ crystal morphology with 0.0071 wt% of C-GNP/C-MWCNT hybrid nanofluid applied

4. Conclusions

With the C-GNP/C-MWCNT additives being dispersed, fouling resistance was negligible over 72 hours, resulting in a better overall heat transfer coefficient. This means less maintenance and longer operating times. A key part of the research was preventing corrosion on the heat transfer surface to avoid corrosion fouling and additional repair work.

References

1. Shaikh, K., Kazi, S. N., Zubir, M. N. M., Wong, K. H., Khan, W. A., Abdullah, S., Alam, M. S., Keat, S. B., & Fauzi, M. a. Z. I. M. (2023). Improvement of heat transfer and fouling retardation performance of heat exchanger using green functionalized graphene nanoplatelets additives. Journal of the Taiwan Institute of Chemical Engineers, 153, 105227. https://doi.org/10.1016/j.jtice.2023.105227
2. Shaikh, K., Kazi, S. N., Zubir, M. N. M., Wong, K. H., Khan, W. A., Abdullah, S., Alam, M. S., & Keat, S. B. (2023). Retardation of CaCO3 fouling on heat exchanger surface using water-based cloves- functionalized multiwall carbon nanotubes (C-MWCNT) nanofluids. Journal of Thermal Analysis and Calorimetry, 148(22), 12937–12946. https://doi.org/10.1007/s10973-023-12551-0
3. Sadri, R., Hosseini, M., Kazi, S., Bagheri, S., Zubir, N., Solangi, K., Zaharinie, T., & Badarudin, A. (2017). A bio-based, facile approach for the preparation of covalently functionalized carbon nanotubes aqueous suspensions and their potential as heat transfer fluids. Journal of Colloid and Interface Science, 504, 115–123. https://doi.org/10.1016/j.jcis.2017.03.051

ZEOLITE-SUPPORTED ALKALI AND ALKALI EARTH METAL OXIDES FOR CO_2 CAPTURE

Abstract: This study explores the synthesis of zeolite-supported alkali earth metal oxides for CO_2 capture against the backdrop of pressing climate change concerns. The Paris Agreement aims to curb greenhouse gas emissions, yet by 2023, global temperatures had already risen by 1.4°C, posing significant risks to vulnerable regions and ecosystems. Melting polar ice caps, rising sea levels, and extreme weather events threaten ecosystems and human societies. The study synthesized four adsorbents with different MgO/13X ratios, with yields ranging from 67.49% to 89.96%. Characterization via XRF, XRD, and FTIR confirmed successful synthesis. Preliminary CO_2 capture tests for Mg13X-1 and Mg13X-2 showed promising results, although further testing was limited by technical and budgetary constraints. Future work should encompass comprehensive carbon capture performance testing, cyclic stability assessments, and SEM microscopy to ensure complete MgO impregnation into the 13X.

1. Research Background

In recent decades, climate change driven by human activities, such as burning fossil fuels and deforestation, has become a pressing global issue. The Paris Agreement, signed by nations worldwide, aims to curb greenhouse gas emissions and limit global temperature rise to below 2°C, with efforts to cap it at 1.5°C above pre-industrial levels (United Nations, 2023). However, by 2023, global temperatures had already risen by 1.4°C, posing significant risks to vulnerable regions and ecosystems, and atmospheric carbon dioxide levels had increased by 50% since the pre-industrial era by 2022.

The impacts of climate change are far-reaching, affecting ecosystems and human societies worldwide. Melting polar ice caps and glaciers have led to rising sea levels, threatening coastal areas, while extreme weather events like hurricanes, heatwaves, and erratic precipitation patterns are becoming more frequent, causing floods, droughts, and wildfires. These changes disrupt ecosystems, endanger biodiversity, and challenge agricultural systems, thus affecting global food security. Moreover, climate change poses risks to human health, exacerbates social inequalities, and threatens global stability, underscoring the urgent need for collaborative efforts to adapt, mitigate, and build resilience on a global scale.

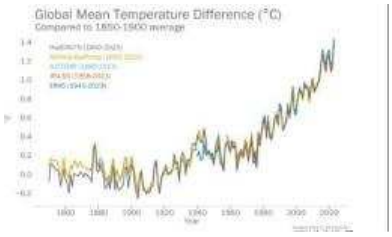

Figure 1. Global Mean Temperature Increase from 1850-1900 (World Meteorological Organization, 2023)

Meeting the goals of the Paris Agreement and keeping global temperature increases below 1.5°C requires more than just cutting greenhouse gas emissions; carbon capture technology is a promising solution (Herzog, 2023). This technology involves capturing carbon dioxide emissions from industrial processes and power plants before they are released into the atmosphere, then storing them underground, a process known as carbon capture and sequestration (CCS). Various forms of carbon capture exist, such as pre-combustion, post-combustion, oxy-

fuel combustion, and direct air capture, offering flexible solutions to reduce emissions from existing infrastructure, support the transition to a low-carbon future, and enhance sustainability in carbon-intensive industries. These technologies play a crucial role in global climate change mitigation efforts.

2. Methodology

The study uses magnesium nitrate, zeolite 13X, and distilled water as materials, and the apparatus includes a beaker, stirrer, hot plate, mortar and pestle, oven, muffle furnace, and thermogravimetric analyzer (TGA). Parameters include active material loading on the zeolite support, activation temperature of the adsorbent, and the operation temperature during the CO_2 capture test. The synthesis procedures involve dissolving magnesium nitrate in heated distilled water, mixing it with crushed zeolite 13X, and evaporating the water before calcining the solid product at 600°C. This process is repeated with varying amounts of magnesium nitrate to produce different samples (Mg13X-1, Mg13X-2, Mg13X-3, Mg13X-4).
Reference samples of zeolite 13X and MgO are also prepared for characterization and performance testing.

Figure 2: Thermogravimetric Analyzer

For the CO_2 capture capacity test, 25mg of the adsorbent is activated in a TGA at 700°C for 10 minutes under a pure nitrogen flow, followed by a carbonation test at 300°C for 30 minutes in a 10% CO_2 atmosphere, with mass observations taken at five-minute intervals.

The characterization of the adsorbent materials involves separating small samples of each finished product, labeling them, and submitting them with the necessary forms for FTIR, XRD, and XRF characterization.

3. Results and Discussions

All synthesized adsorbents have product yields below 90%, with Mg13X-1 yielding 86.24%, Mg13X-2 at 88.12%, Mg13X-3 at 67.49%, and Mg13X-4 at 89.96%. Mg13X-3 has the lowest yield, while Mg13X-4 has the highest. These adsorbents, which appear as a brownish-white powder, can be easily crushed into a fine powder. XRF analysis confirmed that the 13X reference sample is composed of Na_2O, MgO, SiO_2, Al_2O_3, K_2O, TiO_2, and Fe_2O_3, with a purity of 97.28%, suitable for characterizing Mg13X-x adsorbents. The MgO reference sample has an 80.91% purity, validating its use for the synthesized adsorbents. The actual MgO/13X ratios in the synthesized adsorbents deviated from theoretical values: Mg13X-1 had a ratio of 1.3784 (37.84% higher), Mg13X-2 had a ratio of 1.4934 (25.33% lower), Mg13X-3 had a ratio of 4.6827 (56.09% higher), and Mg13X-4 had a ratio of 4.6508 (16.27% higher).

Figure 3: Result of Material Synthesis

The XRD patterns for zeolite 13X and MgO reference samples confirm their identities, closely matching literature patterns with characteristic peaks. The XRD patterns for synthesized adsorbents Mg13X-1 and Mg13X-2 indicate successful synthesis with peaks corresponding to both MgO and zeolite 13X. However, Mg13X-3 and

Mg13X-4 primarily show peaks for MgO, suggesting the possible absence of zeolite 13X and indicating issues with the synthesis process.

The FTIR spectra analysis shows that the reference samples of zeolite 13X and MgO match literature data, validating their use for characterizing synthesized adsorbents. Zeolite 13X exhibits O-H and aluminosilicate group peaks, while MgO displays peaks for O-H, C=O, and Mg-O groups. The FTIR spectra for synthesized adsorbents Mg13X-1, Mg13X-2, Mg13X-3, and Mg13X-4 all indicate the presence of both MgO and zeolite 13X, with characteristic peaks for O-H, aluminosilicate, and Mg-O groups. These results confirm the successful synthesis of the adsorbents, containing the intended components.

Mg13X-1, starting with 21.2 mg, increased by 0.84% to 21.378 mg after a 30-minute test at 300°C, showing the highest mass increase among the adsorbents tested. Mg13X-2, with an initial mass of 62.9 mg, showed a smaller increase of 0.12% to 62.973 mg under the same conditions. Despite the similar absolute mass change, Mg13X-1's higher percentage increase indicates better performance in CO_2 capture relative to its initial mass. Both adsorbents did not reach their maximum adsorption capacities within the test duration.

Several issues arose during the adsorbent synthesis and performance testing. The synthesis process was prolonged due to the extended time required for complete evaporation of distilled water from the $MgNO_3$ solution, taking several days to two weeks at elevated temperatures. Low product yields were another challenge. This low yield is theorized to result from difficulties in transferring solidified products from the beaker to the crucible. Consequently, the actual MgO/13X ratios often differed from theoretical values, affecting adsorbent quality. Potential reasons include inaccurate measurement of precursor materials and incomplete impregnation of MgO into zeolite 13X, as suggested by XRD patterns. Ensuring proper sample collection and accurate measurement of precursors, as well as allowing sufficient time for water evaporation, could mitigate these issues.

4. Conclusions

In conclusion, the project successfully synthesized zeolite-supported alkali earth metal oxides for CO_2 capture, with four adsorbents exhibiting different MgO/13X ratios and percentage yields ranging from 67.49% to 89.96%. Characterization via XRF, XRD, and FTIR confirmed the presence of MgO and 13X in the adsorbents, signifying successful synthesis. Preliminary CO2 capture tests for Mg13X-1 and Mg13X-2 yielded promising results, although further testing for all four adsorbents was impeded by technical and budgetary constraints. Future work should encompass comprehensive carbon capture performance testing, cyclic stability assessments, and SEM microscopy to scrutinize the microstructure and ensure complete MgO impregnation into the 13X.

References

1. Herzog, H. (2023). *Carbon Capture*. MIT Climate Portal. https://climate.mit.edu/explainers/carbon-capture
2. United Nations. (2023). *What is the Paris Agreement?* United Nations. https://unfccc.int/process-and-meetings/the-paris-agreement
3. World Meteorological Organization. (2023). *2023 Shatters climate records, with major impact.* https://wmo.int/news/media-centre/2023-shatters-climate- records-major-impacts

CHAPTER 2

Composite Material

Unlocking The Potential of Mesoporous Iron Oxide Nanoparticles in Advanced Battery Applications

Fabrication of Multilayer Biopolymer Microcapsules by Using Alginate and Starch

Synthesis and Characterization of Membrane Material to Enhance Water Vapor Permeance

The Effect of Composite Thermo-Catalyst Based on Metals and Mxene for Ammonia Decomposition to Hydrogen

Preface

The pursuit of innovative materials and technologies is pivotal in addressing the pressing challenges of energy sustainability, environmental preservation, and biomedical advancements. This collection of abstracts reflects cutting-edge research endeavors across diverse scientific disciplines, each contributing to critical areas of modern science and technology. The first study underscores the systematic development of Fe_3O_4 nanorods, with a focus on their synthesis, characterization, and application potential in advanced battery technologies. Through a comprehensive analysis of their thermal, structural, and electrochemical properties, this research highlights their promise as high-performance electrode materials, emphasizing the role of precision and rigor in material science for sustainable energy solutions. The second abstract delves into the intersection of biotechnology and aquaculture, presenting the fabrication of multilayer microcapsules using biopolymers. Designed for targeted drug delivery, these microcapsules encapsulate bacteriophages and fish feed, offering a novel approach to disease prevention in fish populations. This study exemplifies the potential of biopolymer-based innovations in improving the efficacy and sustainability of aquaculture practices. The third study addresses the critical need for sustainable cooling technologies in the face of global warming and rising energy demands. By developing advanced composite membranes for Vacuum-Based Membrane Dehumidifiers, this research paves the way for more efficient and environmentally friendly cooling solutions. The meticulous optimization of membrane properties demonstrates the convergence of material science and engineering to tackle global energy challenges. Finally, the fourth study explores the utilization of MXene-based composite catalysts for ammonia decomposition, a process integral to hydrogen production. By examining the thermo-chemical dynamics of ammonia breakdown and optimizing catalyst performance, this research contributes to advancing clean energy technologies. It highlights the transformative potential of innovative catalysts in enabling a sustainable hydrogen economy. Together, these studies represent a collective effort to harness scientific ingenuity for addressing some of the most significant challenges of our time, from energy sustainability and environmental conservation to advancements in healthcare and aquaculture. Each study serves as a testament to the power of interdisciplinary research in driving progress and fostering innovation for a better future.

UNLOCKING THE POTENTIAL OF MESOPOROUS IRON OXIDE NANOPARTICLES IN ADVANCED BATTERY APPLICATIONS

Abstract: This study presents a systematic synthesis and characterization of Fe_3O_4 nanorods for potential application in advanced battery technologies. Fe_3O_4 nanorods were synthesized via a controlled precipitation method followed by annealing. Thermal properties, crystallographic structure, surface morphology, and electrochemical behavior were thoroughly investigated using various analytical techniques. Thermogravimetric Analysis (TGA) revealed the thermal stability and decomposition kinetics of the nanorods. X-ray Diffraction (XRD) confirmed the crystalline nature of the material, while Field Emission Scanning Electron Microscopy (FESEM) provided insights into its surface morphology. Brunauer-Emmett-Teller (BET) analysis determined the specific surface area and porosity, crucial for electrode materials. Cyclic Voltammetry (CV) studies elucidated the redox properties, essential for energy storage applications. The results demonstrate the potential of Fe_3O_4 nanorods as promising candidates for high-performance battery systems, highlighting the importance of systematic synthesis and comprehensive characterization in material design for sustainable energy solutions.

1. Research Background

This research focuses on the comprehensive exploration of mesoporous iron oxide nanoparticles for advanced battery technologies. Key areas of investigation include optimizing the synthesis of these nanoparticles by examining precursor concentrations, reaction temperatures, and times to achieve reproducible and well-defined results.

Advanced analytical techniques, such as TGA, XRD, FESEM, BET surface area analysis, and cyclic voltammetry, will be used to thoroughly characterize the nanoparticles' morphology, crystalline structure, and surface properties. The ultimate goal is to enhance energy storage technologies by improving the performance and sustainability of batteries using mesoporous iron oxide nanoparticles, addressing current limitations in the field.

2. Methodology

The methodology involves a systematic approach to synthesize and characterize Fe_3O_4 nanorods for potential applications in advanced battery technologies. Initially, $FeCl_3.6H_20$ and $FeSO_4.7H_2O$ are dissolved in distilled water, followed by the gradual addition of ammonia solution under controlled conditions. This leads to the formation of Fe_3O_4 nanorods, which are then subjected to heating, washing, and annealing steps to optimize their properties.

Following synthesis, the nanorods undergo comprehensive characterization using advanced analytical techniques. Thermogravimetric Analysis (TGA) assesses thermal properties and decomposition kinetics, while X-ray Diffraction (XRD) provides insights into crystallographic structure. Additionally, Field Emission Scanning Electron Microscopy (FESEM) offers high-resolution imaging, Brunauer-Emmett-Teller (BET) analysis determines specific surface area and porosity, and Cyclic Voltammetry (CV) studies redox properties.

By combining synthesis optimization with thorough characterization, this methodology aims to provide valuable

insights into the properties of Fe_3O_4 nanorods, contributing to their potential utilization in enhancing the performance and sustainability of advanced battery systems.

3. Results and Discussions

The FESEM analysis provided insights into how the morphology and pore structure of the nanoparticles changed with increasing annealing temperature. At 450°C, the nanoparticles displayed ordered, step-like structures, indicating a level of crystallinity. As the temperature rose to 550°C, a more intricate flower-like pattern emerged, suggesting a transition towards magnetite. By 650°C, the structures became blocky and crystalline, indicating further evolution towards magnetite formation.

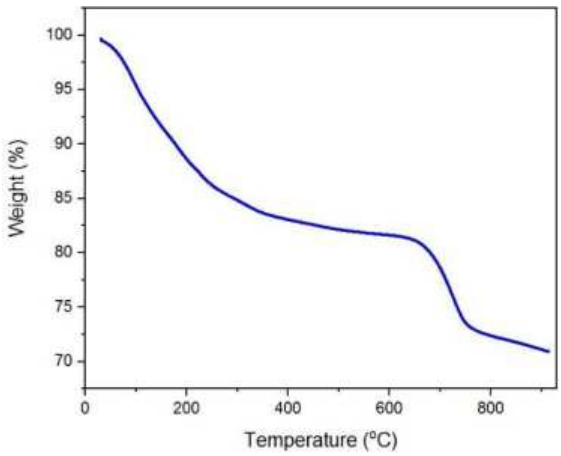

Figure 1: TGA Curve of the Samples

Thermogravimetric Analysis (TGA) shed light on the thermal behaviour of the samples. Initial weight loss observed at lower temperatures was attributed to the removal of physically absorbed water and volatile contaminants. As the temperature increased, gradual decomposition occurred, likely due to the thermal decomposition of Fe_2O_3 or its transformation into other iron oxides. At 800°C, the weight loss reduced, indicating substantial thermal decomposition had occurred.

X-Ray Diffraction (XRD) analysis tracked the phase transformation process from α-Fe_2O_3 to Fe_3O_4. Initially, at 350°C, the sample was predominantly α-Fe_2O_3, but as the temperature increased, the presence of Fe_3O_4 became more pronounced. By 650°C, Fe_3O_4 dominated, signifying a significant phase transition.

BET analysis delved into the surface properties and pore structure of the samples. At 550°C, the sample exhibited notable mesoporosity, which is essential for catalytic applications. Pore volume measurements indicated consistent data, with minimal contribution from micropores. The pore size distribution remained stable across adsorption and desorption phases.

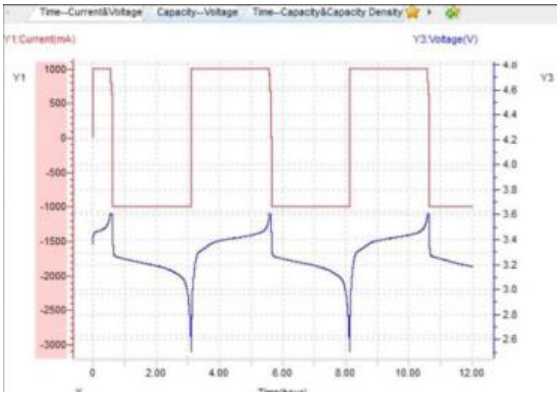

Figure 2: Cyclic Voltammetry Results

Cyclic Voltammetry profiles illustrated typical battery cycles, showcasing high- current discharge phases followed by low- current charge phases over a 12-hour period. The corresponding voltage profiles showed peaks around 4.8 V during charging phases, indicating the electrochemical behaviour of the samples.

4. Conclusions

The synthesized Fe_3O_4 nanorods show promising potential for advanced battery applications. Through systematic synthesis and comprehensive characterization, including TGA, XRD, FESEM, BET analysis, and CV studies, their structural and electrochemical properties have been elucidated. The nanorods demonstrate favourable thermal stability, crystalline structure, high surface area, and redox activity, all essential for efficient energy storage. This research contributes valuable

insights into the design and optimization of Fe_3O_4-based materials for sustainable and high-performance battery technologies, offering a pathway towards the development of next-generation energy storage systems.

References

1. Neware. (2017, January 15). Neware Tester BatteryTesting Equipment/Cycler - Neware Battery Cycler Curve View. Newarelab.com; Neware Tester - Battery Testing Equipment/Cycler.https://www.newarelab.com/support/neware-manual/item/95- newarebattery-cycler-curve-view
2. Lithium Ion Battery Coin Cell Lab Research Machine Manufacturers. (2016).Xmacey.com. https://www.xmacey.com/lithium-ion-battery -coincell-lab-research-machine_p264.html
3. Reversible Conversion Reactions of Mesoporous Iron Oxide with High Initial Coulombic Efficiency for Lithium-Ion Batteries. (2021). ACS Sustainable Chemistry & Engineering. https://pubs.acs.org/doi/abs/10.1021/acssuschemeng.1c05335
4. Iron-Air Batteries Promise Higher Energy Density Than Lithium-Ion Batteries. (2017, November 16). SciTechDaily. https://scitechdaily.com/iron-air-batteries-promise- higherenergy-density-than-lithium-ion-batteries/

FABRICATION OF MULTILAYER BIOPOLYMER MICROCAPSULES BY USING ALGINATE AND STARCH

Abstract: This study focuses on the fabrication of multilayer microcapsules using biopolymers alginate and starch. These capsules are designed for drug delivery and biomedical applications, particularly for disease prevention in fish populations. The microcapsules contain bacteriophages, which are viruses that target and kill bacteria, offering an alternative to antibiotics. The outer layer of the capsules also contains fish feed to attract fish, ensuring they consume both the feed and the phage. The multilayer structure enhances the capsules' strength, durability, and controlled-release properties, protecting the phages from extreme environmental conditions. However, this research does not explore the effects of temperature, pH, or water absorption on the microcapsules' stability. The study focuses solely on the fabrication method, using Sodium Alginate and Starch, and the resulting microcapsules are examined under a microscope.

1. Research Background

Aquaculture is a rapidly growing food sector, but it suffers from bacterial infections that cause significant economic losses due to decreased fish productivity, especially in high-density facilities. Vaccination has been effective in promoting fish immunity, but the previous reliance on antibiotics has led to antibiotic resistance. Encapsulation of bacteriophages (viruses that target bacteria) in multilayer microcapsules using alginate and starch offers better protection from extreme environmental conditions compared to single-layer capsules. This research aims to create multilayer microcapsules with phage at the core and fish feed in an outer layer, ensuring fish consume the beneficial phage. This method provides dual benefits of feeding fish and preventing infections, improving economic outcomes for fish farmers and enhancing the country's food industry.

2. Methodology

For fabrication of alginate microcapsules, there are preparation of soulutions like 50mM Tris- HCl (pH 7.5) and 5% of Calcium Chloride. Then, the solution is mixed with emulsifier and Sodium Alginate until the solution appear creamy. The mixture is then, being centrifuged at 400 rpm and later will go through washing steps for three times

Figure 1 shows the fabrication of microcapsules from Alginate that used as guide and reference, obtained from a research paper.

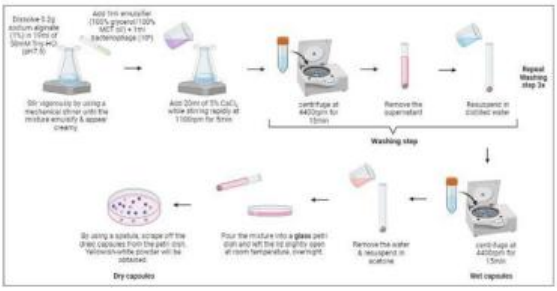

Fig. 1. Fabrication of Microcapsules from Alginate

For fabrication multilayer microcapsules from alginate, the steps are almost similar but only the amount of 0.3 ml of phage is being replaced with the mixture that contained single layer of alginate microcapsules

For fabrication of starch microcapsules, 30g of starch is dissolved in 200ml of 3.5M sulfuric acid. Then, the flask is covered with plastic wrap and leaved in oven overnight (16-18 hours) at 40 degree Celcius. The mixture is being centrifuged at 400 rpm for 15 minutes and a few washing steps until clean pellets have been obtained.

T the methodology of your research in this section using Times New Roman 12 pt with paragraph having justified alignment. For each section, the heading should be numbered 1., 2., etc. (heading Times New Roman 12 point bold). Separate each paragraph with an empty line. There is no restriction to length, as long as all sections are within the 2-page limit.

3. Results and Discussions

Figure 2: Alginate microcapsule obtained after centrifugation process

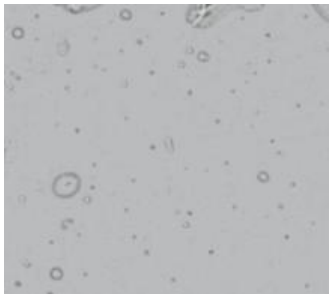

Figure 3: Alginate Microcapsuled Observed under Microscope

Figure 4: Starch microcapsule obtained after centrifugation

Figure 5: Starch Microcapsules Observed under Microscope

Figure 6: Alginate-alginate multilayer microcapsule observed under microscope

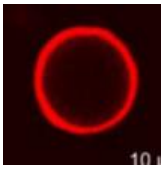

Figure 7: Multilayer Microcapsules of Alginate- Alginate Obtained from Research Article

The microcapsules shown in Figure 6 exhibit similar characteristics to those in Figures 7. They have round shapes with a ring around the circle, and their size falls within the accepted range of 1 to 10 micrometers. The morphology of the microcapsules appears consistent across both figures, suggesting the presence of multilayer capsules. However, further studies are required to conclusively confirm the existence of multilayer microcapsules.

4. Conclusions

In conclusion, this research achieved its objectives of fabricating multilayer microcapsules using alginate-alginate and studying their morphology. The LbL approachwas crucial for controlling size, shape, and composition, especially for incorporating functional moleculesphage. Fabricating multilayer starch microcapsules requires further troubleshooting, extendingthe research timeline. Matching biopolymer substances between alginate and starch and modifying fabrication methods for alginate microcapsules were explored. Overall, microcapsule technology shows promise for resilient crop protection in aquaculture, but ongoing research is vital for optimization and widespread adoption.

Reference

1. Blell R. Generating In-Plane Orientational Order in Multilayer Films Prepared bySpray- Assisted Layer-by-Layer Assembly.*ACS Nano.* 2017;11:84–94.
2. Khan M.A. Detection of Colonized Pathogenic Bacteria from Food Handlers in Saudi Arabia. *J. Pure Appl. Microbiol.*

SYNTHESIS AND CHARACTERIZATION OF MEMBRANE MATERIAL TO ENHANCE WATER VAPOR PERMEANCE

Abstract: This research addresses the need for sustainable and energy-efficient cooling technologies amid global warming and rising energy demands. The study enhances Vacuum-Based Membrane Dehumidifiers (VMDs) by developing composite membranes using polyvinyl alcohol (PVA) with potassium formate (KCOOH) and titanium dioxide (TiO2) on a stainless-steel wire mesh. By varying KCOOH concentrations and the number of dips in the dip-coating process, the research aimed to optimize the membrane's water vapor permeance, hydrophilicity, and cost-effectiveness. The findings demonstrated that increased KCOOH concentration and number of dips significantly improved the water vapor permeance. Sample M8, with 60% KCOOH content and 5 dips, was identified as the best performing membrane. These advancements contribute to more efficient and environmentally friendly cooling technologies, addressing the challenges of energy consumption and climate change.

1. Research Background

Global warming and rising energy demands have intensified the need for energy- efficient cooling technologies. Traditional air conditioning systems are energy- intensive and contribute significantly to global energy consumption (Shekh et al., 2023). Vacuum-Based Membrane Dehumidifiers (VMDs) offer a promising alternative, combining latent and sensible cooling processes to improve overall energy efficiency (Bui et al., 2021). The use of KCOOH in the PVA matrix improves the hydrophilicity and water vapor permeability, making the membranes more efficient and environmentally friendly (Shekh et al., 2023).

VMD systems operate by removing moisture from process air through a hydrophilic membrane layer, driven by a vapor pressure gradient created by a vacuum pump. This method offers a more sustainable solution compared to traditional air conditioning systems that rely on energy-intensive vapor compression cycles (Cho & Cheon, 2021). The development of efficient membranes for VMD applications is crucial for enhancing the performance of these systems and addressing the global challenge of rising energy consumption and climate change.

2. Methodology

The research employed a systematic approach to develop and characterize composite membranes by varying KCOOH concentrations (25%, 40%, and 60%) in the PVA solution and applying different numbers of dips (4 to 14) in the dip-coating process. Stainless-steel wire mesh served as the substrate. The dip-coating process included immersion, dwelling, withdrawal, and drying stages to ensure uniform coatings. Table 1 summarizes the experimental parameters for the membrane samples.

Table 1: Experimental Parameters for Membrane Samples

Membrane ID	KCOOH content in PVA/KCOOH Solution (%)	Number of Dips	Weight (g)	Dwelling Time (s)	Drying Temperature (°C)	Drying Time (min)
M1	25	10	5.0	30	80	10
M2	25	12	6.0	30	80	10
M3	25	14	7.0	30	80	10
M4	40	6	4.8	30	80	10
M5	40	8	6.4	30	80	10
M6	40	9	7.2	30	80	10
M7	60	4	4.8	30	80	10
M8	60	5	6.0	30	80	10
M9	60	6	7.2	30	80	10
M10	0	10	4.5	30	80	10

Comprehensive testing was conducted to evaluate the performance of the membranes. Water vapor permeance tests were performed according to the ASTM E96-21 Standard Test Methods for Water Vapor Transmission of Materials, while air permeance tests utilized a single gas permeation test setup. Morphological analysis was carried out using Field Emission Scanning Electron Microscopy (FESEM) to examine surface characteristics and coating uniformity, and Energy Dispersive Spectroscopy (EDS) was used to analyze the elemental composition of the membranes.

3. Results and Discussions

The study revealed that increasing KCOOH concentration and the number of dips significantly improved the water vapor permeance of the membranes. FESEM analysis showed that higher KCOOH content and more dips resulted in thicker, smoother, and more uniform coatings. EDS analysis confirmed the successful deposition of PVA/KCOOH coating, with variations in elemental composition reflecting the influence of KCOOH concentration and the number of dips. The water vapor permeance tests indicated that Sample M8, with 60% KCOOH content and 5 dips, exhibited the highest water vapor permeance, making it the most efficient membrane for practical applications.

Table 2: Water Vapor Permeance Data for Different Membrane Samples

Sample	dm/dt	KH20
M1	0.000033	1.16E-07
M2	0.000016	5.63E-08
M3	0.000033	1.16E-07
M4	0.000046	1.62E-07
M5	0.00003	1.06E-07
M6	0.000037	1.30E-07
M7	0.000159	5.60E-07
M8	0.000168	5.91E-07
M9	0.000141	4.96E-07
M10	0	0.00E+00

The water vapor permeance tests indicated that Sample M8, with 60% KCOOH content and 5 dips, exhibited the highest water vapor permeance, making it the most efficient membrane for practical applications. This sample demonstrated the best balance between coating thickness and uniformity, resulting in optimal performance.

4. Conclusions

This research has successfully developed and characterized composite membranes with enhanced water vapor permeance for VMD applications. The optimal membrane, Sample M8, demonstrated superior performance, highlighting the potential for more efficient and environmentally friendly cooling technologies. Future research should focus on incorporating contact angle measurements, producing larger membrane samples, exploring different PVA/KCOOH ratios, and conducting long-term performance testing in real-world applications to further enhance the membranes' efficiency and practicality.

References

1. Bui, T. D., Chen, F., Nida, A., Chua, K. J., & Ng, K. C. (2015). Experimental and modeling analysis of membrane-based air dehumidification. Separation and Purification Technology, 144, 114-122.
2. Shekh, A., Mohd, M. R., Muhamad, K. Ö., Md Shadab, A., & Shaikh, K. (2023). Technological development of evaporative cooling systems and its integration with air dehumidification processes: A review. Energy and Buildings, 283, 112805.
3. Lim, S., & Choi, H. (2020). Comparative analysis of various membrane-based vacuum air dehumidification systems. Applied Energy, 270, 116252.

THE EFFECT OF COMPOSITE THERMO-CATALYST BASED ON METALS AND MXENE FOR AMMONIA DECOMPOSITION TO HYDROGEN

Abstract: This study explores the potential of MXene-based composite catalysts to enhance ammonia decomposition for hydrogen production. Ammonia, a promising hydrogen carrier, could lead to a cleaner energy environment if efficiently broken down. The research investigates the thermo-chemical reaction of ammonia using MXene and metal composite catalysts. It examines the effect of temperature from 500 ℃ to 800 ℃ on ammonia decomposition at various inlet flow rates (0.5L/min, 0.3L/min, and 0.1L/min). The process involves setting up a hydrogen production system, testing flow rates and heat, and preparing a thermo-catalyst by coating nickel foam with CoS_2 MXene. Results are recorded, and ammonia conversion percentages are calculated and plotted against temperature to compare different flow rates. The performance of the experimented thermo-catalyst is also compared with other catalysts at a fixed temperature of 600℃ using data from research papers. The findings aim to provide a more effective and sustainable method for hydrogen production.

1. Research Background

Worldwide attempts to find greener energy options are fuelled by the substantial carbon emissions caused using fossil fuels. Hydrogen's potential is drawing attention as it is considered sustainable and environmentally benign. Ammonia is a particularly attractive hydrogen storage solution due to its affordability and readily available infrastructure. Thermo-catalyst efficiency is the main emphasis of this study's evaluation of ammonia breakdown techniques for hydrogen generation [1]. Nevertheless, there are still unanswered questions about the scalability and durability of composite thermo-catalysts. The research attempts to develop effective and sustainable hydrogen generating techniques by filling up these gaps [2].

2. Methodology

For thermo-catalyst production, the process involves preparing the nickel foam mesh and the MXene binder solution. First, the mesh's initial mass is recorded, cleaned with a mixture of ethanol, acetone, and distilled water, sonicated at 23℃ for 30 minutes, washed with deionized water, and immersed in acetic acid for 30 minutes to remove residual solvents. The mesh is weighed before and after these steps. For the binder solution, 0.2g of water-borne polyurethane is dissolved in 12.8g of ethanol, sonicated for 2 hours, and mixed with 0.72g of MXene powder for 20 minutes. The mesh is then coated with this solution using the dip-coating method.

The methodology involved placing the thermo-catalyst in the center of a stainless-steel pipe, with insulating materials at the inlet and outlet to minimize heat loss. Heated anhydrous NH_3 gas is fed into the pipe at reaction temperatures from 500℃ to 800℃. Three low flow rates (0.5 L/min, 0.3 L/min, and 0.1 L/min) were used to ensure safety, as ammonia gas is hazardous. Ammonia conversion was measured during steady-state reactions, with the catalyst undergoing self-activation under NH3 flow. The ammonia conversion percentage is calculated by using this equation:

$$NH_3 Conversion\ (\%) = 100 \times \frac{Q_{out}}{\frac{3}{2} Q_{in}}$$

3. Results and Discussions

This is the result of thermo-catalyst preparation:

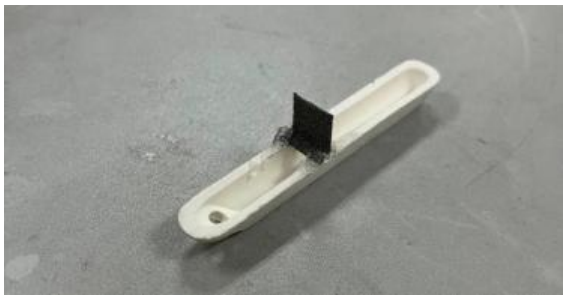

Fig. 1: Finishing of thermo-catalyst above ceramic kit

After setting up the temperature from furnace, the ammonia gas flows through the pipeline and the outlet flow rate are recorded. Then, the ammonia conversion percentage is calculated.

Table 1: Data of ammonia conversion percentage depending on temperature and flow rates

Thermocouple Temperature Value (°C)	Ammonia Conversion Percentage (%)		
	0.5 L/min	0.3 L/min	0.1 L/min
500	0.00	0.00	0.00
600	53.33	44.44	33.33
625	53.33	44.44	33.33
660	53.33	44.44	33.33
700	53.33	44.44	33.33
725	93.33	66.67	66.67
758	106.67	88.89	66.67
780	106.67	88.89	66.67

Fig. 2 demonstrates that higher temperatures enhance ammonia conversion, as the thermo-chemical reaction requires elevated heat levels for ammonia to decompose into hydrogen and nitrogen. Notably, at an inlet flow rate of 0.5 L/min, there's significantly higher ammonia conversion compared to lower rates. Ammonia conversion starts only after reaching 500°C, as indicated by a zero-conversion percentage before this temperature, marking the beginning of the decomposition process.

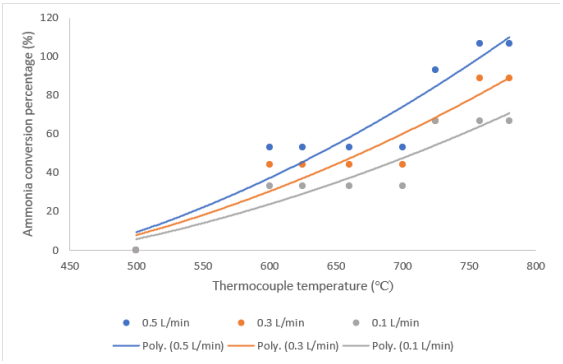

Fig. 2: Graph of ammonia conversion percentage against thermocouple temperature (℃)

Based on Table 2, it is shown that the experimental catalyst can be one of the potentials to decompose ammonia to hydrogen other than common catalyst that be tested from various research paper. Even though not higher than Ru/Cr_2O_3 and Co- SiO_2 because Ru/Cr_2O_3 is noble metal-based catalyst, so it is very efficient to decompose ammonia with lower activation energy same goes to Co-SiO_2.

Table 2: Comparison the ammonia conversion percentage between experimented thermo-catalyst with other types of thermo-catalyst

Catalyst	Ammonia Conversion	Ref.
Ni coated CoS_2 MXene at 0.5 L/min Test 1	53.3	–
Ru/Cr_2O_3	99.9	[3]
Fe/CNF	38.8	[4]
Co-SiO_2	94.9	[5]
FeMo/YSZ	50.0	[6]
$CoFe_5$/CNTs	45.0	[7]
Fused Fe-Co	40.0	[8]

4. Conclusions

This thesis examines the development and effectiveness of a composite thermo-catalyst, combining metals and MXene, for converting ammonia to hydrogen. Modified coating techniques ensured successful MXene deposition on nickel foam. The catalyst's performance was evaluated between 500°C and 800°C, showing higher efficiency at temperatures above 700°C. MXene's unique properties, such as high surface area, chemical stability, and thermal conductivity, contributed to its exceptional ammonia conversion perentage. The process demonstrated high hydrogen

production and stable operation across multiple cycles, suggesting promising prospects for MXene-based composite catalysts in sustainable hydrogen production at an industrial scale, calling for further optimization.

References

1. Sun, S., Jiang, Q., Zhao, D., Cao, T., Sha, H., Zhang, C., Song, H., & Da, Z. (2022). Ammonia as hydrogen carrier: Advances in ammonia decomposition catalysts for promising hydrogen production. *Renewable and Sustainable Energy Reviews*, *169*,112918. https://doi.org/10.1016/j.rser.2022.1 12918
2. Lee, J. E., Lee, J., Jeong, H., Park, Y.-K., & Kim, B.-S. (2023). Catalytic ammonia decomposition to produce hydrogen: A mini review. *Chemical Engineering Journal*, *475*, 146108. https://doi.org/10.1016/j.cej.2023.14 6108
3. Li, L., Wang, Y., Xu, Z. P., & Zhu, Z.(2013). Catalytic ammonia decomposition for co-free hydrogen generation over RU/cr2o3 catalysts. *Applied Catalysis A: General*, *467*, 246–252. https://doi.org/10.1016/j.apcata.2013 .07.003
4. Ji, J., Yan, X., Qian, G., Peng, C., Duan, X., & Zhou, X. (2017). Morphology and location manipulation of Fe nanoparticles on carbon nanofibers as catalysts for ammonia decomposition to generate hydrogen. *International Journal of Hydrogen Energy*, *42*(27), 17466–17475. https://doi.org/10.1016/j.ijhydene.20 17.04.037
5. Hu, X., Wang, W., Gu, Y., Jin, Z., Song, Q., & Jia, C. (2016). Co-SIO2 nanocomposite catalysts for COx- free hydrogen production by ammonia decomposition. *ChemPlusChem*, *82*(3), 368–375. https://doi.org/10.1002/cplu.2016004 44
6. Huang, C., Li, H., Yang, J., Wang, C., Hu, F., Wang, X., Lu, Z.-H., Feng, G., & Zhang, R. (2019). Ce0.6Zr0.3y0.1O2 Solid Solutions-supported Ni Co bimetal nanocatalysts for NH3 decomposition. *Applied Surface Science*, *478*, 708–716. https://doi.org/10.1016/j.apsusc.2019.01.269
7. Zhang, J., Müller, J.-O., Zheng, W., Wang, D., Su, D., & Schlögl, R. (2008). Individual fe−co alloy nanoparticles on carbon nanotubes: Structural and catalytic properties. *Nano Letters*, *8*(9), 2738–2743. https://doi.org/10.1021/nl8011984
8. Lendzion-Bieluń, Z., & Arabczyk, W. (2013). Fused feco catalysts for hydrogen production by means of the ammonia decomposition reaction. *Catalysis Today*, *212*, 215–219. https://doi.org/10.1016/j.cattod.2012. 12.014

CHAPTER 3

Material Testing and Characterization

Correlation Study Between Tensile Properties and Coil-Break Intensities of Uncoiled Low Carbon Steel Sheets

Study The Root Cause of Inconsistency on The Mechanical Properties in The Aging Process of 6061 Series Aluminum

Characterizing Tensile State Mechanical Properties and Their Impact on Thermomechanical Behavior of Solder Alloys in Power Electronics Modules

Relationship Between Extrusion Parameters and Mechanical Properties of Aluminium Alloy

Characterizing Shear State Mechanical Properties of Solder Alloys Through Digital Image Correlation Technique

Preface

Materials science and engineering play a vital role in addressing some of the most complex challenges in modern industry, from improving the reliability of electronic components to optimizing the structural integrity of metals and alloys. This collection of studies reflects diverse approaches to understanding and enhancing material behavior, offering practical solutions and insights across various fields. The first study takes on the challenge of coil breaks in low carbon steel sheets—a persistent issue impacting surface quality and production efficiency. By investigating how wall thickness and arc radius influence these defects, the research provides a deeper understanding of their root causes and presents strategies for mitigation, aiming to elevate production standards in the steel industry. In the second study, the spotlight turns to 6061 aluminum alloy, a cornerstone of modern engineering due to its strength and versatility. The research investigates heat treatment processes and their effects on tensile strength and hardness, uncovering the causes of production inconsistencies and offering pathways to refine alloy performance in large-scale applications. The third study addresses the critical demands of power electronics by examining SAC305 solder alloys and their behavior under thermal and mechanical stress. Through advanced modeling techniques and experimental validation, the research reveals how these materials perform in real-world conditions, guiding the design of more robust and reliable electronic systems. The fourth study explores the extrusion process and its impact on the mechanical properties of aluminum alloys. By integrating microstructural analysis with mechanical testing, the research sheds light on how parameters like temperature, speed, and post-treatment influence material performance, providing actionable insights for optimizing manufacturing processes. Finally, the fifth study investigates the shear properties of tin-bismuth solder alloys, a vital component in electronic assemblies. Using state-of-the-art Digital Image Correlation techniques, the research delivers precise measurements of mechanical behavior, enhancing the reliability of solder joints in a range of devices. Each of these studies exemplifies the intersection of innovation, experimentation, and application. Together, they highlight the transformative power of materials research in shaping technologies that are not only more efficient and durable but also capable of meeting the evolving demands of industry and society.

CORRELATION STUDY BETWEEN TENSILE PROPERTIES AND COIL-BREAK INTENSITIES OF UNCOILED LOW CARBON STEEL SHEETS

Abstract: This study investigates the persistent surface defects known as coil breaks in fully annealed low carbon steel sheets. These defects arise due to localized plastic deformation during the uncoiling process, often linked to tensile properties like yield spike height and yield point elongation. However, the impact of wall thickness and the arc radius of coil sheets on the formation of coil breaks remains underexplored. By analyzing tensile specimens from coils with varying wall thickness and using a 3D Optical Surface Texture Analyzer to observe coil break patterns, this research aims to elucidate the correlation between these factors and coil break intensity. The findings will contribute to better predictive models and mitigation strategies, ultimately enhancing the quality and profitability of low carbon steel sheet production.

1. Research Background

Coil breaks, or cross marks, are surface defects on fully annealed low carbon steel sheets caused by localized plastic deformation during uncoiling. These defects lead to significant material wastage and financial losses in the steel industry as affected sheets are often scrapped. Prior research has highlighted the role of tensile properties, such as yield spike height and yield point elongation, in coil break formation [1]. However, the effects of wall thickness and arc radius during uncoiling remain underexplored [2].

The arc radius decreases as the coil unravels, making high-curvature coils harder to flatten and more prone to break. Similarly, wall thickness variations can affect stress distribution and deformation during uncoiling, contributing to coil break severity [2].

This study aims to investigate the impact of wall thickness and arc radius on coil break formation, enhancing predictive capabilities and developing effective mitigation strategies to improve the quality and profitability of low carbon steel sheet production.

2. Methodology

This research adopts an empirical approach to investigate the formation of coil breaks in fully annealed low carbon steel sheets. Tensile tests were conducted on specimens cut from the top and end portions of annealed coils with varying wall thicknesses, ensuring a diverse range of material properties representative of industrial processes. The equivalent crosshead separation rate can be calculated using Eqn. 1. The presence and intensity of coil breaks were meticulously examined along uncoiled sheets, with samples displaying coil break marks extracted for further analysis.

$$v_c = L_c \times \dot{e}_{L_c} \ldots (1)$$

Surface roughness and waviness of the coil break marks will be measured using a 3D Optical Surface Texture Analyzer as shown in Fig. 1. The collected data on tensile properties and surface measurements will be analyzed to establish correlations with the intensity of coil breaks. This approach aims to understand the factors influencing coil break formation and contribute to developing strategies to mitigate these defects in the steel industry.

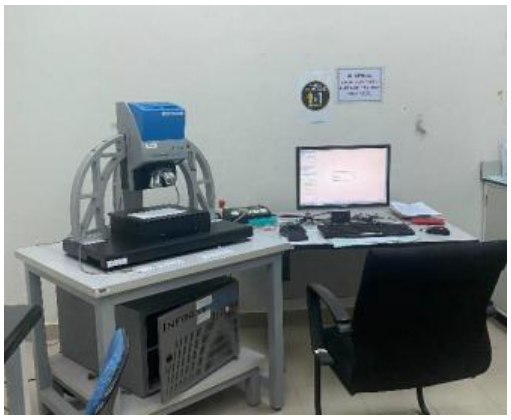

Fig. 1: 3D Optical Surface Texture Analyzer Setup

3. Results and Discussions

The observed trend in spike height based on Table 1 revealed a decrease as strip thickness increased, indicating a more gradual yielding behavior in thicker strips during tensile testing. This phenomenon is attributed to the distribution of stress across a larger cross-sectional area in thicker strips, resulting in reduced stress concentrations and less abrupt yielding [2].

Similarly, yield point elongation decreased with increasing strip thickness, with thicker strips exhibiting lower levels of elongation at the yield point compared to thinner ones. This suggests a reduced tendency for plastic deformation before failure in thicker strips, emphasizing their enhanced resistance to deformation owing to their larger cross- sectional areas [2].

Table 1: Averaged tensile properties

Thickness (mm)	LY (MPa)	UY (MPa)	SH (MPa)	YPE (MPa)
0.61	175.045	221.548	46.503	9.51
0.76	203.565	259.344	55.779	9.68
0.80	211.762	253.065	41.303	7.88
1.21	189.839	199.033	9.194	3.37
1.52	197.429	206.217	8.788	3.24

Table 2 data shows a relationship between coil break intensity and surface roughness and waviness parameters. For the 0.61 mm thick strips with severe coil break intensity, the Ra values range from 0.148 µm to 0.205 µm, while the Wa values range from 0.208 µm to 0.311 µm. In contrast, for the 0.76 mm thick strips with light coil break intensity, the Ra values range from 0.181 µm to 0.263 µm, and the Wa values range from 0.350 µm to 0.467 µm. This suggests that lighter coil breaks may lead to higher surface roughness compared to severe coil breaks [1].

Table 2: Surface roughness and waviness parameter

Thickness (mm)	Coil Break Intensity	Ra (µm)	Wa (µm)
0.61	Severe	0.185	0.208
0.61	Severe	0.148	0.266
0.61	Severe	0.180	0.311
0.61	Severe	0.158	0.287
0.61	Severe	0.205	0.281
0.76	Light	0.263	0.467
0.76	Light	0.240	0.350
0.76	Light	0.216	0.421
0.76	Light	0.181	0.431
0.76	Light	0.216	0.386

4. Conclusions

This research provides valuable insights into the relationship between strip thickness, coil break intensity, and surface roughness parameters in low carbon steel sheets. Thicker strips consistently displayed lighter coil break intensity compared to thinner ones, suggesting a significant role of strip thickness in mitigating coil breaks during manufacturing. Moreover, the study highlighted the influence of coil break intensity on surface roughness, with lighter coil breaks potentially resulting in higher surface roughness. Further research is recommended to explore these relationships in more depth and improve quality control strategies.

References

1. Mucsi, A. (2018). Analysis of coil break defects. *Engineering Failure Analysis*, *83*, 109–116. https://doi.org/10.1016/j.engfailanal.2017.09.022
2. Tan, C. J., & Liew, H. L. (2021). Investigation of coil-break formation during uncoiling of fully annealed low carbon steel sheet using FE simulation. *Engineering Failure Analysis*, *120*, 105112. https://doi.org/10.1016/j.engfailanal.2020.105112

STUDY THE ROOT CAUSE OF INCONSISTENCY ON THE MECHANICAL PROPERTIES IN THE AGING PROCESS OF 6061 SERIES ALUMINUM

Abstract: Aluminum alloys are renowned for their exceptional properties and widespread industrial applications, attributed to their abundance and enhanced strength when alloyed. Pure aluminum, despite its favorable characteristics, is often too soft for practical use. Alloying with various metals significantly improves its mechanical properties. This study focuses on the 6061 series aluminum alloy, particularly investigating the effects of heat-treatment—a process critical in enhancing tensile strength and hardness. However, heat-treatment also impacts other properties, such as reducing malleability and increasing brittleness. By analyzing data and observations from manufacturing facilities, this research aims to identify the root causes of inconsistencies in mechanical properties during large-scale production. The goal is to propose solutions to mitigate defects and improve the overall quality of aluminum alloys.

1. Research Background

Aluminium alloys are widely recognized for their versatility and applicability across numerous industries due to their superior material properties and abundance in the earth's crust. Pure aluminium, although possessing beneficial characteristics, is typically too soft for most industrial applications. This limitation is addressed by alloying aluminium with various metals or non-metals, significantly enhancing its strength and making it suitable for a range of uses.

Among the numerous aluminium alloy series, the 6061 series stands out for its balanced properties, making it a popular choice in applications requiring good mechanical properties and corrosion resistance. The primary focus of this study is on the 6061 series aluminium alloy, which is subjected to heat treatment to further enhance its mechanical properties. Heat treatment processes, such as ageing, are crucial in fine-tuning the alloy’s characteristics, particularly improving its tensile strength and hardness.

In large-scale manufacturing, inconsistencies in the mechanical properties of heat-treated aluminium alloys can arise, leading to defects and variability in product quality. This research aims to investigate the root causes of these inconsistencies in the ageing process of the 6061 series aluminium alloy. By conducting detailed process analysis and mechanical testing, the study seeks to identify the factors contributing to the variability in mechanical properties. This includes examining the operational practices, equipment, and conditions within the heat treatment facility.

The ultimate goal of this research is to propose solutions to minimize defects and enhance the consistency of the mechanical properties of the 6061 series aluminium alloy. Through a systematic analysis and comprehensive evaluation of the heat treatment process, this study endeavors to provide valuable insights and recommendations for improving the quality and reliability of aluminium alloys used in various industrial applications .

2. Methodology

1. Site Visit

During the on-site visit to the Heat Treatment Department at Press Metal Berhad Facilities, the primary objective will be to thoroughly understand the heat treatment process, specifically the aging of 6061 series aluminum. The visit will involve observing the entire process, from the preparation of aluminum billets to their placement in the aging ovens and noting the temperature regulation mechanisms and time intervals.

Figure 1 : The Position of alloys on the trolley inside the ageing oven

2. Data Analysis

This study will utilize Press Metal Berhad as its primary data source, focusing on the mechanical properties and failure rates associated with the 6061 series of aluminum. Data collection will involve acquiring comprehensive datasets encompassing tensile strength, yield strength, hardness, and failure rates linked to aging. The analysis will consist of correlation studies to identify relationships between mechanical qualities and failure rates, root cause identification to pinpoint factors contributing to variations in mechanical quality, and comparison with ASTM standards for 6061 aluminums. The results will be presented in a detailed report highlighting factors influencing mechanical characteristics during the aging process and offering recommendations for process optimization.

3. Mechanical Properties Tests

In the Mechanical Properties Test for the 6061 Alloy, two samples underwent a series of evaluations to assess their quality. Beginning with a Webster Hardness Test after cooling, both samples were then cut into smaller profiles for ease of milling. The milling process, conducted using a CNC milling machine with coolant to maintain alloy temperature, was followed by Spark Tests to analyze composition and ensure conformity. Subsequently, hardness tests were performed using Webster and Barcol equipment to gauge material hardness. The final stage involved Ultimate Tensile Strength (UTS) testing according to ASTM standards, utilizing the MTS Machine.

Figure 2 : Sample 1 performing the UTS

4. Metallography Analysis

The examination of its microstructure reveals crucial insights into its properties, particularly regarding the production and distribution of Mg2Si precipitates. These precipitates significantly enhance the alloy's hardness and strength. Cutting samples into smaller pieces facilitates the mounting process with phenolic resin, which aids in grinding and polishing for microscopic analysis. Grinding and polishing are conducted sequentially using specific grades of sandpaper and polishing compounds to achieve a mirror-like surface.

Subsequently, the samples are observed under an optical microscope to examine the formation and distribution of Mg2Si particles,

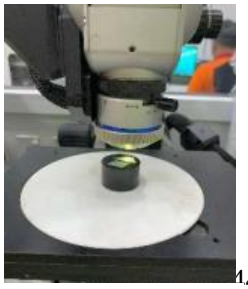

Figure 3 – Sample 1 under microscope

3. Results and Discussions

1. Ageing Oven Analysis & Maintenance

During site visits, ageing ovens were scrutinized for their vital role in aluminum alloy hardening. Proper stacking ensures uniform treatment, preventing damage and ensuring specified properties. Issues like defective timers and seal deterioration highlight the need for reliable equipment and maintenance. Regular checks and calibration maintain performance. Staggered calibration ensures ongoing precision. Thermocouple checks to identify air leakage for optimal efficiency.

2. Monthly QC Defect Data Analysis

Analyzing the monthly defect rate is crucial for maintaining quality and efficiency in aluminum alloy production at Press Metal Berhad. By monitoring failure rates, identifying patterns, and implementing corrective actions, the company can improve product quality, reduce waste, and meet quality standards. Focusing on May 2024, this study examines the monthly defect rate, particularly regarding hardness defects, to enhance production processes.

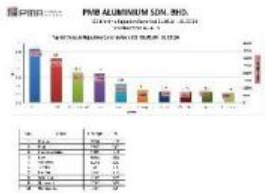

Figure 4 : Rejection percentage for different type of defects

3. Mechanical Properties Tests

The Hardness Test, as previously mentioned in the methodology section, is performed via a specialized instrument known as the webster Hardness Tester

The UTS Test, as described before in the methodology section, is conducted using a specialist instrument called the Instron® 3400 Series electromechanical universal testing equipment. [2]

Equipment	Tensile Stress (MPa)	Elongation (%)	Maximum Load (kN)
Universal Testing Machine	320.9	8.116	14.186

Figure 5 : Result for UTS of Sample 1

4. Metallographic Analysis

Sample 1 & Sample 2 was taken to the next step to further our analysis and discover other aspects of the alloy which are its microstructure[1]

Figure 7 : Sample 1 (Passed)

Figure 6 : Sample 2 (Failed)

4. Conclusions

This study investigates the inconsistencies in mechanical characteristics of 6061 aluminum during aging, aiming to enhance dependability and effectiveness in industrial applications, thus filling a significant gap in literature. Findings underscore the crucial role of microstructure, particularly Mg2Si particles, in influencing mechanical properties. Manipulating processing parameters like quenching and aging temperatures significantly impacts microstructure and material properties. Implementing precise heat treatments and automated control systems minimizes variability in final products. Manufacturers can enhance product quality and minimize defects by understanding underlying reasons for irregularities and making appropriate adjustments. Future research may explore sophisticated methodologies for regulating microstructure. Collaborations with academic and industrial partners can facilitate innovative solutions to manufacturing challenges.

References

1. Metallographic Specimen Preparation for 6061 Aluminium Alloy. (n.d.). Struers. Retrieved June 9, 2024.
2. How universal tensile testing machine works. (n.d.). Munro Scientific Division. Retrieved June 9, 2024

CHARACTERIZING TENSILE STATE MECHANICAL PROPERTIES AND THEIR IMPACT ON THERMOMECHANICAL BEHAVIOR OF SOLDER ALLOYS IN POWER ELECTRONICS MODULES

Abstract: This thesis investigates the tensile mechanical properties of SAC305 solder alloys and their influence on the thermomechanical behavior of power electronics modules using finite element analysis. Employing a model of a ball grid array (BGA) package with a 3x3 array of SAC305 solder balls connecting an STM32F103VET6 die to a FR4 printed circuit board (PCB), a constitutive elastoplastic-creep material model for SAC305 was developed in Ansys Workbench 2023, drawing on mechanical properties from literature. The model accurately predicted elastic properties with a 0.0258% discrepancy but overestimated plastic behavior by 9.0532% under monotonic tensile loading at a 0.01s^-1 strain rate, under thermal loads of 25°C and 125°C. Thermal cycling tests from -40°C to 125°C were conducted to evaluate the thermomechanical behavior of SAC305 solder in power electronic modules. Results showed increasing tensile stress during heating, decreasing stress at high-temperature dwell, and increasing strain. The highest stress and strain were observed at the contact region between the SAC305 solder joint, die, and PCB, attributed to a coefficient of thermal expansion (CTE) mismatch between die and PCB materials. However, the model underestimated average stress and strain compared to the Anand model. This study presents a simplified yet comparable model to characterize the thermomechanical behavior of SAC305 solder joints under realistic operational conditions, offering insights into temperature and loading effects.

1. Research Background

Solder alloys are crucial in power electronics for connecting components to printed circuit boards, providing structural support and ensuring reliable placement. Tin-lead (SnPb) solder has been widely used for over fifty years due to its excellent soldering properties, reliable performance and low cost. However, the lead's toxicity led to regulations like the EU's Restriction of Hazardous Substances (RoHS) Directive, banning SnPb solder in consumer devices since 2006. This prompted a global shift to lead-free alternatives, such as tin-copper (SAC) solder alloys like SAC105 and SAC305, now commonly used in the electronics industry [1].

SAC305 solder alloy is ideal for electronic assembly due to its suitable melting temperature, good wetting performance, strong mechanical properties and reliability with fatigue resistance and thermal cycling [2]. Evaluating the reliability of these solder joints, especially in power electronics, is essential but challenging with real-world tests due to time and complexity. Therefore, researchers often use computational modeling, such as the finite element method to assess SAC305's mechanical properties under tensile forces and temperature cycling.

Existing models like the Anand and Qian-Liu models are complex and time-consuming. This research aims to propose a simpler constitutive elastoplastic-creep material model for SAC305 using finite element analysis (FEA) in Ansys. The goal is to streamline simulations and make the analysis of SAC305 solder joints more efficient and accessible while maintaining accuracy in evaluating their reliability and thermomechanical behavior in power electronics modules.

2. Methodology

The model used is a ball grid array (BGA) package with a 3x3 array of SAC305 solder balls to connect a STM32F103VET6 die to a FR4 printed circuit board (PCB) as shown in Fig. 1. The dimensions of the components are shown in Table 1.

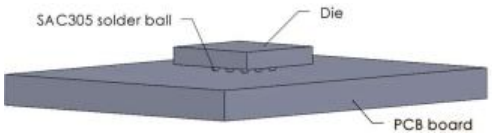

Fig. 1: BGA package model geometry

Table 1: Dimensions of the components

Parts	Ball diameter (mm)	Ball height (mm)	Size (length × wide × height) (mm)
Solder ball	0.5	0.35	-
Die	-	-	5 × 5 × 0.9
PCB	-	-	15 × 20 × 1.57

The mechanical properties of SAC305, the die and the PCB are based on literature values, including Young's Modulus, Poisson's ratio and the coefficient of thermal expansion. The behavior of SAC305 is modeled using the isotropic elasticity model for elasticity, the bilinear kinematic hardening model for plasticity, and the Generalized Garofalo model for creep. The isotropic elasticity parameters come from the stress-strain curve in [3] while the bilinear kinematic hardening model uses a yield strength of 68 MPa and a tangent modulus of 180 MPa as reported by [4]. The creep behavior is defined using constants from [5], detailed in Table 2.

Table 2: Generalized Garofalo constants

Constants	C_1 (s^{-1})	C_2	C_3 $(MPa)^{-1}$	C_4 (KJ/mol)
Values	1.04	0.46	0.045	3360

Boundary conditions are applied to simulate real conditions. Displacement is used to represent strain rate, and thermal loading cycles from -40°C to 125°C with 10-minute dwells and 15-minute ramps, following the JESD22-A104C standard for 3 cycles (18000s). The thermal cycling profile is shown in Fig. 2. Fixed support is applied to the die and PCB to restrict their displacement and rotation during the applied strain rate and thermal loading.

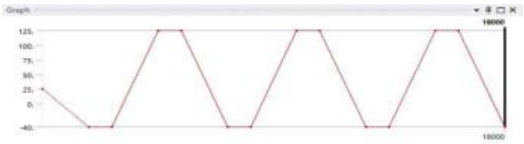

Fig. 2: Thermal cycling profile

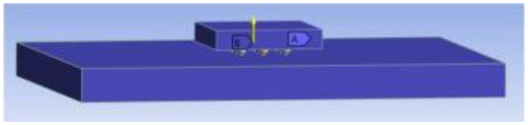

Fig. 3: Boundary conditions of the model

Lastly, the constitutive model is compared with the Anand model under the same analysis settings. The parameters for the Anand model are sourced from [3] and detailed in Table 3.

Table 3: Anand parameters

S_0 (MPa)	Q/R (1/K)	A (s^{-1})	ζ	m	h_0 (MPa)	s (MPa)	n	a
21	9320	3501	4.0	0.25	180000	30.2	0.01	1.78

3. Results and Discussions

In monotonic tensile loading, the equivalent stress and strain of the SAC305 model are evaluated under boundary conditions strain rates (0.001s-1) and temperatures (25°C and 125°C).

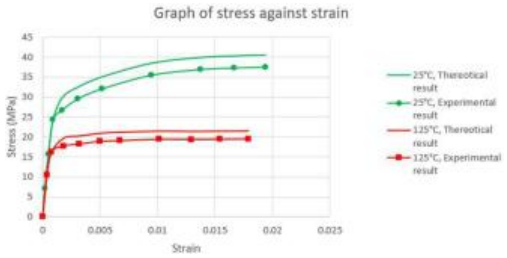

Fig. 4: Stress-strain curve under 0.001s^{-1}

The constitutive model closely estimates the elastic properties of the SAC305 solder ball with a 0.0258% discrepancy, but overestimates plastic behavior by 9.0532% under constant thermal loading at 25°C and 125°C. This slight inaccuracy may stem from the simplified bilinear kinematic hardening model utilized. Nonetheless, the overall results are acceptable and relatively accurate, with discrepancies remaining below 10%.In thermal cycling, the average equivalent stress and strain of the SAC305 solder ball from the constitutive model are evaluated and compared with the Anand model as shown in Fig 5 and Fig 6.

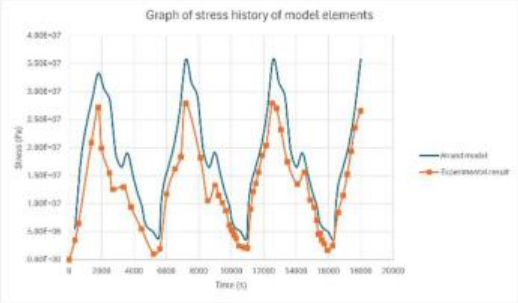

Fig. 5: Graph of stress history of the constitutive model and Anand model

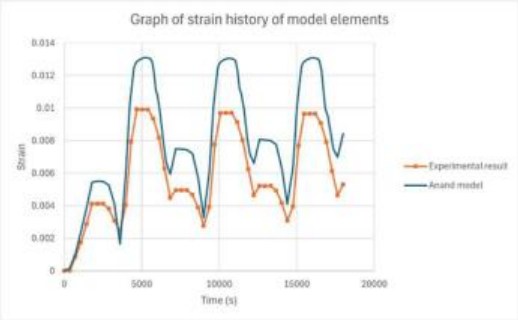

Fig. 6: Graph of strain history of the constitutive model and Anand model

Both Fig. 5 and Fig. 6 reveal similar patterns between the constitutive model and the Anand model. The constitutive model underestimates the average stress and strain of SAC305 solder balls across three thermal cycles. This discrepancy may arise from the constitutive model's reliance on three separate models (isotropic elasticity, bilinear kinematic hardening, and Generalized Garofalo), necessitating material property inputs and potentially accumulating errors. Additionally, there's an increase in tensile stress during thermal ramp-up and a subsequent stress release with increased strain during the high-temperature dwell phase. Stress concentrations are highest at the contact region between the SAC305 solder joint, die, and PCB due to CTE mismatch, potentially leading to failure.

4. Conclusions

This study introduced a simplified constitutive elastoplastic-creep model for SAC305, incorporating isotropic elasticity, bilinear kinematic hardening, and Generalized Garofalo in Ansys. While accurately estimating elastic properties with a 0.0258% discrepancy, the model overestimates plastic behavior by 9.0532% under monotonic tensile loading and underestimates average stress and strain during thermal cycles compared to the Anand model. Despite these discrepancies, the model provides conservative estimates, offering precise elastic and moderate plastic simulation of SAC305.

The constitutive model underwent thermal cycling from -40°C to 125°C to assess SAC305's thermomechanical behavior in quarter-scale power electronic modules. It showed increased tensile stress during thermal ramp-up, but stress was released at high temperatures while strain increased. The highest stress and strain were at the contact region between the SAC305 solder joint, die and PCB due to CTE mismatch, posing a risk of failure. This finding is valuable as it identifies critical points in the BGA structure under thermal cycling, predicting solder joints' stress-strain responses and informing electronic packaging structural design for targeted fatigue life.

References

1. Cheng, S., & Pecht, M. (2017). A review of lead-free solders for electronics applications. *75*, 77-95.
2. Anderson, I. E. (2007). Development of Sn-Ag-Cu alloys for Pb-free electronic solder applications. *Lead-Free Electronic Solders: Materials in Electronics* (pp. 55-76). Boston, MA: Springer US.
3. Motalab, M. & Lall, P. (June 2012). *Determination of Anand constants for SAC solders using stress-strain or creep data.* Paper presented at the 13th InterSociety Conference on Thermal Phenomena in Electronic Systems.
4. Fun, Seng Phan (2019) Modelling Of Mechanical Behaviour Of Electronics Materials. Universiti Sains Malaysia, Pusat Pengajian Kejuruteraan Mekanik. doi: http://eprints.usm.my/id/eprint/58428
5. Fahim, A., Hasan, K & Lall, P. (2021). Prediction of Stress-Strain Behavior of Thermally Cycled SAC305 Solder Joints by Finite Element Modeling and Nanoindentation Characterization. *20th IEEE Intersociety Conference on Thermal in Electronic Systems (iTherm)*, 917-926. doi:10.1109/ITherm51669.2021.9503218

RELATIONSHIP BETWEEN EXTRUSION PARAMETERS AND MECHANICAL PROPERTIES OF ALUMINIUM ALLOY

Abstract: This study addresses critical gaps in literature by exploring the intricate relationship between extrusion parameters and the mechanical properties of aluminum alloys. The research aims to provide a comprehensive analysis of how mechanical properties, such as yield strength, ultimate tensile strength, are influenced by extrusion conditions, including temperature, speed, and die parameters. Through the application of linear multiple regression (LMR) models, it was found that both an increased reduction ratio (36%) and temperature (20%) result in a slight decrease in ultimate strength (2%), while a higher temperature alone (20%) significantly reduces yield strength (9%). The study also delves into the effects of homogenization, extrusion, and post-extrusion annealing treatments on the microstructure and mechanical properties of 2024 aluminum alloy. Findings reveal notable grain refinement, with coarse eutectic microstructures at grain boundaries becoming uniformly distributed post-annealing. The presence of S (Al2CuMg) and Al7Cu2Fe second phases in the extruded material significantly enhances tensile strength and elongation by 176% and 547%, respectively. By addressing inconsistencies in previous methodologies through a systematic approach encompassing microstructural analysis, extensive mechanical testing, and controlled extrusion experiments, this research aims to establish a unified framework for optimizing extrusion processes and advancing the understanding of materials science.

1. Research Background

Aluminum alloys, particularly the 2024 alloy, are widely used in aerospace and automotive industries due to their excellent strength-to-weight ratio and mechanical properties. Despite their extensive application, optimizing the extrusion process to enhance these properties remains a challenge. The most important factors shaping these properties include the content of alloying elements (mainly the addition of copper), as well as parameters of plastic forming and heat treatment (Martin, 2012)

Additionally, The major alloying elements in 6000 series Al alloys are magnesium (Mg) and silicon (Si). The formation of magnesium silicide (Mg2Si) requires a Mg/Si ratio of 1.73 by mass (Mukhopadhyay, 2012). There is an abundance of these alloy grades commonly differentiated by their chemical composition, extrudability and material properties (Sheppard, 2013). Treatments like homogenization, extrusion, and post-extrusion annealing have been found to improve grain refinement and mechanical properties, yet their combined effects are not fully understood. This study aims to systematically investigate these interactions to develop a unified framework for optimizing the extrusion process of 2024 aluminum alloy. By addressing these gaps, the research seeks to advance the understanding and application of aluminum alloys in high-performance industries.

2. Methodology

This study explores how extrusion parameters affect the microstructure and mechanical properties of Aluminum 6082 and 2024 alloys. High-quality alloy specimens are prepared, cleaned, and organized. For Aluminum 6082, samples are extruded at temperatures of 350°C, 425°C, and 500°C with reduction ratios of

6, 8.5, and 11. Tensile specimens are produced per ASTM standards, measuring Young's Modulus, ultimate tensile strength, yield strength, and elongation.

Microstructural analysis uses electropolishing and micro-etching to reveal grain structures. For the 2024 alloy, ingots are extruded at 380°C with an extrusion ratio of 4.2 and speed of 1.0 mm/s, forming a profile with dimensions of ϕ202 × 53 mm. Post-extrusion, samples undergo tensile testing at room temperature, followed by SEM analysis of fractures.

Microstructural characteristics in as-cast, extruded, and extrusion + annealed states are examined using a laser confocal microscope. Samples are polished and corroded with Keller reagent for detailed analysis. This methodology ensures precise control of extrusion parameters and comprehensive understanding of their effects on aluminum alloys.

3. Results and Discussions

In the microstructure analysis phase, it was clearly observed that as both reduction ratio and extrusion temperature increase, the sample's grain size increases, while the grain boundaries and voids intensity decreases; giving a visually more similar structure to that of the parent material.

Implementing into the linear multiple regression (LMR) models, it is found that increasing both reduction ratio (36%) and temperature (20%) leads to a slight decrease in ultimate strength (2%), while higher temperature alone (20%) reduces yield strength more significantly (9%)., it was discovered that the optimum extrusion temperature and reduction ratio values to obtain the highest yield tensile strength (105.06 MPa) and ultimate tensile strength (166.07 MPa) are 350°C and 6, respectively.

The effects of homogenization, extrusion and post extrusion annealing treatment on the microstructure and mechanical properties of 2024 aluminum alloy were discussed in detail. The results indicate that the grain refinement of the extruded alloy material is significant.

The coarse eutectic microstructure at the grain boundaries was refined, and these grains tended to be uniformly distributed after the annealing treatment. Extruded 2024 aluminum alloy material mainly has S (Al2CuMg) and Al7Cu2Fe second phases. The appearance of a large number of S phases led to a significant improvement in the properties of the alloy with an increase in tensile strength and elongation of 176% and 547%, respectively.

4. Conclusions

This study investigated the impact of extrusion parameters on the microstructure and mechanical properties of Aluminum 6082 and 2024 alloys. By varying extrusion temperature and reduction ratio, higher temperatures and ratios result in finer, more uniform grain structures, enhancing tensile strength and ductility. For Aluminum 6082, the best tensile strength was at 350°C with a reduction ratio of 6. Post-extrusion annealing significantly improved the strengths of the 2024 alloy. The findings highlight the importance of precisely controlling extrusion parameters to optimize the mechanical properties and microstructure for high-performance applications.

References

1. Martin JW Precipitation Hardening: Theory and Applications,Butterworth-Heinemann, 2012
2. Mukhopadhyay, P. (2012). Alloy designation, processing, and use of AA6XXX series aluminium alloys. ISRN Metallurgy, 2012.
3. Sheppard, T. (2013). Extrusion of aluminium alloys. Springer Science & Business Media.

CHARACTERIZING SHEAR STATE MECHANICAL PROPERTIES OF SOLDER ALLOYS THROUGH DIGITAL IMAGE CORRELATION TECHNIQUE

Abstract: Soldering joins metals with a lower-melting alloy, crucial for assemblies, heat dissipation, and electrical signal transmission. Environmental concerns led to lead-free solders, with tin-bismuth (Sn-Bi) alloys popular for their low melting point of 138 °C and strong joint strength. Evaluating solder mechanical properties, especially under shear conditions, is essential since traditional tensile tests may not reflect real-world scenarios where solder joints experience shear forces. This research uses Digital Image Correlation (DIC) to precisely measure shear properties. The methodology involved fabricating C1100 copper plate specimens, soldering them with Sn-Bi alloy in a vacuum furnace, and applying a speckle pattern for DIC analysis during tensile shear tests at different strain rates. The study confirmed DIC reliability, with slight deviations from Universal Testing Machine (UTM) measurements and found higher strain rates resulted in fewer data points and a higher shear modulus. These findings enhance the understanding of solder shear properties, ensuring their reliability in electronic devices.

1. Research Background

Soldering is a crucial process in various industries. Historically, tin-lead (Sn63-Pb37) was the preferred alloy for its cost-effectiveness and excellent properties [4]. However, environmental concerns led to restrictions on lead in electronics, enforcing environmentally friendly alternatives [1].

Tin-bismuth (Sn-Bi) solders have become a popular lead-free alternative due to their low eutectic melting point of 138 °C and offering strong joint strength [2]. Despite their advantages, Sn-Bi solders can form low melting point intermetallic compounds, affecting reliability [3]. Hence, identifying their mechanical properties is vital for ensuring practical industrial application.

Conventional tensile tests may not accurately reflect real-world conditions where solder joints experience shear forces [5]. Single lap shear tests are more suitable for simulating these conditions, and Digital Image Correlation (DIC) is recommended for analyzing mechanical characteristics due to its effectiveness with small samples and rapid failure detection.

2. Methodology

A 3 mm thick C1100 copper plate was selected for the shear test as its widespread use in electronics. The specimen geometry was designed for single lap joint testing, addressing potential imbalances, and bending moments from tensile forces.

The specimens were fabricated via wire cut EDM, followed by cleaning with isopropyl alcohol and citric acid in an ultrasonic cleaner. Soldering was done in a vacuum furnace with Sn-Bi solder paste, and the joint area was patterned for DIC analysis.

Fig. 1: Well prepared specimen

Tensile shear tests were conducted using an Instron 3369 UTM at 3 grip displacement rates (0.6 μm/s, 3.0 μm/s, 6.0 μm/s). Specimens were clamped, and a camera captured images of the speckle pattern during testing. Data was collected and analyzed for shear stress and strain.

DIC analysis was performed using VIC-2D software to track material deformation.

Captured images were uploaded, and the region of interest was specified. The software calculated pixel displacements, allowing for accurate shear strain measurement. Calibration and data reduction were performed, and results were analysed to plot shear stress-strain graphs.

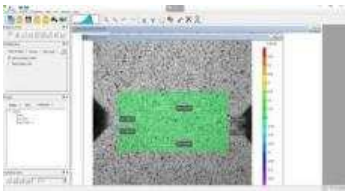

Fig. 2: Analyse speckle images with DIC

3. Results and Discussions

The shear stress-strain curves for specimens at a grip displacement rate of 0.6 µm/s show distinct elastic and plastic deformation regions, indicating the ductile nature of the tin-bismuth solder. Data from UTM and DIC techniques show similar trends, but DIC consistently measures higher strains, telling its higher sensitivity.

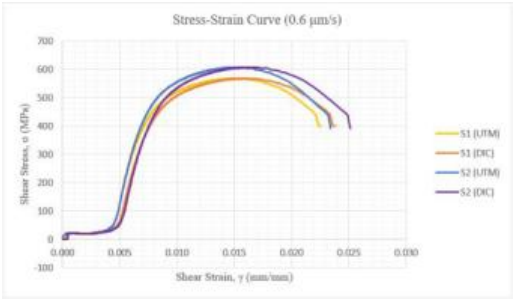

Fig. 3: Shear stress-strain curve plotted from data analysed at 0.6 µm/s grip displacement rate

At a higher displacement rate of 3.0 µm/s, stress-strain curves resemble those at 0.6 µm/s, with DIC again measuring higher strains. Variations between specimens suggest differences in solder joint quality due to soldering positioning.

Fig. 4: Shear stress-strain curve plotted from data analysed at 3.0 µm/s grip displacement rate

At the highest displacement rate of 6.0 µm/s, significant differences occur between specimens, especially Specimen 6, showing abnormal behavior suggestive of brittleness, likely influenced by a larger solder joint area. Specimen slippage was evident at the beginning of all tests due to low friction between grips and specimens.

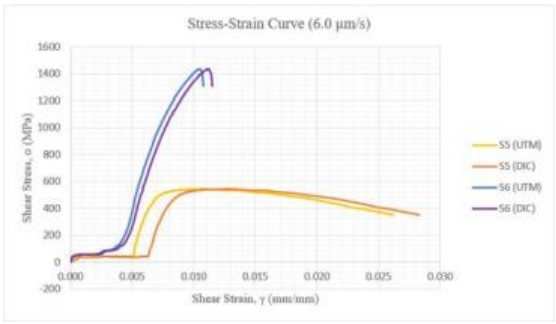

Fig. 5: Shear stress-strain curve plotted from data analysed at 6.0 µm/s grip displacement rate

DIC proved reliable for measuring shear strain, with an average percentage difference of around 14% compared to UTM data. Both methods showed similar trends, with DIC consistently measured higher shear strains than UTM. This discrepancy is likely due to variations in measurement techniques, specimen preparation, and inherent constraints.

Table 1: Average percentage of differences of shear strain measured from UTM and DIC techniques

Specimen	Average percentage difference of shear strain (%)
S1	9.7759478
S2	12.7761259
S3	14.2439367
S4	6.7909966
S5	33.9769644
S6	9.6784842
Average	14.5404093

As strain rates increase, solder joints yield faster, shortening the time to capture speckle pattern deformation. This reduces speckle images from 2253 to just 203 at a higher rate, resulting in fewer data points for shear stress-strain graphs and affecting accuracy. Higher strain rates also increase shear modulus, leading to a stiffer solder response as reduced atomic reorganization and dislocation movement time.

Table 2: Influence of strain rate on number of speckle images being analysed and the shear modulus

Strain rate	S	Speckle images	Shear modulus	
			UTM (GPa)	DIC (GPa)
0.6 μm/s	S1	2250	73.337	87.067
	S2	2253	80.794	98.650
3.0 μm/s	S3	407	106.379	117.065
	S4	349	107.914	121.883
6.0 μm/s	S5	222	90.424	227.293
	S6	203	218.174	233.234

4. Conclusions

Shear strain data were plotted against shear stress to analyze the mechanical properties of Sn-Bi solder alloy. DIC proved reliable with a shear strain measurement deviation of around 14% compared to UTM. Higher strain rates increased shear modulus and stiffness but reduced DIC accuracy due to fewer speckle images.

References

1. Cheng, S., Huang, C.-M., & Pecht, M. (2017). A review of lead-free solders for electronics applications. *Microelectronics Reliability*, *75*, 77–95. https://doi.org/10.1016/j.microrel.2017.06.016
2. Frear, D. R. (2006). Issues related to the implementation of Pb-free electronic solders in consumer electronics. *Journal of Materials Science: Materials in Electronics*, *18*(1-3), 319–330. https://doi.org/10.1007/s10854-006-9021-7
3. Kotadia, H. R., Howes, P. D., & Mannan, S. H. (2014). A review: On the development of low melting temperatu- re Pb-free solders. *Microelectronics Reliability*, *54*(6-7), 1253–1273. https://doi.org/10.1016/j.microrel.2014.02.02
4. Ma, H., & Suhling, J. C. (2009). A review of mechanical properties of lead-free solders for electronic packaging. *Journal of Materials Science*, *44*(5) 1141–1158. https://doi.org/10.1007/s10853-008-3125-9
5. Yee, S. C., Wong, K. M. C., & Isayeva, G. (2019). A Study on the Shear Strength and Failure Modes of Sn-3.0Ag-0.5 Cu Solder Joint Containing. *IOP Conference Series: Materials Science and Engineering*, *495*, 012085. https://doi.org/10.1088/1757-899x/495/1/012085

CHAPTER 4

Renewable Materials Engineering

Synthesis, Optimization and Characterization of Graphene Oxide Using Bio-Waste

Regeneration of Sodium Borohydride (NaBH4) by Ball Milling Sodium Metaborate (NaBO2) With Magnesium: A Sustainable Approach for Hydrogen Storage

Green Synthesis of Graphene Oxide

Design of an Affordable Motorized Wheelchair Using Sustainable Materials

Preface

The intersection of sustainability, innovation, and practicality underpins the research endeavors presented in this collection. These studies exemplify the creative application of science and engineering to address global challenges, focusing on eco-friendly materials, renewable energy solutions, and accessible technology for enhanced quality of life. The first study pioneers the synthesis of Graphene Oxide (GO) from pineapple peel bio-waste, proposing a sustainable alternative to traditional resource-intensive methods. By repurposing agricultural waste and minimizing environmental impact, this research not only contributes to the burgeoning graphene market but also underscores the potential of green chemistry in fostering environmental stewardship. In the second study, the regeneration of sodium borohydride ($NaBH_4$) is explored through the ball milling process of sodium metaborate with magnesium. This innovative approach enhances the reusability of $NaBH_4$ as a hydrogen storage material, addressing critical aspects of sustainable energy systems. The study's findings on reaction kinetics and structural transformations provide a pathway for optimizing hydrogen storage technologies for a greener future. The third study investigates greener alternatives to traditional acids for the synthesis of Graphene Oxide using a modified Hummers' Method. While experiments with acetic acid and wood vinegar yielded insights into oxidation limitations, they also reaffirmed the necessity of strong acids for successful GO synthesis. The findings contribute to the ongoing quest for sustainable yet effective methods in materials science. The fourth study tackles the accessibility and sustainability of mobility aids, presenting the development of an affordable motorized wheelchair using rattan as a primary material. By bridging the gap between cost and functionality, this project aligns with multiple Sustainable Development Goals, showcasing how innovation in design and material selection can transform lives while promoting environmental consciousness. Together, these studies demonstrate the profound impact of integrating sustainability into scientific exploration and technological advancement. By addressing pressing challenges with innovative and practical solutions, they highlight the transformative potential of research in building a more equitable and sustainable world.

SYNTHESIS, OPTIMIZATION AND CHARACTERIZATION OF GRAPHENE OXIDE USING BIO-WASTE

Abstract: This research focuses on the synthesis, optimization, and characterization of Graphene Oxide (GO) using pineapple peel bio-waste. Traditional methods of GO synthesis often involve harsh chemicals and resource-intensive processes, leading to environmental degradation. In contrast, this study explores a sustainable approach by utilizing agricultural waste. The pineapple peel waste was pyrolyzed at 500°C, and 600°C under inert gas, and the pyrolyzed samples at 500°C and 600°C were used to synthesize GO. The characterization of the samples included XRD and FTIR spectroscopy, confirming the presence of oxygen-containing groups and validating the successful synthesis of GO. This novel approach demonstrates the potential for eco-friendly production of GO, contributing to both environmental sustainability and the expanding graphene market.

1. Research Background

Graphene Oxide (GO) is a layered carbon structure with oxygen-containing functional groups (e.g., =O, -OH, -O-, -COOH) on its surfaces and edges (Shin et al., 2017). Depending on the number of layers, GO can range from single-layer to multilayered structures, with specific nomenclature distinguishing between few-layered and graphite oxide when exceeding ten layers (1). GO is produced by oxidizing graphite into graphite oxide and then exfoliating it. The synthesis method significantly influences the characteristics of GO, particularly the type and quantity of oxygen functionalities.

However, traditional GO synthesis methods involve harsh chemicals and energy- intensive processes, raising environmental and sustainability concerns. This project addresses these challenges by exploring the use of bio-waste as a precursor for GO synthesis. The aim is to develop a more sustainable and environmentally friendly method for producing GO, leveraging agricultural waste materials like pineapple peel.

2. Methodology

The proposed methodology for this project involves a systematic approach to explore and compare conventional methods with a sustainable alternative. The initial phase focuses on a thorough literature review to comprehend existing synthesis techniques, specifically the conventional Hummer (HM)(2) and Improved Hummer methods (IHM) (3) identifying their respective strengths and limitations. Following this, the controlled sample GO are synthesized using the conventional method to establish a baseline for comparison. The characterization of the controlled sample involves thermogravimetric analysis (TGA), X-ray diffraction (XRD), and Fourier transform infrared spectroscopy (FTIR) to analyze its thermal stability, crystal structure, and functional groups.

Concurrently, pineapple waste is chosen for conversion into biochar through pyrolysis, and the synthesis of GO is to be attempted using this pineapple-waste-derived precursor. This is called method 3. Characterization of the bio-waste-derived GO includes XRD and FTIR analyses for

comparison with the controlled sample. The project concludes by summarizing findings, drawing comparisons, and discussing the feasibility and sustainability of the bio- waste-derived synthesis, while also suggesting potential areas for future research and applications.

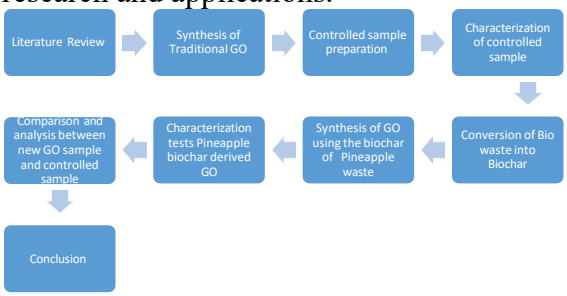

Fig. 1: Flowchart of the methodology process.

3. Results and Discussions

The TGA and XRD analyses of GO samples synthesized using the Hummer's Method (HM) and Improved Hummer's Method (IHM) show key differences. The HM sample had a 70% mass loss in the 0-200°C range, indicating removal of water and volatile components, and showed substantial thermal resistance above 400°C. The IHM sample exhibited a lower mass loss of 60%, suggesting better thermal stability. XRD results for HM showed peaks at 23.03°, 26.23°, 42.81°, 46.68°, and
79.12°, indicating partially reduced GO and structural defects. The IHM sample had peaks at 16.12°, 22.77°, 60.76°, and 81.24°,
indicating the presence of GO with expanded interlayer spacing and structural defects

The XRD analysis of the 500°C sample reveals peaks at 18.26°, 25.51°, 26.75°, and 28.49°, indicating the presence of oxygen- containing groups, graphite, and possibly suggesting incomplete oxidation or a mixture of graphite and GO. The FTIR spectrum shows broad peaks around 3600- 3200 cm^{-1} (hydroxyl groups), 3000-2850 cm^{-1} (C-H stretching), 1750-1650 cm^{-1} (carbonyl groups), 1650-1500 cm^{-1} (C=C stretching), and 1300-1000 cm^{-1} (C-O stretching), confirming various oxygenated functional groups characteristic of graphene oxide. These findings indicate the sample likely contains a mixture of GO, graphite, and structural defects.

Table 1: List of peaks obtained for XRD test method 3: 500°C

No.	2θ (°)
1	18.2569
2	25.5058
3	26.7516
4	28.4913
5	34.9349
6	40.1818
7	53.3386
8	56.0439

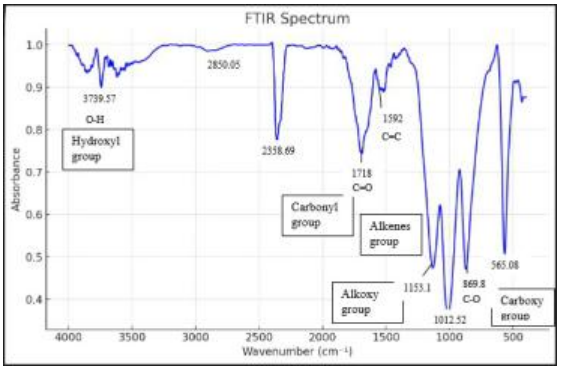

Fig. 2: FTIR results graph for method 3: 500°C.

The XRD analysis of the 600°C sample presents some ambiguity regarding the presence of graphene oxide (GO), with peaks at 25.33°, 26.52°, and 28.29° indicating a mix of graphite and reduced graphene oxide (rGO). However, the FTIR spectrum hints at the possibility of GO, with features such as broad O-H stretching at 3423 cm^{-1} (indicative of hydroxyl groups), prominent peaks at 1726 cm^{-1} (suggesting carbonyl groups), and 1581 cm^{-1} (potentially linked to aromatic groups), alongside C-H stretching in the range of 3000-2850 cm^{-1} and C-O stretching at 1076 cm^{-1}

Table 2: List of peaks obtained for XRD test method 3: 600°C

No.	2θ (°)
1	25.3346
2	26.524
3	28.2938
4	34.7722
5	40.4973
6	50.167

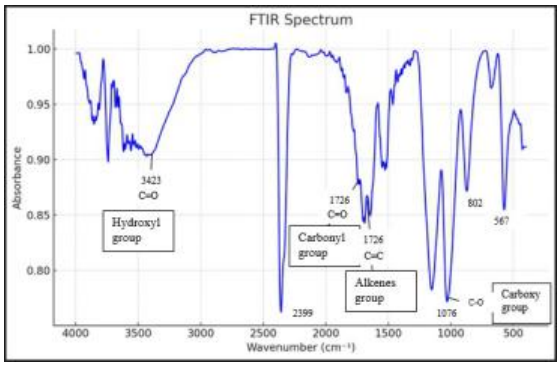

Fig. 3: FTIR results graph for method 3: 600°C.

4. Conclusions

This project demonstrates pineapple waste as a sustainable precursor for synthesizing graphene oxide (GO), providing an eco-friendly alternative to traditional graphite-based methods. The characterized GO shows similar properties to conventional GO, validating the synthesis process. This sustainable approach reduces waste and production costs, aligning with environmental and economic goals. Future research can optimize the method for consistent results and enhance sustainability by substituting strong acids with natural alternatives like tartaric acid, in line with green chemistry principles.

References

1. Kumar, V., Kumar, A., Lee, D.-J., & Park, S.-S. (2021). Estimation of number of graphene layers using different methods: a focused review. Materials, 14(16), 4590.
2. Hummers, W. S., Jr., & Offeman, R. E. (1958). Preparation of Graphitic Oxide. *Journal of the American Chemical Society*, *80*(6), 1339-1339. https://doi.org/10.1021/ja01539a017
3. Marcano, D. C., Kosynkin, D. V., Berlin, J. M., Sinitskii, A., Sun, Z., Slesarev, A., Alemany, L. B., Lu, W., & Tour, J. M. (2010). Improved Synthesis of Graphene Oxide. *ACS Nano*, *4*(8), 4806-4814. https://doi.org/10.1021/nn1006368

REGENERATION OF SODIUM BOROHYDRIDE (NABH4) BY BALL MILLING SODIUM METABORATE (NABO2) WITH MAGNESIUM: A SUSTAINABLE APPROACH FOR HYDROGEN STORAGE

Abstract: This research investigates the regeneration of sodium borohydride (NaBH4) through the ball milling process of sodium metaborate (NaBO2) with magnesium (Mg). The study explores the parameters aspects and efficiency of this regeneration method, aiming to enhance the reusability of NaBH4 as a hydrogen storage material. Experimental results and analysis contribute to a deeper understanding of the reaction kinetics and structural changes induced by ball milling, offering insights into the feasibility and optimization of this regeneration approach for sustainable hydrogen storage systems. Based on the experiments, it can be concluded that 15:1 for ball to powder ratio , 8:1 for Mg:NaBO2.4H2O ratio, ethanol as solvent and inert gas condition yields the highest yield weight percentage of 60.53%.

1. Research Background

The pressing need for cleaner, more sustainable energy sources has fueled research into better hydrogen storage devices. Because of its high hydrogen content, Sodium borohydride (NaBH4) has risen to the top of the list of promising options. However, the irreversible dehydrogenation process of Sodium metaborate (NaBO2), the byproduct of hydrogen generation using NaBH4 makes it unsuitable for practical use. In recent years, the synergistic coupling of ball milling and magnesium (Mg) has emerged as a new and efficient strategy for NaBH4 regeneration.

The purpose of this research is to thoroughly examine and understand the complex mechanisms involved in the ball milling-assisted regeneration of NaBH4 with Mg. We hope that by conducting a comprehensive investigation of the synergistic effects, we will be able to not only grasp the underlying principles driving this process, but also give insights that will pave the way for optimizing and scaling up NaBH4 regeneration. This research's possible consequences extend beyond the laboratory, offering promise for practical applications in hydrogen storage systems, which are critical components of the worldwide goal of a sustainable and carbon-neutral future.

2. Methodology

The methodology applied for this research are studying past attempts of other researchers to identify the most effective approaches from past results and then replicating the experiment by the same parameters used and carrying out multiple experiment with varying parameters to discover the most effective parameters. This process will then be repeated until the highest yield weight percentage is gained. The first step is analyzing past literature to gain the control parameters. Then, the parameters (ball to powder ratio, Mg to NaBO2.4H2O ratio, ….) are manipulated to find the set of parameters that yield the best results.

Tests (XRD, XRF) are done on materials that will be used for the research (NaBO2.4H20). Then, the weight of each material used is calculated based on the

desired ratio and measured before being put into the ball milling jar. Depending on the desired parameters, the preparation may be done under inert gases by using glove box. Then, the jar is sealed and sent to the lab for ball milling under 400 RPM for 12 hours. The ball mill machine used is laboratory ball mill. The condition during the ball milling process is kept under low humidity and 22-26ºC.

After the ball milling process is done, the samples are immersed in the solvent (Ethanol, THF, Methanol) for 3 hours to allow NaBH4 produced to dissolve in the solvent. Then the solution is filtered using filter paper. The solution is then heated in an oven at 80oC for 2 hours. The white powder obtained are then scraped from the crucibles and obtained. The samples collected are then weighed and sent to the lab for analysis by FTIR test. The results obtained are then analyzed to set the parameters for the next set of experiments.

3. Results and Discussions

Table 1: Samples Parameter

Sample	Ball to powder ratio (mass/g)	Mg to NaBO2.4H2O ratio (mole)	Solvent	Inert surrounding condition
1A	7:1	6:1	Ethanol	No
1B	10:1	6:1	Ethanol	No
1C	13:1	6:1	Ethanol	No
1D	15:1	6:1	Ethanol	No
2A	15:1	6:1	Ethanol	No
2B	15:1	8:1	Ethanol	No
2C	15:1	4:1	Ethanol	No
2D	15:1	10:1	Ethanol	No
3A	15:1	8:1	Ethanol	No
3B	15:1	8:1	Methanol	No
3C	15:1	8:1	THF	No
4A	15:1	8:1	Ethanol	No
4B	15:1	8:1	Ethanol	Yes

Table 2: Results of NaBH4 yield

Yield weight	1A	1B	1C	1D	2A	2B	2C
Theoretical (g)	0.5907	0.4134	0.4134	0.4134	0.6202	0.5296	0.7486
Experimental (g)	0.1822	0.1564	0.1922	0.2026	0.2926	0.2082	0.3241
Percentage (%)	30.85	37.83	46.52	49.04	47.18	52.90	43.30

Yield weight	2D	3A	3B	3C	4A	4B
Theoretical (g)	0.4620	0.5296	0.5296	0.5296	0.5296	0.5296
Experimental (g)	0.2274	0.2723	0.2703	0.2695	0.3022	0.3206
Percentage (%)	49.22	51.42	51.04	50.89	57.06	60.54

Based on the results gained, ball ratio 15:1, Mg:NaBO2.4H2O ratio 8:1, ethanol solvent and inert gas condition yield the highest mass percentage of NaBH4 produced from the reaction. Then, we analyze the yield using FTIR analysis to confirm the presence of NaBH4.

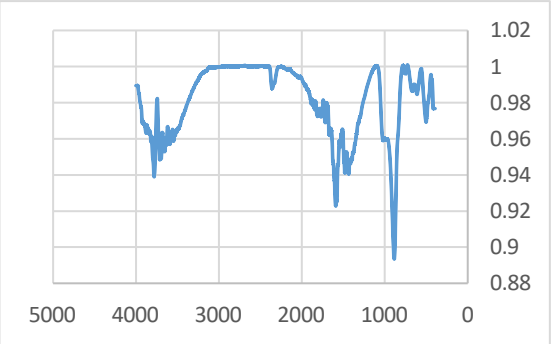

Figure 4.3: FTIR analysis of NaBH4 yield 1

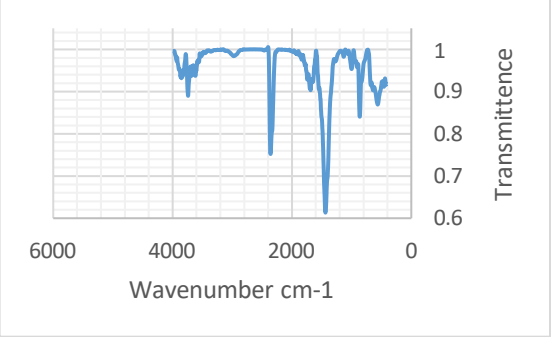

Figure 4.4: FTIR analysis of NaBH4 yield 2

To determine the presence of NaBH4, we need to look for peaks at ~2380 cm^{-1} and ~1150 cm^{-1}. Both samples analyzed produces peaks that fulfills above conditions. For both analysis 1 and 2, other substances that can be detected in the samples are ethanol, carbon dioxide and Magnesium oxide.

4. Conclusions

The regeneration of sodium borohydride (NaBH4) through ball milling of sodium metaborate (NaBO2) with magnesium although promising is still an unsustainable method in term of cost for hydrogen storage. This thesis report delved into the process of transforming sodium metaborate and magnesium into sodium borohydride, a key material for hydrogen storage applications. Through comprehensive experimentation and analysis, several key findings emerged. Firstly, the ball milling process proved to be an efficient means of promoting the reaction between sodium metaborate and magnesium, leading to the regeneration of NaBH4. This method offers advantages in terms of scalability and energy efficiency compared to traditional synthesis routes. When ball milling is done with 400rpm for 12 hours, it is found that 15 to 1 zirconia ball to powder ratio, 8 to 1 Magnesium to NaBH4.4H20 ratio, ethanol solvent and inert gas condition produce the highest NaBH4 yield weight percentage of 60.54%. Secondly, the sustainability aspect of this approach cannot be overlooked. By utilizing readily available such as sodium metaborate while producing little to almost no waste, this method aligns with the principles of green chemistry and offers a viable pathway for the large-scale production of NaBH4. Moreover, the characterization of the synthesized NaBH4 demonstrated its purity and suitability for hydrogen storage applications. This underscores the potential of the ball milling method as a reliable and practical means of NaBH4 regeneration.

In conclusion, the regeneration of sodium borohydride through ball milling of sodium metaborate with magnesium represents a significant advancement in the field of hydrogen storage. This sustainable approach offers a pathway towards addressing the challenges associated with the widespread adoption of hydrogen as a clean energy carrier. Further research and development in this area hold promise for unlocking the full potential of NaBH4 as a viable energy storage solution in the transition towards a more sustainable future.

References

1. Demirci, U. B. (2015). The hydrogen cycle with the hydrolysis of sodium borohydride: A statistical approach for highlighting the scientific/technical issues to prioritize in the field. *International Journal of Hydrogen Energy, 40*(6), 2673-2691. https://doi.org/10.1016/j.ijhydene.2014.12.067
2. Kalantzopoulos, G. N., Vitillo, J. G., Albanese, E., Pinatel, E., Civalleri, B., Deledda, S., Bordiga, S., Baricco, M., & Hauback, B. C. (2014). Hydrogen storage of Mg– Zn mixed metal borohydrides. *Journal of Alloys and Compounds, 615*, S702-S705. https://doi.org/10.1016/j.jallcom.2013.12.258
3. Lang, C., Jia, Y., Liu, J., Wang, H., Ouyang, L., Zhu, M., & Yao, X. (2017). NaBH 4 regeneration from NaBO 2 by high-energy ball milling and its plausible mechanism. *International Journal of Hydrogen Energy,42*(18), 13127-13135. https://doi.org/10.1016/j.ijhydene.2017.04.014
4. Liu, R., & Book, D. (2014). Mn-based borohydride synthesized by ball-milling KBH4 and MnCl2 for hydrogen storage. *International Journal of Hydrogen Energy, 39*(5), 2194-2200. https://doi.org/10.1016/j.ijhydene.2013.11.125
5. Zhang, J., Li, H., Xiao, X., & Ouyang, L. (2023). Preparation and regeneration of metal borohydrides for high-density hydrogen supply: Progress, challenges, and perspectives. *Journal of Alloys and Compounds, 951*. https://doi.org/10.1016/j.jallcom.2023.169887

GREEN SYNTHESIS OF GRAPHENE OXIDE

Abstract: This research is conducted to synthesize GO using HM and experiment with greener acids (acetic acid and wood vinegar) as substitutes for strong acids. Experiments include S1 (redo): HM, S3: HM with Acetic Acid, S4: HM with Wood Vinegar, and S4.2: HM with Wood Vinegar 2. Characterization methods include TGA, XRD, and Raman spectroscopy. S1 (redo) shows TGA Tmax at 275℃ and XRD peak at 18.2°. Raman confirms GO presence with G band at 1589 cm^{-1}, D band at 1347 cm^{-1}, and 2D band at 2751 cm^{-1}. Meanwhile, S3, S4, and S4.2 TGA Tmax values are 730℃, 735℃, and 930℃ respectively, with XRD peaks at 26.4° and 54.6°. GO was successfully produced only in S1. While other samples resulted in graphite due to the weak acids' low dissociation, insufficient for graphite oxidation. Thus, acetic acid and wood vinegar are not suitable substitution for strong acids.

1. Research Background

GO is a derivative of graphene which contains oxygen-containing functional groups (=O, -OH, -O-, -COOH) at the basal planes and edges of the plane, forming a mixture of sp^2 and sp^3 hybridized carbon atoms [1]. GO has several applications in gas barrier, water treatment, stimuli- responsive sensors, and anti-corrosive polymer coatings [2].

Furthermore, GO is the precursor of reduced graphene oxide (rGO), which has low solubility in water, slightly better thermal applications, superior electronic properties and highly customizable depending on applications [3], making it an emerging material in energy storage, biosensors, and in biomedical drug delivery system [4].

Synthesis of GO involves in using strong acids like sulfuric acid, phosphoric acid, or nitric acid as oxidizing agents. However, the process releases hazardous gas and ions such as nitrogen dioxide (NO_2), manganese cation (Mn^{2+}) and permanganyl ion (MnO_3+), into the surrounding environment. Considering the global trend towards green chemistry, limited studies are published on the use of environmentally friendly reagents. Hence, the feasibility and effectiveness of green organic acids will be investigated. The products obtained are characterized and discussion are made.

2. Methodology

S1(redo): Hummers' Method (HM)

Table 1: S1(redo) Procedure

	Concentration	Quantity	Mixing Order	Time (min)
H_2SO_4	95-98 %	67.5 ml	1	30
H_3PO_4	85 %	10 ml		
HNO_3	65-68 %	22.5 ml		
Graphite powder	< 20 μm	1 g		
$KMnO_4$	-	6 g	2	120
Distilled water	-	100 ml (batch 1) + 120 ml (batch 2)	3, 4	60
H_2O_2	30 %	15 ml	4	30

S3: HM with Acetic Acid

Table 1: S3 Procedure

	Concentration	Quantity	Mixing Order	Time (min)
Acetic acid, CH_3COOH	>99.8 %	100 ml	1	30
Graphite powder	<20 μm	1 g		
$KMnO_4$	-	6 g	2	120
Distilled water	-	100 ml (batch 1) + 120 ml	3, 4	60

		(batch 2)		
H_2O_2	30 %	15 ml	4	30

S4: HM with Wood Vinegar

	Concentration	Quantity	Mixing Order	Time (min)
Wood vinegar	30.00 %	100 ml	1	30
Graphite powder	<20 μm	1 g		
$KMnO_4$	-	6 g	2	120
Distilled water	-	100 ml (batch 1) + 120 ml (batch 2)	3, 4	60
H_2O_2	30 %	15 ml	4	30

Fig. 3: S4 Procedure

S4.2: HM with Wood Vinegar 2

	Concentration	Quantity	Mixing Order	Time (min)
Wood vinegar	30.00 %	50 ml	1	30
Powder from S4	-	0.5 g		
$KMnO_4$	-	3 g	2	120
Distilled water	-	50 ml (batch 1) + 60 ml (batch 2)	3, 4	60
H_2O_2	30 %	7.5ml	4	30

Fig. 4: S4.2 Procedure

3. Results and Discussions

S1(redo): Hummers' Method (HM)

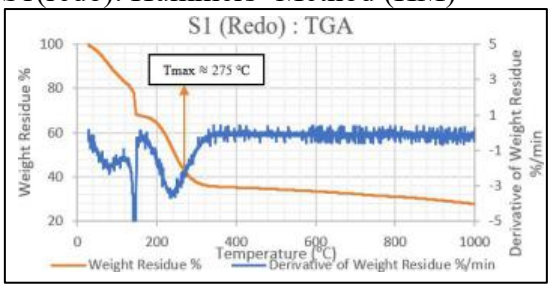

Fig. 5: S1(redo) TGA

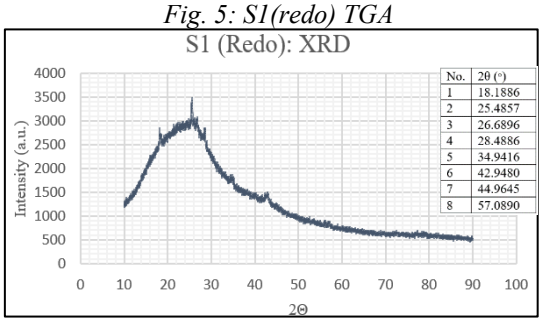

Fig. 6: S1(redo) XRD

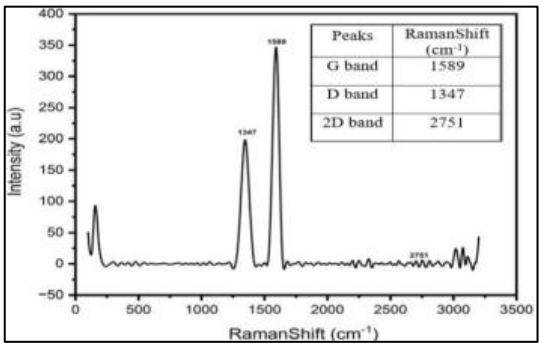

Fig. 6: S1(redo) Raman

S1(redo) successfully yielded GO and is verified from TGA (Tmax at 275 °C), XRD (18.2°) and 532nm Raman (G band = 1589 cm^{-1}, D band = 1347 cm^{-1}, and 2D = 2751 cm^{-1}). Raman also reveals that the GO has high level of defects since the intensity ratio of D and G band are high (1.75). Theoretical value of GO is 250–300 °C for TGA' Tmax, 16–19° for XRD's 2θ, Raman G band = 1852 cm^{-1}, D band = 1350 cm^{-1}, and 2D = 2685 cm^{-1}.

S3: HM with Acetic Acid

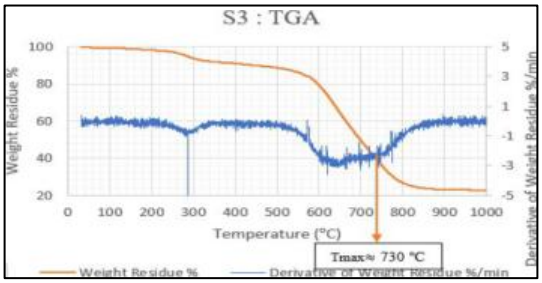

Fig. 7: S3 TGA

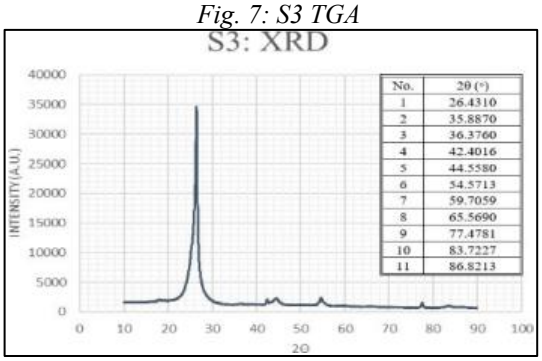

Fig. 8: S3 XRD

S3 did not yield GO. Instead, graphite is yielded based on the TGA (Tmax at 730℃) and XRD (2θ at 26.4°) results. Theoretical values of graphite are 841–949 °C for TGA's Tmax, and 26.7° for XRD's 2θ.

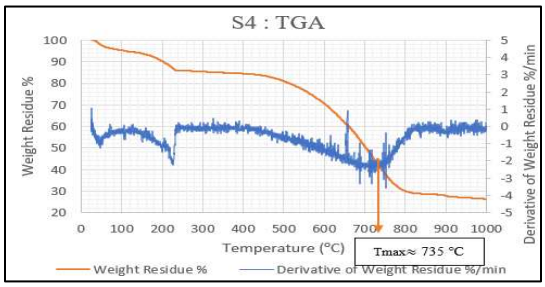

Fig. 9: S4: HM with Wood Vinegar. S4 TGA

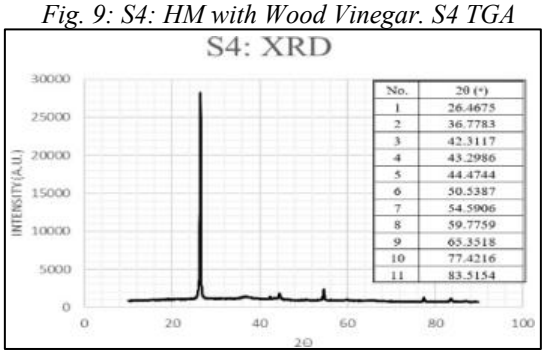

Fig. 10: S4 XRD

S4 did not yield GO. Instead, graphite is yielded based on the TGA (Tmax at 735℃) and XRD (2θ at 26.5°) results

S4.2: HM with Wood Vinegar 2

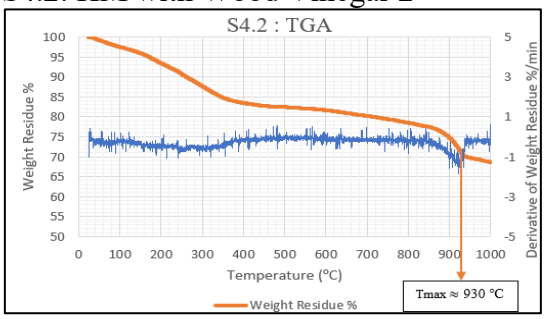

Fig. 11: S4.2 TGA

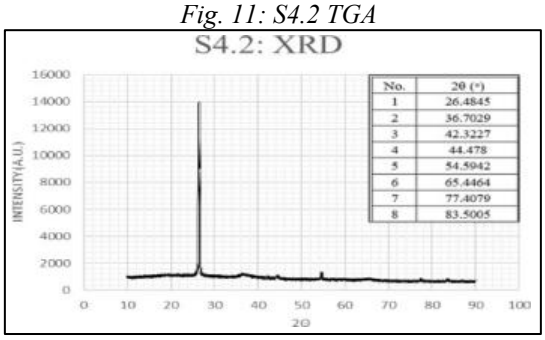

Fig. 12: S4.2 XRD

S4.2 did not yield GO. Instead, graphite is yielded based on the TGA (Tmax at 930℃) and XRD (2θ at 26.5°) results

4. Conclusions

In conclusion, conventional method, S1 (redo) successfully yielded GO. But S3, S4, and S4.2 did not yield GO and were identified as graphite. Therefore, acetic acid and wood vinegar are not suitable substitutes for strong acids. This is due to the weak dissociation degree of hydrogen ion of the weak acids, which are not sufficient to oxidize graphite.

References

1. Yang, G., Li, L., Lee, W. B., & Ng, M. C. (2018). Structure of graphene and its disorders: a review. *Science and Technology of Advanced Materials*, *19*(1), 613-648. https://doi.org/10.1080/14686996.2018.1494493
2. Smith, A. T., LaChance, A. M., Zeng,S., Liu, B., & Sun, L. (2019). Synthesis, properties, and applications of graphene oxide/reduced graphene oxide and their nanocomposites. *Nano Materials Science*, *1*(1), 31-47. https://doi.org/https://doi.org/10.1016/j.nanoms.2019.02.004
3. Jiříčková, A., Jankovský, O., Sofer, Z., & Sedmidubský, D. (2022). Synthesis and Applications of Graphene Oxide. *Materials (Basel, Switzerland)*, *15*(3), 920. https://doi.org/10.3390/ma15030920
4. Kumar, A., Kumar, N., Sharma, Y., Leu, J., & Tseng, T. Y. (2019). Synthesis of Free-Standing Flexible rGO/MWCNT Films for Symmetric Supercapacitor Application. *Nanoscale Research Letters*, *14*(1), 266. https://doi.org/10.1186/s11671-019-3100-1

DESIGN OF AN AFFORDABLE MOTORIZED WHEELCHAIR USING SUSTAINABLE MATERIALS

Abstract: To address the gap between motorized and affordable wheelchairs while promoting sustainability, a study was conducted to develop an affordable motorized wheelchair using sustainable materials. Current market options are often too expensive, limiting accessibility. The project aimed to enhance mobility for all users, leveraging the benefits of motorized systems over traditional ones. Sustainable materials were prioritized to align with Sustainable Development Goals (SDG) 7, 11, and 12. Extensive research determined the best materials, design, and motor systems, resulting in a wheelchair made primarily of rattan. Theoretical calculations and simulations, including torque requirements, were completed, and a scale model was fabricated and successfully tested, demonstrating the prototype's viability.

1. Research Background

Wheelchairs are widely used globally, with motorized versions gaining prominence due to technological advances. However, motorized wheelchairs are expensive, with the lowest price in the Malaysian market being RM1450. This high cost, primarily due to materials, makes them unaffordable for many who need them. This research aims to design an affordable motorized wheelchair using sustainable materials like bamboo and rattan to reduce production costs and lower the price.

This research provides sustainable material used, along with the complete design and also a theoretically working motor system. And the cost of all of that is also being provided so as to meet the affordable part of the objective. Also, a prototype with scale 1:3 also had been fabricated to prove the concept of this project

2. Methodology

Sustainable materials support social responsibility, ecological balance, and economic viability throughout their life cycle. They are produced with minimal energy and water, sourced from renewables, and designed for safe biodegradation, recycling, or repurposing. These materials aim to reduce the environmental impact of traditional manufacturing and consumption. Globally, material production and consumption face environmental constraints, such as biodiversity loss, land-use changes, climate impacts, and biogeochemical disruptions (1)

For the design and simulation, SolidWorks software was used. Initially, individual parts of the wheelchair were designed and then assembled to form the complete structure. For simulation, the properties of rattan were studied and applied to analyze the von Mises stress of the wheelchair. (2),(3) and (4).

Property	Value	Units
Elastic Modulus	1303.36	N/mm^2
Poisson's Ratio	0.4896	N/A
Shear Modulus	416.3	N/mm^2
Mass Density	350	kg/m^3
Tensile Strength	42	N/mm^2
Compressive Strength	24.93	N/mm^2
Yield Strength	58.46	N/mm^2
Thermal Expansion Coefficient		/K
Thermal Conductivity	0.05	W/(m·K)
Specific Heat		J/(kg·K)

Fig. 1: Properties of rattan applied in SolidWorks

The calculation for the motor specifications is crucial, requiring the determination of necessary force. Valid formulas, tested by the author in their research paper, were utilized for this purpose. These formulas,

including the main one for determining required force, will guide the selection of an appropriate motor for the project (3).

$$Tw[Nm] = TTE[N] * Rw * RF \ldots\ldots\ldots [1]$$

Following the design phase, a prototype of the wheelchair was fabricated at a scale of 1:3. The materials for the prototype were chosen based on factors like strength-to-weight ratio, availability, cost, and ease of fabrication. Design considerations included user convenience, maintenance ease, and aesthetic appeal.

3. Results and Discussions

A comprehensive comparison was conducted to identify the most suitable material for the project, with a focus on sustainability. Four sustainable materials were shortlisted, and their pros and cons were analyzed and listed in a table. Rattan emerged as the preferred material due to its renewable sources, sustainability, excellent strength-to-weight ratio, and flexibility. Despite potentially higher initial costs compared to wood and bamboo, its durability ensures long-term viability, making it the ideal choice for the project.

Table 1: Comparison between sustainable materials

Materials	Pros	Cons
Rattan	Have a good strength. Flexible. High availability. Lightweight.	Weaker than wood. Natural rattan not waterproof. Cost more than bamboo and wood.
Bamboo	Stronger than rattan. Easy to grow. Lightweight. Waterproof. Relatively cheap.	Not flexible. Limited design of structure.
Wood	Stronger than bamboo and rattan. Can be shaped easily into desired design. Relatively cheap.	Heavy. Not flexible. Not suitable for wheelchair.
Aluminium	Highly resistant to corrosion. Lightweight. High strength to weight ratio.	Energy-intensive production. Higher initial cost. Thermal conductivity.

The von Mises Stress analysis depicted in Figure 2 provides crucial values indicating whether the material or structure is at risk of fracturing. Based on this analysis, it is evident that the structure can effectively withstand a total force of 1000N, applied perpendicular to the main frame. The accurate fix constraint points between the wheel and axle ensure precise results.

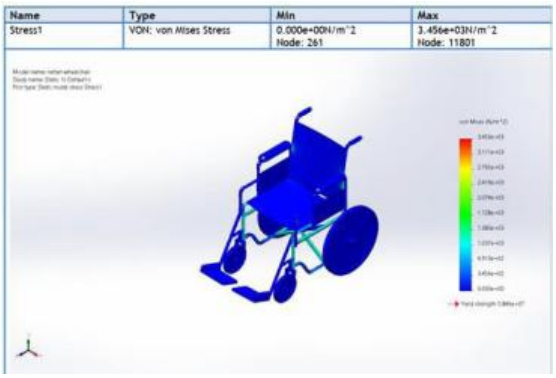

Fig. 2: Simulation of von Misses stress using SolidWorks

For the fabrication, a scale model of 1:3 has been made. It comes with a wireless motor system where the user can control the wheelchair using Bluetooth controller such as tablet. The prototype also comes with a movable seat to enhance the overall experience of the user.

Fig. 3: Prototype with its Bluetooth controller

4. Conclusions

This thesis aimed to create an affordable motorized wheelchair using sustainable materials. The project successfully developed a cost-effective design with adjustable seats, and user-friendly controls. Extensive research identified materials like natural fiber composites, such as rattan, and biodegradable polymers, promoting sustainability. The result is a wheelchair accessible to low- and middle-income populations, advancing assistive technology and sustainable engineering.

References

1. Olivetti, E. A., & Cullen, J. M. (2018). Toward a sustainable materials system. Science, 360(6396), 1396-1398.
2. Yang, S., Xiang, E. l., Shang, L., Liu, X. e., Tian, G., & Ma, J. (2020). Comparison of physical and mechanical properties of four rattan species grown in China. *Journal of Wood Science, 66*(1), 3. doi:10.1186/s10086-020-1850-0
3. Adewuyi, A. P., Otukoya, A., Olaniyi, O., & Olafusi, O. (2015). Comparative Studies of Steel, Bamboo and Rattan as Reinforcing Bars in Concrete: Tensile and Flexural Characteristics. Open Journal of Civil Engineering, 5, 228-238. doi:10.4236/ojce.2015.52023
4. Osoka. (2015). Optimum Conditions for Mercerization Rattan Palm Fibre.
5. Sutradhar, A., Sunny, M. S. H., Mandal, M., & Ahmed, R. (2017, 7-9 Dec. 2017). Design and construction of an automatic electric wheelchair: An economic approach for Bangladesh. Paper presented at the 2017 3rd International Conference on Electrical Information and Communication Technology (EICT).

CHAPTER 5

Corrosion and Surface Engineering

Heat Exchanger Fouling Mitigation by Applying Thermal Conductive Coatings on Heat Transfer Surfaces

The Effect of Heat Treatment of WE43 on Corrosion Behaviour for Biomedical Applications

Understanding Corrosion Behavior of Steel Alloys in Different Environments of The Oil and Gas Industry with The Addition of Corrosion Inhibitors

Application of Titanium Oxide Thin Film on Structured Heat Exchanger Surface for Enhancing Heat Transfer and Fouling Mitigation

Preface

The challenges posed by fouling, corrosion, and material degradation in industrial and biomedical applications call for innovative solutions to enhance performance, sustainability, and safety. This collection of studies highlights efforts to address these pressing issues through material science, surface engineering, and corrosion inhibition. The first study investigates titanium coatings on brass heat exchanger tubes to mitigate calcium carbonate fouling. By analyzing fouling resistance, heat transfer coefficients, and morphological structures via advanced imaging techniques, the research demonstrates how titanium coatings can significantly improve thermal performance and reduce fouling, offering a promising avenue for enhancing industrial heat exchanger efficiency. The second study explores the corrosion behavior and mechanical properties of WE43 magnesium alloys for temporary biomedical implants. By comparing treated and untreated WE43 with other materials, the research identifies optimal conditions for corrosion resistance and mechanical support. These findings align with the critical requirements for temporary implants, presenting WE43 as a strong candidate for medical applications while pointing to opportunities for further refinement. In the third study, the focus shifts to the corrosion dynamics of carbon steel and the efficacy of Kalmegh solution as a corrosion inhibitor in sodium chloride and sodium hydroxide environments. The results underscore the potential of Kalmegh solution to significantly reduce corrosion rates, paving the way for environmentally friendly and cost-effective corrosion mitigation strategies in industrial settings. The fourth study delves into the use of titanium dioxide coatings to combat fouling in heat exchangers. Through rigorous testing and comparative analysis, it demonstrates how these coatings enhance resistance to fouling, reduce maintenance demands, and improve heat transfer efficiency. The findings validate titanium dioxide as a viable and durable solution to one of the most persistent problems in heat exchange systems. Together, these studies exemplify the application of cutting-edge research to address industrial and biomedical challenges. By focusing on material innovation and sustainable solutions, they contribute to advancing technologies that improve efficiency, reliability, and environmental compatibility.

HEAT EXCHANGER FOULING MITIGATION BY APPLYING THERMAL CONDUCTIVE COATINGS ON HEAT TRANSFER SURFACES

Abstract: Fouling is a problem that is bothersome in many industrial heat exchangers as it retards the performance of heat exchange. The presence of deposits such as $CaCO_3$ on the heat exchanger surface causes deterioration in performance caused by the deposits formed which possess low thermal conductivity. In this study, we will be using the titanium coating on the brass specimen heat exchanger tubes surface and investigate the heat transfer and mitigation of
$CaCO_3$. The fouling resistance and overall heat transfer coefficient of the uncoated brass specimen has been recorded after a 72-hour experiment with synthetic saltwater solution containing 0.3g/l $CaCO_3$solution was utilized to simulate the fouling environment. The EDTA complexometric titration checks the calcium cation concentration in the fouling solution every six hours and is added to it every six hours. Based on the results obtained, the mass of
$CaCO_3$ deposited is 0.1734g for uncoated surface and 0.0863g for coated surface. The fouling resistance for uncoated surface is higher than coated surface and the overall heat transfer coefficient for uncoated surface is lower than coated surface. The test specimen was also observed via FESEM to gain a better understanding of the morphological structure. Ti coated brass surface shows less deposition and a better overall heat transfer coefficient.

1. Research Background

In the 21st century, heat exchangers have become crucial in reducing energy consumption and optimizing new energy resources. Their importance spans various applications, from home air conditioning and refrigerators to large-scale power generation. Advances in heat exchanger technology and design have made them ideal for applying thermodynamic principles. A heat exchanger transfers heat energy between two mediums, which can be gases, liquids, or both, through conduction. It maximizes thermal exchange efficiency while minimizing fluid flow resistance and prevents the mixing of the two fluids, which typically have high flow rates to facilitate heat transfer.

1.1 Research Objectives

Water is often used as the medium for heat exchange in various industries, leading to fouling from mineral and substance deposits on the heat exchange surface.Fouling reduces heat transfer efficiency, increases pressure drops, and can cause structural failure. Industries mitigate this by periodically halting production for cleaning, which increases costs. Improper cleaning can irreversibly damage the surface. Researchers are exploring solutions like applying titanium oxide thermal conductive coatings on heat exchanger tubes to prevent fouling. These coatings are tested in a fouling rig with mineral salts to evaluate their performance. The results are studied to determine the correlation of heat transfer and fouling mitigation effects with the thermal conductive coating for comparison with the available data.

2. Methodology

Fouling can be observed on the heat exchanger surface in a variety of ways. Fouling that occurs can be categorized into multiple groups, depending on the physical or chemical process that happens on the heat transfer surface. The most well know and common types of fouling are particulate fouling, chemical fouling, corrosion fouling, solidification fouling, biological fouling, and crystallization fouling are a few of the fouling types that can happen. Fouling formation on the heat exchanger surface can be split up into the deposition process and the removal process. It can be summarized as the figure shown below. The stages of fouling can be divided into 5 stages which are initiation, transport, attachment, removal and aging.

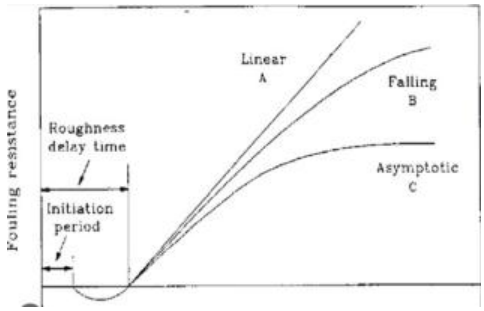

Figure 2.1: Types of fouling curves

Factors that affect fouling are the flow rate, temperature, material of heat exchanger, pH value of fluid, and presence of impurities in fluid. Among the fouling mitigation techniques include chemical method, surface anti-fouling coating, liquid-side mitigation strategies. There are several types of fouling models such as Watkinson model, Kern and Seaton model, Ritter model and Hasson model.

Research on fouling and the improvement of fouling models in heat exchangers continues due to the complex nature of deposit formation and measurement of fouling resistance. Various models have been proposed for different types of fouling, but simplifying assumptions are often made to manage this complexity. These assumptions include neglecting changes in the physical properties of fluids, surface roughness, and the form of deposits, as well as considering only one type of fouling and assuming homogeneity of the fouling layer.

Efforts to replicate the initiation and roughness delay periods in fouling have led to models predicting fouling after the main delay period. Key parameters investigated in fouling studies include flow velocity, bulk temperature, time, and concentration. The process of fouling is viewed as the net result of deposition and removal processes, expressed mathematically as:

$$\frac{dm}{dt} = m_f = m_d - m_r$$

The deposition rate depends on the type and mechanism of fouling, while the removal rate is influenced by the adhesion strength of the deposits and the shear stress caused by flow velocity. Several fouling models have been developed to assess the impact of fouling on heat exchanger performance under specific operating conditions.

3. Results and Discussions

Physical vapor deposition (PVD), also known as physical vapor transport, is a vacuum deposition method used to create thin films of coating on substrates like metal and polymers. This process involves the substance transitioning from a condensed phase to a vapor phase and then back to a condensed phase to form a thin film. For developing titanium deposits on brass surfaces, radiofrequency reactive magnetron sputtering is used. In this process, titanium and argon gas, both with 99.999% purity, are utilized, with argon serving as the carrier gas. An axial rotating chuck at a speed of 5 rpm ensures uniform coating thickness. After the coating, the specimen is stored in a desiccator for use in heat transfer applications. For preparation of bulk solution, calcium chloride is reacted with sodium bicarbonate to produce calcium carbonate,

sodium chloride, water and carbon dioxide. Below is the chemical reaction:

$$CaCl2 + 2NaHCO3 \rightarrow CaCO3 + 2NaCl + H2O + CO2$$

Table 3.1: Preparation of calcium carbonate solution

Components	$CaCl_2$	$NaHCO_3$	$CaCO_3$
Molar mass	110.9054	168.002	100.089
Molar mass ratio(g/mol)	1.108	1.6785	1
Mass for 1 litre,(g)	0.3324	0.5035	0.3
Mass for 7 litre,(g)	2.332	3.549	0.3

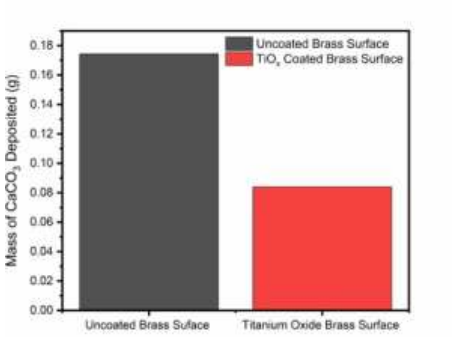

Figure 3.1: Mass of calcium carbonate deposited

Based on the results after the experiment, the amount of calcium carbonate deposited for uncoated brass surface is higher than Ti coated brass surface. The fouling resistance for uncoated is higher than coated surface and this theory is correct as the overall heat transfer coefficient for uncoated brass surface is lower than coated brass surface.

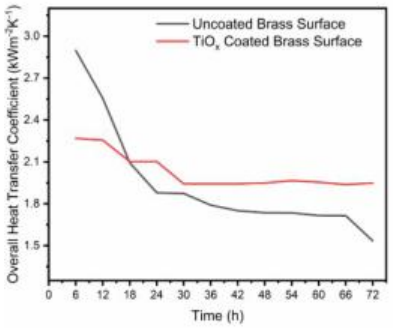

Figure 3.2 Graph of overall heat transfer coefficient

FESEM test was conducted to investigate the morphological surface of specimen. The uncoated brass specimen showed a higher density of calcium carbonate pellets size with high density while Ti coated surface showed lower density with most deposition size small and flaky.

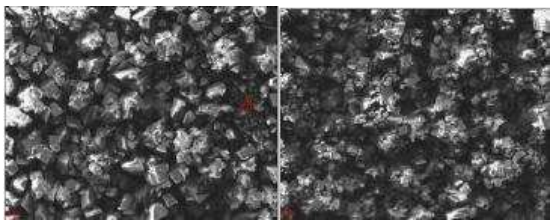

Figure 3.3: FESEM on uncoated brass surface(left) and Ti coated brass surface(right)

For uncoated specimen, it is found nearly 90% of calcium carbonate is deposited while only 41.23% of calcium carbonate is deposited in the Ti coated brass specimen. This shows that Ti coated brass specimen retards the deposition this prolonging the heat exchanger life.

4. Conclusions

In summary, titanium oxide coating was applied to brass surfaces using physical vapor deposition to reduce fouling. The coated brass showed lower fouling resistance and a higher overall heat transfer coefficient compared to uncoated brass. The coating decreases the deposition rate, enhancing heat transfer efficiency. Additionally, the titanium oxide layer protects the brass surface from corrosion, thereby extending the heat exchanger's lifespan. To improve the accuracy of fouling data and calcium ion deposition rates, the experiment should be extended beyond 72 hours. A longer experiment duration would yield more precise data and likely result in a higher heat transfer coefficient. Additionally, exploring other coating methods, such as chemical vapor deposition or electrolysis, could provide more effective anti-fouling coatings.

References

1. Oon CS, Kazi SN, Hakimin MA, Abdelrazek AH, Mallah AR, Low FW, et al. Heat transfer and fouling deposition investigation on the titanium coated heat exchanger surface. Powder Technol. 2020;373:671–80. https://doi.org/10.1016/j.powtec.2020.07.010.

THE EFFECT OF HEAT TREATMENT OF WE43 ON CORROSION BEHAVIOUR FOR BIOMEDICAL APPLICATIONS

Abstract: Magnesium alloys like WE43 are promising for temporary implants, avoiding the complications of secondary surgeries. WE43 boasts excellent mechanical properties, but in vitro studies show that prolonged immersion leads to accelerated corrosion. This project examines the effects of solid solution and aging treatments on WE43 to improve its suitability as a temporary implant by comparing with as-cast WE43, AZ91, and high-purity magnesium. Corrosion behaviours is tested via immersion in Hank's solution, mimicking body electrolytes, and mechanical properties are assessed using the Vickers hardness test. Microstructural analysis is conducted with optical microscopy (OM), scanning electron microscopy (SEM), and energy-dispersive X-ray spectroscopy (EDS). The study concludes that treated WE43 aligns well with healing processes and offers adequate support, though more precise methods could enhance future research results.

1. Research Background

Among the primary categories which are metals, ceramics, polymers, and composites, metallic materials are favoured for load-bearing applications. However, the need for secondary surgeries to remove stainless steel or titanium implants in small fractures is both costly and inconvenient. Biodegradable materials like magnesium and its alloys present a promising alternative, as they are naturally absorbed by the body post-healing.

Despite their advantageous mechanical properties, magnesium-based biomaterials face significant challenges, including rapid corrosion, hydrogen gas production, and elevated local pH levels. Consequently, extensive research has focused on managing the corrosion behaviours of magnesium alloys. This study aims to explore the impact of heat treatment on the corrosion behaviours and mechanical properties of the WE43 magnesium alloy, comparing it with high-purity magnesium and AZ91, to evaluate its suitability for temporary implant applications.

2. Methodology

WE43, AZ91 and high purity magnesium (HP Mg) were cut using CNC EDM wirecut having dimensions around 10x10x5mm$^{3.}$ The WE43 were separated into different types of heat treatment process as in Table

1. Solid solution treatment using 525°C for 8 hours while aging treatment using 250°C and variables duration after quenching in room temperature based on previous research [3]. After heat treatment, all materials were ground with 1200 grit abrasive paper, washed with distilled water, and dried in a desiccant environment.

Table 1: Different heat treatment process for WE43

Heat Treatment Process of WE43	Label	Aging Duration
Without heat treatment	A	
Solid solution treatment only	B	
Solid solution treatment and Aging	C	1 hour
Solid solution treatment and Aging	D	4 hours
Solid solution treatment and Aging	E	8 hours
Solid solution treatment and Aging	F	12 hours

Corrosion behaviours were analysed through immersion tests in Hanks' Balanced Salts (H1387) with sodium bicarbonate and distilled water. The surface area of each sample was recorded before each sample was hung with fishing line in

200 ml of solution in a 250 ml beaker, and hydrogen was collected in a burette above the sample at 37°C for 14 days as shown in Fig. 1.

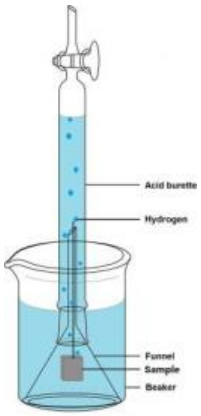

Fig. 1: The experimental setup for immersion test

The corrosion rate, P_{AH} (mm/year) was calculated using Eq 1 [2].

$$P_{AH} = 2.279V_H \ldots. (1)$$

where V_H is the hydrogen evolution rate, calculated by dividing the total hydrogen volume by immersion time. The corroded surfaces were observed with scanning electron microscopy (SEM) and energy-dispersive X-ray spectroscopy (EDS).

For microstructure study, all samples were ground on 800, 1000, and 1200 grit abrasive papers, then polished before etched in a nital solution (3ml nitric acid in 97ml ethanol) for 5 seconds, then analysed using optical microscope (OM).

The mechanical properties were assessed using hardness test on a Vickers hardness testing machine, and the results were compared among all materials.

3. Results and Discussions

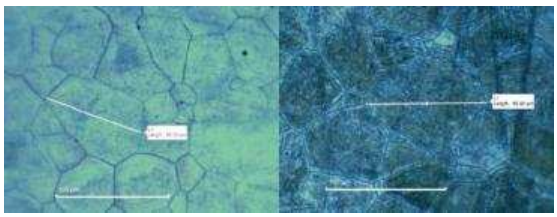

Fig. 2: Microstructure of as-cast WE43(left) and solid solution treated and aged WE43

The grain structure solution treated and aged WE43 becomes more complex, featuring a mix of refined grains and precipitates compared to as cast WE43 as shown in Fig 2. The heat treatment causes the grain size to increase, possibly due to overaging [1].

Table 2: Corrosion rate and Vickers hardness test result for all samples

Material	Corrosion Rate (mm/y)	Vickers Hardness Test (HV)	% Diff of Hardness from As-cast WE43 (%)
HP Mg	0.4771	38.52	
AZ91	0.3226	75.01	
WE43 A	0.0913	109.53	
WE43 B	2.8835	81.84	25.28
WE43 C	1.5200	99.03	9.59
WE43 D	0.5333	95.47	12.84
WE43 E	0.0633	83.09	24.14
WE43 F	1.7696	78.05	28.74

The corrosion rate from the immersion test gave the following ranking: WE43 E < WE43 A < AZ91 < HP Mg < WE43 D < WE43 C < WE43 F < WE43 B as shown in Table 2. The as-cast microstructure of WE43, with its mix of α-Mg dendrites and intermetallic phases, offers excellent corrosion resistance due to a stable protective surface layer. In contrast, AZ91, containing aluminium and zinc, has a coarse secondary eutectic β phase ($Mg_{17}Al_{12}$) that reduces corrosion but can cause localized grain boundary corrosion. HP Mg lacks these protective phases, resulting in higher corrosion rates.

WE43 B shows the highest hydrogen evolution and rapid corrosion due to the dissolution of protective intermetallic phases during solution treatment, increasing susceptibility to corrosion. Aging post-solution treatment (WE43 C, D and E) improves corrosion resistance, with optimal aging (8 hours) exhibiting the lowest corrosion rates due to fine, uniformly distributed phases enhancing protective properties as shown in Fig. 3 with highlights the presence of Yttrium (Y) and Neodymium (Nd) in Fig. 4 [1].

However, prolonged aging (WE43 F) increases corrosion rates due to precipitate coarsening and micro-galvanic cells. The unexpectedly high corrosion rates in heat-treated conditions might be due to experimental errors or residual stresses and defects from the treatments, despite heat treatment generally improving corrosion resistance by refining secondary phase particles and reducing galvanic cell formation.

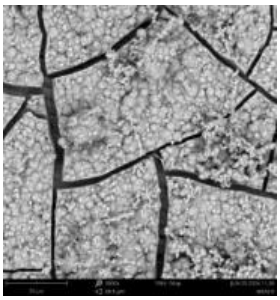

Fig. 3: The corroded surface of WE43 after immersion test for 14 days using SEM at 3000× magnification

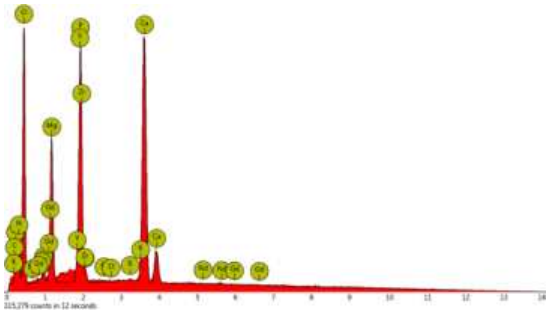

Fig. 4: EDS results of corroded surface WE43 E

Therefore, WE43 E is the best choice, with a corrosion rate of 0.06 mm/y and hardness of 83 HV, aligning with literature requirements for healing processes and structural support [2,3].

4. Conclusions

This study effectively applied solid solution heat treatment and aging treatment to WE43, comparing its properties to as-cast WE43, AZ91, and high-purity magnesium. The findings indicated that solid solution treatment followed by aging generally improved corrosion resistance by promoting the precipitation of fine, uniformly distributed phases. This act as effective barriers against corrosion propagation and refine the grain structure to reduce galvanic coupling. An optimal aging duration of 8 hours (WE43 E) yielded the lowest corrosion rate, making it the most suitable material among the conditions tested for temporary implants. Furthermore, the hardness of WE43 E which lower than that of as-cast WE43, suggested an increase in ductility, which is beneficial for reducing stress shielding and brittleness in orthopaedic applications. The study demonstrated that solid solution and aging treatments can significantly improve the corrosion behaviour and hardness of WE43, making it a promising material for temporary implant applications.

References

1. Yang, C., Gupta, N., Ding, H., & Xiang, C. (2020). Effect of Microstructure on Corrosion Behavior of WE43 Magnesium Alloy in As Cast and Heat-Treated Conditions. *Metals*, *10*(11), 1552. https://www.mdpi.com/2075-4701/10/11/1552
2. Zainal Abidin, N. I., Atrens, A. D., Martin, D., & Atrens, A. (2011). Corrosion of high purity Mg, Mg2Zn0.2Mn, ZE41 and AZ91 in Hank's solution at 37°C. *Corrosion Science*, *53*(11), 3542-3556. https://doi.org/https://doi.org/10.1016/j.corsci.2011.06.030.
3. Zhang, J., Han, S., Sun, Y., Chen, X., Chen, P., Li, Z., Huang, G., & Pan, F. (2023). Enhanced strength of WE43 magnesium-rare earth alloy via combining extrusion and aging. *Materials Science and Engineering: A*, *880*, 145329. https://doi.org/https://doi.org/10.1016/j.msea.2023.145329

UNDERSTANDING CORROSION BEHAVIOR OF STEEL ALLOYS IN DIFFERENT ENVIRONMENTS OF THE OIL AND GAS INDUSTRY WITH THE ADDITION OF CORROSION INHIBITORS

Abstract: This research investigates the corrosion dynamics of carbon steel, focusing on the influence of environmental factors and the efficiency of Kalmegh solution as a corrosion inhibitor. The study examines the impact of varying concentrations of sodium chloride (NaCl) and sodium hydroxide (NaOH) solutions on corrosion rate of carbon steel. Key objectives include evaluating the effectiveness of different Kalmegh solution concentrations in reducing corrosion rates in these environments. The research involves immersion and potentiodynamic polarization tests, along with surface characterization using Optical Microscope. Findings indicate that corrosion rates initially increase and then decrease with higher concentrations of sodium chloride and sodium hydroxide while increased Kalmegh solution concentrations consistently reduce corrosion rates.

1. Research Background

1.1 Introduction

Corrosion is a significant challenge in petroleum refineries due to exposure to corrosive gases and seawater, which can compromise equipment integrity [1]. The use of corrosion inhibitors is vital for mitigating these effects and ensuring the durability of carbon steel alloys in various environments.

1.2 Research Objectives

This study aims to understand the effect of various concentrations of NaCl and NaOH solutions on corrosion behavior of carbon steel. It also investigates the effectiveness of different concentrations of Kalmegh solution as a corrosion inhibitor in these varying conditions.

2. Methodology

2.1 Samples and Solutions Preparation

A516 carbon steel alloy samples were initially polished with fine grade sandpapers (P180 to P1200), with acetone used to prevent scratches. The samples are ultrasonically cleaned to remove small particles.

NaCl solutions of 1M, 2M, and 3M were prepared by dissolving 29.22g, 58.44g, and 87.66g of NaCl powder, respectively, in 500ml of distilled water. Similarly, NaOH solutions were prepared by dissolving 20g, 40g, and 60g of NaOH powder in 500ml of distilled water. Kalmegh solution was prepared by grinding Kalmegh coarse powder, soaking 10g, 20g, and 30g of the powder in 90ml, 80ml, and 70ml of distilled water respectively, stirring the mixture for 24 hours, and then filtering it for use.

2.2 Weight Loss (Immersion) Test

Three alloy samples are weighed and immersed in 100ml of varying concentrations of NaCl and NaOH solutions, with and without Kalmegh solution, for 14 days. Post immersion, the samples are treated with hydrochloric acid, cleaned, weighed, and the corrosion rate is calculated. The corrosion rate (C_R) formula is as shown below.

$$C_R \text{ (mm/y)} = \frac{87.6 \times w}{atD} \ldots. (1)$$

2.3 Polarization Test

Electrochemical tests using a three-electrode cell setup with a carbon steel alloy working electrode, platinum counter electrode, and standard calomel reference electrode were conducted with 1M, 2M and 3M NaCl and NaOH solutions, both with and without Kalmegh solution, to obtain polarization curves. Tafel extrapolation was performed using EC Lab software to determine corrosion potential (E_{corr}) and corrosion current density (I_{corr}) from the polarization curves.

3. Results and Discussions

3.1 Weight Loss (Immersion) Test

The weight loss tests indicate that corrosion rates increase from 1M to 2M but decrease from 2M to 3M concentrations of NaCl and NaOH, aligning with past research that attributes this trend to decreased oxygen solubility at higher salt concentrations [2]. The presence of Kalmegh solution as an inhibitor consistently reduces corrosion rates across all tested concentrations, with more pronounced effectiveness in NaCl solutions compared to NaOH solutions. Increasing Kalmegh solution concentration from 10 wt% to 30 wt% further reduces corrosion rates, although the impact is less significant in NaOH solutions.

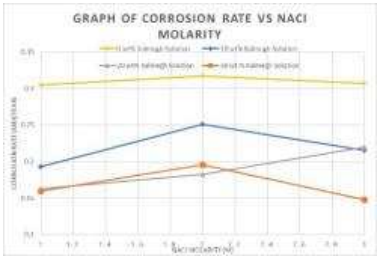

Fig. 1: Graph of corrosion rate against sodium chloride solution molarities.

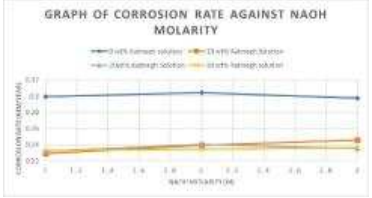

Fig. 2: Graph of corrosion rate against sodium hydroxide solution molarities.

3.2 Polarization Test

The corrosion current density of carbon steel increases up to a peak before decreasing with higher NaCl and NaOH molarity, matching weight loss test results. Polarization tests show that the corrosion rate, which decreases with increasing Kalmegh solution concentration, is cathodically controlled, with extensive reduction reactions occurring due to the influence of oxygen reduction as the rate-determining step.

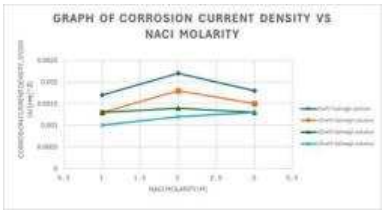

Fig. 3: Graph of corrosion current density against sodium chloride solution molarities.

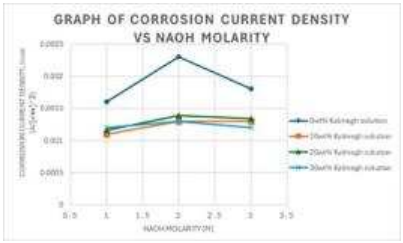

Fig. 4: Graph of corrosion current density against sodium hydroxide solution molarities.

4. Conclusions

This study demonstrates that varying concentrations of NaCl and NaOH influence corrosion rates in a non-linear manner and establishes Kalmegh solution as an effective corrosion inhibitor.

References

1. Groysman, A. (2016). Corrosion problems and solutions at oil refinery and petrochemical units. Topics in Safety, Risk, Reliability and Quality, 37–99. doi:10.1007/978-3-319-45256-2_4
2. Matsushima, I. (2002). Effect of chloride concentration and ph on corrosion of carbon steel and stainless-steel reinforcements. *Zairyo-to-Kankyo*, *51*(10), 463–466. doi:10.3323/jcorr1991.51.463

APPLICATION OF TITANIUM OXIDE THIN FILM ON STRUCTURED HEAT EXCHANGER SURFACE FOR ENHANCING HEAT TRANSFER AND FOULING MITIGATION

Abstract: The paper examines the effectiveness of applying a titanium dioxide coating to prevent fouling in heat exchangers. Fouling is a process that results in greater pressure drop and decreased heat transfer efficiency, leading to higher maintenance expenses. The study seeks to evaluate the coating's efficacy in mitigating fouling resulting from salts and precipitates, as well as investigating its mechanical durability and wettability. The testing procedure consisted of subjecting SS316L specimens, both coated and uncoated, to a CaCO3 saltwater solution for two consecutive runs of 72 hours each. The findings suggest that the specimen with a coating had a reduced occurrence of calcium carbonate deposits and exhibited greater resistance to fouling in comparison to the untreated surface. Furthermore, the coated specimen demonstrated an elevated coefficient of heat transfer, providing evidence for the efficacy of titanium dioxide as a viable remedy for fouling reduction in heat exchangers.

1. Research Background

Fouling is a phenomenon characterized by the deposition of unwanted substances on the surfaces of processing equipment. This is typically caused by the precipitation of soluble salts from water and subsequent crystal growth. Mineral deposits as calcium carbonate calcium sulphate (and silica, are frequently observed in cooling systems, leading to a considerable decline in the surface's ability to transfer heat. The decrease in cross-sectional area results in an increase in pressure drop across the equipment. Fouling has types as crystallization, particulate, chemical reaction, corrosion, biological fouling and solidification. Fouling influencing factor are fluid flow velocity, fluid properties, surface roughness, surface temperature, surface material and pH value. For fouling mitigation coating can be applied to the tubes increase the fouling resistivity thus increase the coefficient of heat transfer over long period of times by decreasing the rate of fouling.

2. Methodology

The experiment consists of two main phases: thermal conductivity testing and fouling assessment. Stainless steel grade 316L specimens, both uncoated and coated with titanium dioxide (TiO_2), were used. The coating was applied using a brush technique and cured at 60°C for 24 hours.

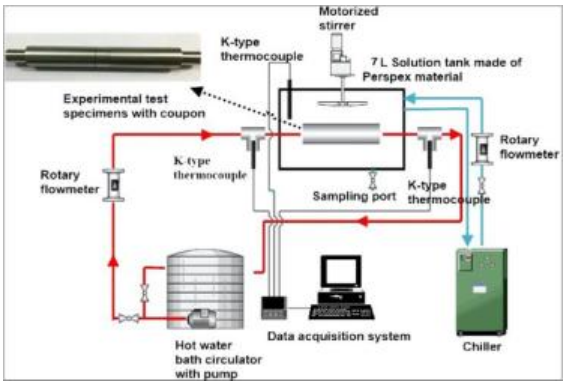

Figure 2.0.1 Experimental Setup for the fouling test rig.

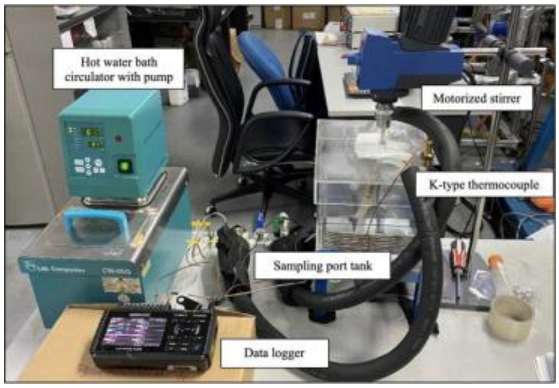

Figure 0.2 Actual Setup of the rig

Experimental Setup: The setup includes a heater, chiller, hot water bath, stirrer, thermocouples, data logger, and flow meters. Hot water at 60°C and cold water at 25°C were circulated through the specimens at 1.2 liters/minute and 2.7 liters/minute, respectively. A 0.3 g/L $CaCO_3$ solution was prepared by mixing calcium chloride and sodium bicarbonate in distilled water. The mixture's concentration was maintained using the EDTA titration method. measuring the temperature difference at intervals to assess thermal conductivity.

The determination of fouling resistance can be derived through utilization of the subsequent equation:

$$R_f = \left(\frac{1}{U_{f}} - \frac{1}{U_{c}}\right) \quad (1)$$

Where, U_f and U_c are the overall heat transfer coefficient for the fouled state and the overall heat transfer coefficient for the initial clean condition, respectively The overall heat transfer coefficients can be calculated using the following equation:

$$Q = U \times A \times \Delta T \quad (2)$$

Where Q is the supplied thermal energy by the heater, A is the area of the outer surface of the test specimen and ΔT is the temperature difference of the inlet and outlet temperatures.

3. Results and Discussions

The results shows that the titanium dioxide specimen has less deposited calcium carbonate compared to the uncoated SS316 L specimen. The amount deposited on the uncoated specimen is 2.561 times the coated one.

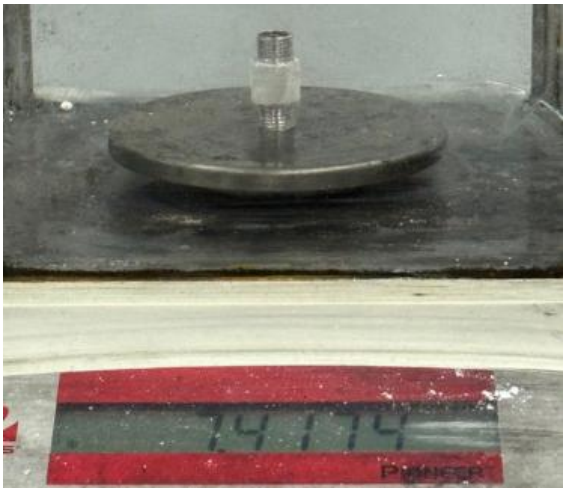

Figure3.1 Final Weigh with deposited CaCO3

	Intial Weight (g)	Final Weight (g)	Weight Depsoited (g)
SS316 L	7.3499	7.5151	0.1652
TiO_2	7.353	7.4175	0.0645

Table 3.1 Deposition after the run by difference in weight.

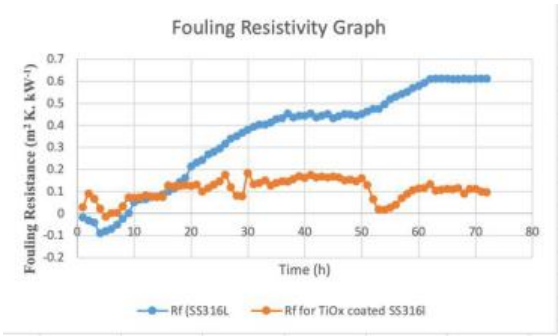

Figure 3.2 Fouling resistivty graph of the 2 specimens

The uncoated SS316 L specimen showed a steady increase in fouling resistance, reaching 0.6 m²K/kW after 60 hours, indicating significant fouling and reduced heat transfer. In contrast, the TiO2-coated

specimen exhibited lower fouling resistance and higher heat transfer coefficients. Notable drops in resistance at hours 27-30 and 50-60 were attributed to surface roughness causing scattered, non-uniform deposition.

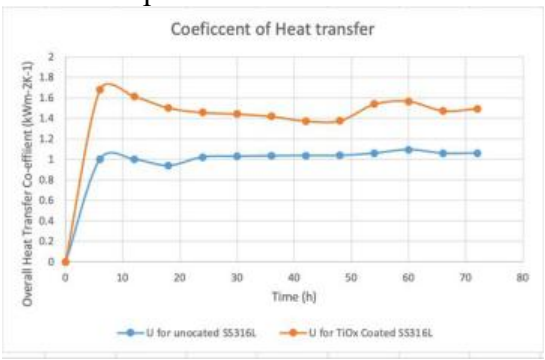

Figure 3.3 Overall Heat transfer coefficient of the 2 specimens

TiO2-coated specimen consistently exhibited a higher overall heat transfer coefficient compared to the uncoated SS316 L specimen. Initially, the coated specimen achieved a peak transfer coefficient of 1.68 kW/m²K. Although fouling caused a decrease, it stabilized at around 1.44 kW/m²K, while the uncoated specimen fluctuated around 1 kW/m²K. The coating's super hydrophilic nature enhances heat transfer by allowing better water contact, resulting in approximately 40% higher conductivity.

4. Conclusions

TiO2 coating significantly enhances the anti-fouling properties and heat transfer performance of SS316 L in a calcium carbonate environment. The coating reduces calcium carbonate deposition, maintains lower fouling resistance, and achieves a higher overall heat transfer coefficient, making it a promising solution for applications requiring efficient thermal management and fouling mitigation.

References

1. Kazi SN. Water-formed deposits fundamentals and mitigation strategies. Koch A, editor. Susan Dennis; 2022.
2. Kazi, S.N. (2018). Fouling and fouling mitigation of calcium compounds on heat exchangers by novel colloids and surface modifications. Rev. Chem. Eng. 36: 653–685.
3. Rodr.guez-Gonz.lez, V., Terashima, C., & Fujishima, A. (2019). Applications of photocatalytic titanium dioxide- based nanomaterials in sustainable agriculture. Journal of Photochemistry and Photobiology C: Photochemistry Reviews, 40, 49–67.
4. Gharbi, K., Benyounes, K., and Khodja, M. (2017). Removal and prevention of asphaltene deposition during oil production: aliterature review. J. Pet. Sci. Eng. 158: 351–360.

CHAPTER 6

Thermal Engineering

Analysis of Heat Transfer for Surface Topology in The Base Surface of Heat Sink

Investigation of Air-Cooling Strategies for Thermal Management of Li-Ion Battery

Comparative Study of Sandblasted and Regular Aluminium Plates on The Cooling Performance of A Thermoelectric Cooler Box

Development of High Conductivity Heat Exchanger Fins and Investigation of Its Heat Transfer

Preface

Effective thermal management is a cornerstone of modern engineering, addressing critical challenges across various applications, from electronics to electric vehicles. This compilation of research highlights innovative approaches to improving heat transfer efficiency, exploring diverse methods to enhance cooling performance and optimize thermal systems. The first study delves into the impact of surface characteristics on heat transfer in heat sinks. By analyzing different surface topologies, it demonstrates how rough surfaces outperform smooth ones, offering higher coefficients of performance (COP) and superior heat dissipation. This work provides practical insights for designing more efficient heat sink surfaces, which are pivotal in electronics and other thermal management systems. The second research focuses on the thermal management of lithium-ion batteries in electric vehicles, proposing enhancements to air-cooled battery thermal management systems (BTMS). Through the development and evaluation of 15 novel designs, it identifies a configuration that improves cooling performance, showcasing the role of innovative design in maintaining battery efficiency and longevity. In the third study, sandblasting is investigated as a surface treatment for aluminum plates in thermoelectric cooler boxes. By enhancing the cold side heat transfer, this work reveals the benefits of increased surface roughness and area, leading to improved cooling performance and energy efficiency. The findings underscore the significance of surface modifications in advancing thermoelectric cooling technologies. Lastly, the fourth study examines copper foam-based heat exchangers for electric vehicle applications. By optimizing fin spacing and pore density, the research explores the relationship between Nusselt number, pressure drop, and heat transfer efficiency. The results highlight the potential of copper foam as a lightweight, high-performance material for thermal management in compact and demanding environments. Collectively, these studies emphasize the importance of innovative materials, surface engineering, and system design in achieving optimal thermal performance. They contribute to the broader goals of sustainability, energy efficiency, and technological advancement in thermal management solutions.

ANALYSIS OF HEAT TRANSFER FOR SURFACE TOPOLOGY IN THE BASE SURFACE OF HEAT SINK

Abstract: This research investigates the impact of surface characteristics on heat transfer efficiency in heat sink applications, focusing on different surface topologies at the base of heat sinks. Smooth surfaces, despite reducing friction, show limited heat transfer, leading to higher power consumption. The study aims to experimentally analyze various surface topologies and evaluate their coefficients of performance (COP). The methodology involves using a Peltier module, DC power supply, data acquisition center, and four thermocouples to measure temperatures at specific points. Experiments are conducted at a constant 1.3A and 6V, with temperature data recorded and analyzed for different heat sinks. Results indicate that rough surfaces consistently exhibit higher COP and better temperature profiles, enhancing heat absorption and dissipation. These findings align with previous studies on the benefits of surface roughness in heat transfer. This research provides insights for designing efficient heat sink surfaces, aiming to improve heat transfer efficiency in diverse engineering applications.

1. Research Background

This research explores the significant role of surface characteristics in determining heat transfer efficiency, particularly in heat sink applications. Smooth surfaces, which reduce friction and enhance fluid flow, often exhibit limited heat transfer due to geometric variations and binding area influences, leading to increased power consumption.

In contrast, surface roughness, quantified by averaging the square of the mean curvature per unit area, can significantly enhance heat transfer.

Studies by Ichimiya et al. (1987), Lu et al. (2020a), and Zhang et al. (2010) have shown that roughness elements, such as those in microchannels, can improve the Nusselt number and global heat transfer performance. However, roughness can also increase flow resistance and pressure drop, with the shape of roughness elements playing a crucial role (2). Historically, Leonardo, Amonton, and Coulomb studied friction concerning loads and surface areas. In 1926, the Bentley racing-car company discovered that their engines with smoother cylinders performed worse due to oil retention issues. Later advancements in surface measurement, standards, and quality control further highlighted the importance of surface roughness (12). Research by Webb et al. (1972), Hall (n.d.), and Turner et al. (n.d.) demonstrated that rough surfaces generally offer better heat transfer performance than smooth ones, especially at low heat fluxes. While smooth surfaces facilitate laminar flow and are easier to clean, they pose challenges in additive manufacturing due to the stair-stepping effect (9).

Conversely, rough surfaces improve adhesion, lubrication, and thermal insulation, beneficial in aerospace and thermal management systems (1,6). This study aims to bridge gaps in understanding experimental analyses on various heat sink surface topologies. By examining thermal management, and the comparative performance of rough and smooth surfaces.

2. Methodology

2.1 Theoretical Background

Coefficient of Performance of Thermoelectric of Peltier Module

Nair M. et al. show that to evaluate the performance of the thermoelectric refrigeration system, the coefficient of performance (COP) will be calculated. The COP is a dimensionless parameter defined as the ratio of the cooling effect or refrigeration rate (Q1) to the power input (W):

$$COP_{ref.} = \frac{Q_1}{W}$$

$$Q_1 = (\alpha_2 - \alpha_1)T_1 I - U(T_1 - T_2) - \frac{1}{2}(I^2)R$$

$$W = (\alpha_2 - \alpha_1)(T_1 - T_2)I + (I^2)R$$

Thus, the original equation becomes :

$$COP_{ref.} = \frac{(\alpha_2 - \alpha_1)T_1 I - U(T_1 - T_2) - \frac{1}{2}(I^2)R}{(\alpha_2 - \alpha_1)(T_1 - T_2)I + (I^2)R}$$

The parameters for Bismuth Telluride in this study, as suggested by Nair M. et al., use Bismuth as material 1 and Tellurium as material 2. Typical values for Bi_2Te_3 at 21°C are presented in the table below.

Table 2.1: Parameters of Bismuth Telluride at 21°C (Nair & Tripathi, n.d.)

Parameters	Value
Seebeck coefficient, α_2 (V/K)	5 X 10^{-4}
Seebeck coefficient, α_1 (V/K)	-7.2 X 10^{-5}
Thermal conductivity, k (W/m K)	1.5
Effective Thermal Conductance, U (W/K)	0.06

2.2 The Experiment Setup

Figure 3.4: Experiment Setup

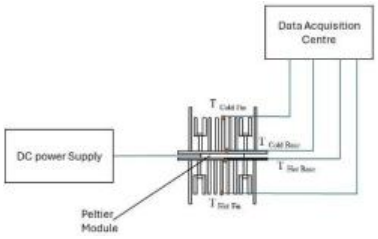

Figure 3.5: Schematic Diagram

The experimental setup comprises a Peltier module, DC power supply, data acquisition center, and four temperature sensors. The Peltier module receives electrical input from the DC power supply. The data acquisition center monitors and collects data, while four thermocouples measure temperatures at specific points on the Peltier module: cold side fin, cold side base, hot side base, and hot side fin.

The experimental procedure involves:

1. Connecting the Peltier module to the DC power supply and temperature sensors to the data acquisition center.
2. Setting the power input to 1.3A and 6V.
3. Monitoring and recording temperature readings at regular intervals.
4. Repeating the process with different heat sinks.
5. Analyzing the collected temperature data to assess thermoelectric performance.

3. Results and Discussions

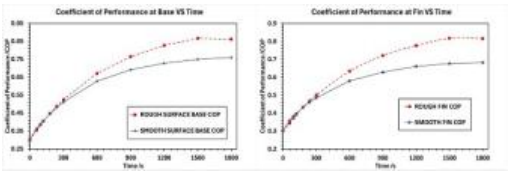

Graph 4.1: Coefficient of Performance Result

Graph 4.1 compares the coefficient of performance (COP) over time for rough and smooth surfaces at both the base and fin locations. For the base surface, the rough surface consistently shows a higher COP than the smooth surface, indicating better heat transfer performance and sustained efficiency over time. This supports findings by Kim et al. (2017) that surface roughness enhances heat transfer due to cavity proliferation.

For the fin surface, the rough surface initially has a lower COP than the smooth surface. However, around the 600-second mark, the rough surface surpasses the smooth surface in COP, becoming more efficient at dissipating heat. This aligns with Nilpueng et al. (2015), who reported that surface roughness improves heat transfer coefficients and pressure drops,

leading to better heat dissipation. Overall, rough surfaces demonstrate superior long- term heat transfer efficiency compared to smooth surfaces.

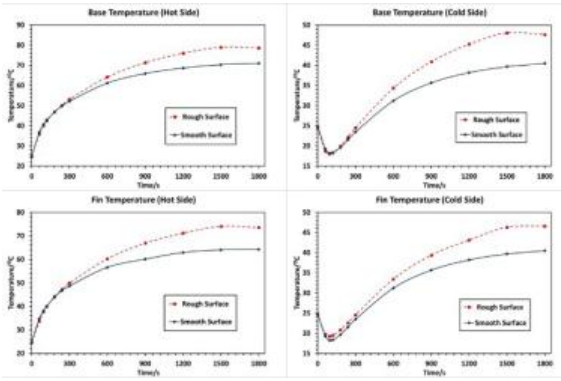

Graph 4.2: Temperature Sensor Data

Graph 4.2 depicts temperature profiles for rough and smooth surfaces at various locations. The rough surface maintains higher temperatures at the hot side base, improving heat absorption, while exhibiting lower temperatures at the cold side base, indicating better heat dissipation. This enhanced thermal performance is crucial for system efficiency and longevity. Similarly, the rough surface demonstrates higher temperatures on the hot side and lower temperatures on the cold side of the fins, facilitating superior heat distribution.

These results underscore the effectiveness of rough surfaces in enhancing heat transfer efficiency, as evidenced by higher COP and favorable temperature distributions. Consistent with prior research, this highlights the advantages of rough surfaces in thermal management, supporting their widespread application in various engineering contexts.

4. Conclusions

The study underscores the superior heat transfer performance of rough surfaces compared to smooth ones in heat sink applications. Experimental results demonstrate consistently higher coefficients of performance (COP) for rough surfaces, corroborating findings by previous studies. Temperature profiles further highlight the enhanced heat absorption and dissipation capabilities of rough surfaces, emphasizing their significance in thermal management.

These findings contribute valuable insights into surface topology's role in heat transfer, aiming to enhance efficiency across diverse applications.

References

1. Bharat Bhushan. (2013). Tribological Components and Applications 12.1
2. García, A., Solano, J. P., Vicente, P. G., & Viedma, A. (2012). The influence of artificial roughness shape on heat transfer enhancement: Corrugated tubes, dimpled tubes and wire coils. Applied Thermal Engineering, 35(1), 196–201. Https://doi.org/10.1016/j.applthermaleng.2011.10.030
3. Hall, W. B. (n.d.). Heat Transfer In Channels Having Rough And Smooth Surfaces.
4. K. Ichimiya Effects of Several Roughness Elements on an Insulated Wall for Heat Transfer From the Opposite Smooth Heated Surface in a Parallel Plate Duct. (1987). http://heattransfer.asmedigitalcollection.asme.org/
5. Kim, J., Jun, S., Lee, J., Godinez, J., & You, S. M. (2017). Effect of Surface Roughness on Pool Boiling Heat Transfer of Water on a Superhydrophilic Aluminum Surface. Journal of Heat Transfer,139(10). https://doi.org/10.1115/1.4036599
6. Michael F. Ashby. (2013). Materials Engineering, Science, Processing and Design
7. Nair, M., & Tripathi, B. (n.d.). Experimental Studieson Thermoelectric Refrigeration System. https://www.researchgate.net/publication/332752147
8. Nilpueng, K., & Wongwises, S. (2015). Experimental study of single-phase heat transfer and pressure drop inside a plate heat exchanger with a rough surface. Experimental Thermal and Fluid Science, 68, 268–275. Https://doi.org/10.1016/j.expthermflusci.2015.04.009
9. Pan, Y., Zhao, X., Zhou, C., & Chen, Y. (2012). Smooth surface fabrication in

mask projection based stereolithography. Journal of Manufacturing Processes, 14(4), 460–
470.
https://doi.org/10.1016/j.jmapro.2012.
09.003

10. Turner, A. B., Hubbe-Walker, S. E., & Bayley, F. J. (n.d.). Fluid ¯ow and heat transfer over straight and curved rough surfaces. www.elsevier.com/locate/ijhmt
11. Webb, R. L., & Eckert, E. R. G. (1972). Application Of Rough Surfaces To Heat Exchanger
Design. In Int. 1. Heat Mass Transfer (Vol. 15). Pergamon Press.
12. Whitehouse, D. J. (n.d.). Surface Characterization and Roughness Measurement in Engineering.
13. Zhang, C., Chen, Y., & Shi, M. (2010). Effects of roughness elements on laminar flow and heat transfer in microchannels. Chemical Engineering and Processing: Process Intensification, 49(11),1188–1192.
https://doi.org/10.1016/j.cep.2010.08. 022

INVESTIGATION OF AIR-COOLING STRATEGIES FOR THERMAL MANAGEMENT OF LI-ION BATTERY

Abstract: Lithium-ion (Li-ion) batteries heat up during charging and discharging due to chemical reactions and charge transfer inside the battery. An air-cooled battery thermal management system (BTMS) is widely used in electric vehicles (EVs). Air-cooled BTMS was chosen due to its simple design, low cost, lightweight, long-life, and easy to maintain. In this work, a T-type BTMS with additional cooling outlet was investigated. Cooling outlet in-line with cooling channels was added to the BTMS. The Bernardi equation was used to calculate heat generated by battery during discharge. A total of 15 novel designs have been developed in this study. It was found that adding cooling channel in line with the cooling channel was unable to reduce the battery temperature further. Design 3, design with inlet at the top of BTMS performs the best of all designs. The temperature was able to drop 2K and 1.3K for maximum and average respectively.

1. Research Background

Li-ion batteries are essential in our daily lives. Portable energy storage, portable electronics and even vehicles have adopted the usage of Li-ion batteries. Some of the vehicles also are now battery powered. The battery has an optimum battery temperature of 15°C to 35°C (1).

However, Li-ion battery produces heat during charging and discharging. This heat generation may lead to overheating, thermal runaway, and fire (2). Thermal runaway is the state in which high temperatures cause heat-producing exothermic reactions and may raise the temperature enough to cause more harmful reactions (3).

There are several ways to cool the battery. Air cooling, liquid cooling and using phase change material are mainly the ways to cool the battery. In this study, the battery is being cooled by air as it is the most popular choice for cooling batteries in Electric Vehicle (EV) (4). It also provides straightforward design, low in cost, lightweight, long-life span, and ease of maintenance.

The objective of this study is to analyze the airflow configuration with different openings and to investigate the effectiveness of the novel designs with conventional T-type by numerical method. T-type was chosen as it has better performance compared to Z and U-type (5). T-type is a symmetrical Battery Thermal Management System (BTMS). Symmetrical BTMS has better performance compared to asymmetrical one (6).

2. Methodology

A total of 24 18650 cylindrical cells were used in 4mm spacing and 20 cells in 10 mm spacing. The 4 mm spacing designs were used in 2-dimension (2D) simulation while 10mm spacing was used for 3-dimension (3D) simulation. A total of 15 novel designs have been developed with notable designs are Design 3 and Design 4. In Design 3, the inlet was placed on top of the BTMS, while in Design 4, the wall of outlet plenum was brought closer to the battery. All 10mm spacing designs have laminar inlets.

The battery that had been referenced was manufactured by LG, with the model LG INR 18650 MJ1 with capacity of 3.5 Ah. Bernardi equation was used to calculate

battery heat generation. The heat generation rate was set to the highest value calculated before. The values are 11260.7 W/m^3, 22521.4 W/m^3, and 45042.8 W/m^3 for discharge rate of 0.5C, 1C and 2C respectively. The Bernardi equation is given as [7].

$$Q = I(U.V) - IT\frac{\partial U}{\partial T} \qquad (1)$$

where heat generation rate by the battery, I, current in amps (A), U, open-circuit voltage (V), V, terminal voltage (V) and $\frac{\partial U}{\partial T}$ is entropic coefficient. Fig. 1 shows the calculated heat generated at different states of charge (SOC) for different discharging rates.

Flow simulation had been done for Basic T- type, Design 1,2 and 3. The flow simulation was done using SolidWorks. The 2D and 3D numerical method was done using Ansys Fluent. The inlet air velocity is set to 1 m/s. The air temperature is 300 K. All air properties were obtained from Ansys Fluent.

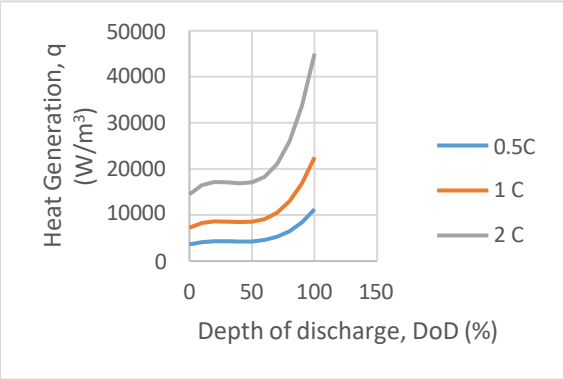

Fig. 1: Calculated battery heat generation at different discharge rates.

3. Results and Discussions

The 2D simulation was done in steady state. The simulation should be done in transient to achieve more accurate results. For 3D simulation, the time setting is set to transient, with the length of simulation set to 30 minutes. The heat generation that was used in this simulation for all designs is 1C.

Table 1: Result of 10 mm spacing with laminar inlet.

Design	Maximum temperature, T_{max} (K)	Average temperature, T_{ave} (K)	Pressure Drop (Pa)
Basic T-type	312.11	310.03	0.138
Design 1	313.17	310.629	0.102
Design 2	313.36	310.808	0.074
Design 3	310.02	308.812	0.093
Design 4	311.49	309.659	0.323
Design 5	313.46	312.617	0.091
Design 6	312.07	309.595	0.125
Design 7	313.8	311.917	0.079
Design 8	313.1	311.626	0.137
Design 9	314.07	311.907	0.103
Design 10	313.72	311.976	0.099
Design 11	314.02	312.076	0.129
Design 12	313.76	311.989	0.110
Design 13	313.56	311.866	0.138
Design 14	313.14	311.884	0.135
Design 15	314.47	312.334	0.192

For Designs 1 and 2, both maximum and average temperatures are higher than the Basic T-type due to insufficient air interaction with the battery. The pressure drops in these designs are lower. Design 3 exhibits the best performance, reducing maximum and average temperatures by 2K and 1.3K, respectively, as it allows more air to contact the battery surface.

Design 4 achieves a temperature reduction of 0.59K (maximum) and 0.46K (average)

by directing air through a secondary channel, significantly cooling the last row of the battery array. In Design 5, maximum and average temperatures increase by
1.38K and 2.5K, respectively, because the air does not fully contact the battery. Design 6 shows minimal temperature reduction with a lower pressure drop.

Design 7's air distribution is good, but insufficient air in the secondary channel limits temperature reduction. Design 8 has higher temperatures (1.02K maximum and 1.51K average) due to poor airflow in the outer rows. Designs 9 through 13 concentrate air in the middle channel, leading to poorer performance than the Basic T-type. Designs 12 and 13 aimed for uniform temperature distribution by adding an additional outlet. In Designs 14 and 15, inadequate air reach causes higher battery temperatures in some areas.

4. Conclusions

In this study, it was found that:

a) Adding additional cooling outlets in line with cooling channel was unable to reduce the battery temperature even further. The air was unable to interact with the battery to remove the heat.
b) Cooling the battery in axial air flow performs the best of all designs. This is due to the air having more surface area to remove heat from the battery. The air was able to flow through the secondary channel, which was unable to accomplish by cooling the battery radially. This design also has the highest calculated Nusselt number.
c) The influence of forcing air into secondary is big. This was accomplished in Design 4, where the air was forced to flow through the secondary channel but resulted in a higher pressure drop.

References

1. Pesaran, A., Santhanagopalan, S., & Kim, G. (2013). Addressing the Impact of Temperature Extremes on Large Format Li-Ion Batteries for Vehicle Applications. Ft. Lauderdale, Florida.
2. Mevawalla, A., Panchal, S., Tran, M.-K., Fowler, M., & Fraser, R. (2021). One dimensional fast computational partial differential model for heat transfer in lithium- ion batteries. *Journal of Energy Storage*.
3. Bandhauer, T. M., Garimella, S., & Fuller, T. F. (2011). A Critical Review of Thermal Issues in Lithium-Ion Batteries. *Journal of The Electrochemical Society*.
4. Sharma, D. K., & Prabhakar, A. (2021). A review on air cooled and air centric hybrid thermal management techniques for Li-ion battery packs in electric vehicles. *Journal of Energy Storage*.
5. Zhang, F., Yi, M., Wang, P., & Liu, C. (2021). Optimization design for improving thermal performance of T-type air-cooled lithium-ion battery pack. *Journal of Energy Storage*.
6. Chen, K., Chen, Y., She, Y., Song, M., Wang, S., & Chen, L. (2020). Construction of effective symmetrical air-cooled system for battery thermal management. *Applied Thermal Engineering*.
7. Bernardi, D., Pawlikowski, E., & Newman, J. (1985). A General Energy Balance for Battery Systems. *Journal of The Electrochemical Society*.

COMPARATIVE STUDY OF SANDBLASTED AND REGULAR ALUMINIUM PLATES ON THE COOLING PERFORMANCE OF A THERMOELECTRIC COOLER BOX

Abstract: This research investigates the effect of sandblasting surface treatment on a cold side aluminum plate for improving the cooling performance of a thermoelectric cooler box, compared to an untreated plate. While existing research focuses on enhancing hot side heat dissipation or optimizing thermoelectric module materials, this study aims to improve cold side heat transfer, which is rarely explored. Two setups are compared - one with a regular untreated aluminum plate and another with a sandblasted plate on the cold side of the thermoelectric module. Temperatures at various points and voltage drops across the module are measured over 60 minutes. Surface morphology is analyzed using scanning electron microscopy. Results show the sandblasted plate achieves 1.5°C lower temperature, extracts 156.65J more heat from the plate and 547.65J more from the coke can, uses 0.2V less voltage, and has a higher COP of
0.027 compared to 0.025 for the untreated plate. Micrographs reveal increased surface area and roughness on the sandblasted plate enhancing heat transfer.

1. Research Background

Thermoelectric coolers (TECs) are solid-state devices that enable cooling based on the Peltier effect and are widely used due to their compact size and lack of moving parts or refrigerants [1]. However, TECs have limitations such as lower efficiency compared to vapor compression cycles and limited cooling capacity [2, 3]. Thermoelectric refrigeration utilizes TECs to absorb heat and provide cooling. Less focus has been given to improving heat transfer on the cold side of the thermoelectric refrigerator or cooler box [4]. Surface treatment presents an opportunity to modify the surface conditions of materials like the aluminum plates used as cold side heat exchangers in TEC cooler boxes. The proposed surface treatment method of sandblasting can increase the effective surface area [5] and roughness [6, 7], which may lead to improved heat transfer through the TEC module and out of the cooler box.

2. Methodology

The two experimental setups for this comparative study are

- Setup 1 – Regular aluminium plate
- Setup 2 – Sandblasted aluminium plate

Each setup consists of a 25.08L polystyrene cooler box with a thermoelectric set fit into the side of the box with the aluminium plate directly connected to the cold side of the thermoelectric module with HY510 thermal grease as a thermal interface material. 4 thermocouples are attached to the hot side fan, hot side heatsink, cold side aluminium plate, and a coke can. A data acquisition device, NI-9211 is used to measure and record thermocouple temperatures for the duration of the experiments.

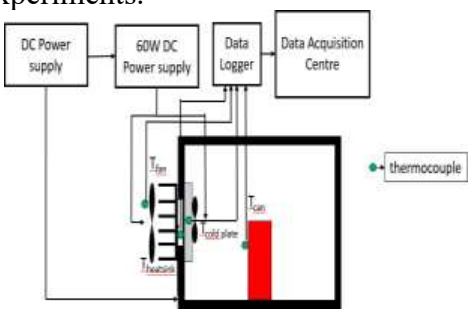

Fig. 1: Schematic diagram of experimental setup

The improvement in cooling of the sandblasted aluminium plate is measured. The power consumption of the thermoelectric module is also compared between the untreated and sandblasted aluminium plates by recording the voltage drop of the thermoelectric module power supply. The heat extracted from each aluminium plate and coke can in each setup, and the corresponding coefficient of performance are calculated using the equations

$$Q = m \times C_p \times (\Delta T) \quad (1)$$

The coefficient of performance of the thermoelectric cooler box can be calculated from the heat extracted from the coke can divided by the work input to the thermoelectric module given by the equation below

$$COP = \frac{Q_{cooling}}{W_1} \quad (2)$$

$$COP = \frac{m \times C_p \times (\Delta T)}{V \times I \times t} \quad (3)$$

The two aluminium plates are scanned under a scanning electron microscope (SEM) to obtain the surface morphology at a μm scale. The visual difference in surface roughness and area between the untreated and sandblasted surfaces is discussed.

3. Results and Discussions

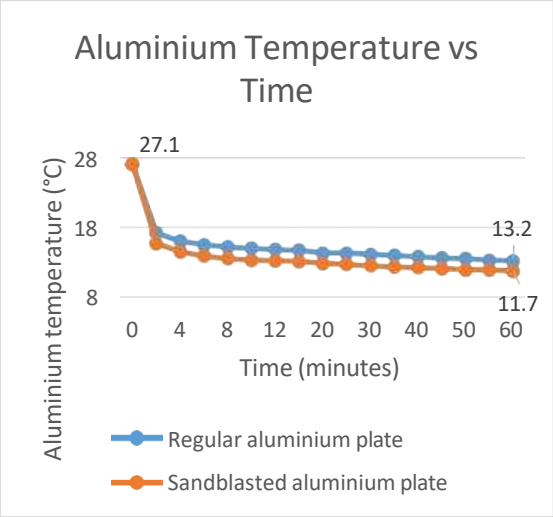

Fig. 2: Graph of aluminium temperature against time for both regular and sandblasted plates

Figure 2 shows the comparison of the temperature of the regular and sandblasted cold side aluminium plates after 60 minutes of cooling of the thermoelectric cooler box. An improvement of 1.5°C is achieved by using the sandblasted aluminium plate, indicating the enhanced heat transfer from the cold side plate to the thermoelectric module.

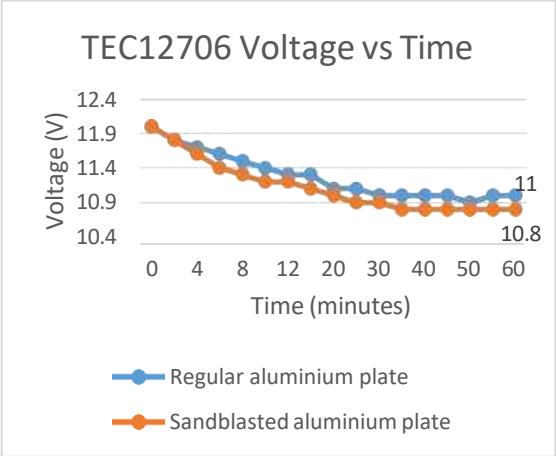

Fig. 3: Graph of voltage drop of power supply for thermoelectric module for each aluminium plate

Figure 3 shows the voltage drop of the power supply that is connected to the thermoelectric module over 60 minutes of operation, with the thermoelectric module in setup 2 showing a consistent difference of 0.2V less than in setup 1, indicating a reduced power consumption and higher efficiency by using the sandblasted aluminium plate over the regular plate as the current supplied is constant at 6A.

Table 1: Heat extracted from aluminium plate and coke can

Type	Heat Extracted (J)
Regular Aluminium Plate	1030.38
Sandblasted Aluminium Plate	1187.03
	Difference = 156.65
Coke Can in Setup 1	6570.72
Coke Can in Setup 2	7118.28
	Difference = 547.65

From Table 1, the heat extracted from the sandblasted plate is 156.65J more than the regular plate, while the heat extracted from the coke can in the setup using sandblasted plate is 547.65J more than in the setup using the regular plate.

Table 2: Coefficient of performance of each thermoelectric cooler box setup

Thermoelectric Cooler Box Setup	Coefficient of Performance
Setup 1, regular Aluminium	0.025
Setup 2, sandblasted aluminium	0.027

From Table 2, an improvement of 0.002 in coefficient of performance is achieved by using the sandblasted plate. The minimal improvement can be explained by the minimal change in temperature difference from the additional 1.5°C cooling, and the lower efficiency of the cooler box design in facilitating the convective heat transfer from the coke can to the aluminium plate.

Fig. 3: SEM image of the the regular aluminium

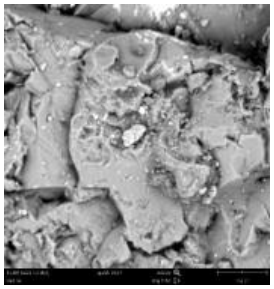

Fig. 4: SEM image of sandblasted aluminium

From Figure 3 and 4, there is an apparent difference in the surface morphology of the two plates whereby the sandblasted surface has more peaks and valleys, leading to an increase in surface area for better heat transfer.

4. Conclusions

The results have shown that performing sandblasting surface treatment on the cold side aluminium plate of a thermoelectric cooler box has improved its cooling capabilities due to the increased surface roughness and surface area leading to better heat transfer from the plate to the thermoelectric module.

References

1. Rowe, D. M. (Ed.). (2018). Thermoelectrics and its energy harvesting: Materials, preparation, and characterization (2 volumes). CRC Press.
2. DiSalvo, F. J. (1999). Thermoelectric cooling and power generation. Science, 285(5428), 703-706. https://doi.org/10.1126/science.285.5428.703
3. Zhao, D., & Tan, G. (2014). A review of thermoelectric cooling: Materials, modeling and applications. Applied Thermal Engineering, 66(1-2), 15-24.https://doi.org/10.1016/j.applthermaleng.2014.01.074
4. Manzagol, J., & Hosseinizadeh, S. F. (2018). Optimization of thermoelectric cooling systems using genetic algorithm. Applied Thermal Engineering, 141, 604-613.
5. Zhang, Y., Chen, L., & Liu, X. (2019). Enhancing effective surface area through sandblasting: A comprehensive study. *Surface Engineering, 35*(4), 279-286.
6. Kim, S., Jeong, J., & Ryu, S. (2018). Effects of sandblasting on surface roughness and adhesion. *Journal of Materials Processing Technology, 256*, 65-72.
7. Lee, H., & Park, D. (2020). Surface roughness improvement by sandblasting: Experimental analysis. *Surface and Coatings Technology, 403*, 126405.

DEVELOPMENT OF HIGH CONDUCTIVITY HEAT EXCHANGER FINS AND INVESTIGATION OF ITS HEAT TRANSFER

Abstract: Due to the increase of demand in electric vehicles due to its benefits compared with internal combustion engine vehicle, the concern for thermal management for electrical components like batteries, electric motors, and power electronics to maintain its optimum operating temperature in different climates. So, the heat exchanger for this application needs to have high heat transfer rate while being lightweight and smaller size. This study focuses on developing a heat exchanger with copper foam due to higher thermal conductivity than aluminum and lower density due to the porous structure. The heat transfer performance and pressure drop are investigated for 20 and 40 PPI also with fin spacing of 10- and 15-mm. The test is done in a square duct subjected to forced convection heat transfer with air as the fluid. Nusselt number of each parameter is compared. Nusselt number for 40 PPI increase 8.8 % and
28.5 % compared to 20 PPI for 10 and 15 mm spacing respectively while Nusselt number for 15 mm spacing increases 66.3 % and 71.5 % compared to 10 mm spacing for 20 and 40 PPI respectively. Pressure drops and friction factor for 10 mm spacing is higher than 15 mm spacing. The 10 mm spacing has lower Nusselt number than 15 mm spacing although having a greater number of fins, which 10 mm spacing have 12 fins and 15 mm spacing give 9 fins. The increase of spacing will increase Nusselt number until optimum then it will drop gradually due to the increase of difficulty for air to pass through the heat exchanger.

1. Research Background

The global trend of autonomous electric vehicles is accelerating at breakneck speed. Report Allied Market Research by forecast that self-driving electric vehicle market to reach 5 trillion USD in 2031 from 0.23 trillion USD in 2021, registering a CAGR of 36.3 % [1]. One of the challenges of autonomous electric vehicles is thermal management. Many components like electric motors, power electronics and batteries have their own optimum thermal requirements. So, the heat exchanger needs to be designed to achieve sufficient heat transfer rate while being lightweight and smaller size.

Currently, researchers have shown interest in the development of porous materials, commonly called metal foam in HXs applications. Metal foam is a solid metal with a porous structure comprising a large portion of the volume. It can be up to 90 % porosity, which leads to very low specific weight. As the specific weight is very low, higher thermal conductivity materials can be used despite the increase of its density. Open-cell metal foam suitable in HXs applications because of this high surface area to volume ratio, high thermal conductivity (depending on materials), and tortuous flow path that may increase the convective heat transfer. So, the design of the metal foam needs to compromise between the heat transfer rate and pressure drop as pressure drop will increase the needs of pumping power.

This study aims to develop a heat exchanger with copper foam as its fins, with different PPI and fin spacing, and investigate the heat transfer performance and pressure drop in forced application.

2. Methodology

Two types of heat exchangers configuration are developed, which is for 10- and 15 mm spacing. The wall

temperature of every fin at the same length from the heat source is measured to determine its consistency.

Table 1: *List of components for heat exchangers.*

Component	Dimension	Manufacturer
Open-cell copper foam	200 × 5 × 20 mm	Linyi Gelon LIB Co. Ltd.
Aluminum housing	240 × 200 × 32 mm	Lian Giap & Co. Sdn. Bhd.
Thermal grease	k = 12.8 W/mK	Maxtor
Cartridge heater	D = 10 mm, L = 200 mm	Maltec

Fig. 2.1: *Heat exchangers setup. (20 PPI, 15 mm spacing)*

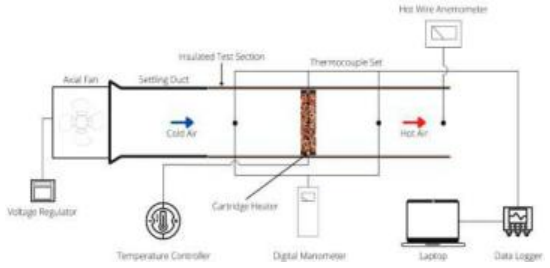

Fig. 2.2: *Schematic diagram of experimental setup.*

First, the temperature controller is set to 80 °C. Second, the velocity of the fan is set to 60 V. Third, the heater is turned on and the temperature data of the 6 points at the wall plus inlet and outlet temperature is collected. Fourth, the velocity and pressure are collected at 9 different points of cross- area section of duct. Lastly, the experiments are repeated for 70, 80, 90 and 100 V.

Table 1: *List of measurement tools*

Measurement tool	Range and resolution	Accuracy (%)
Exposed Welded Tip K-Type Thermocouple	-75 – 260 °C	0.75
Omega USB TC0-08 DAQ	-270 – 2820 °C, 20 bit	-
GM8903 hot wire anemometer	0 – 30 m/s	-
Testo 521-1 manometer + Testo 0635 2145 L-type pitot tube	0 – 100 hPa, 0.01 hPa	±0.2

List of formula used for the calculation is Reynolds number:

$$Re = \frac{\rho V D_h}{\mu}, \quad \text{..... (1)}$$

heat transfer coefficient:

$$h = \frac{\dot{m} c_p (T_o - T_{in})}{A(T_w - T_b)}, \quad \text{..... (2)}$$

bulk mean temperature:

$$T_b = \frac{T_o - T_{in}}{2}, \quad \text{..... (3)}$$

Nusselt number:

$$Nu = \frac{h D_h}{k}, \quad \text{..... (4)}$$

pressure drop:

$$\Delta P = P_{in} - P_{out}, \quad \text{..... (5)}$$

and friction factor:

$$f = \frac{\Delta P}{4(\frac{L}{D_h})(\frac{\rho v^2}{2})}, \quad \text{..... (6)}$$

3. Results and Discussions

Fig. 4.3 shows that Nu increases with the increase of PPI based on both with spacing of 10- and 15-mm, as expected. At Re of 20000, Nu for 40 PPI increase 8.8 % and 28.5 % higher than its 20 PPI for 10 and 15 mm spacing respectively. The increase in heat transfer coefficient may be because of the increase of surface area for heat transfer and/or because of the decrease in the thickness of boundary layer due to decrease in length between ligaments that promote flow mixing. Nusselt number is higher for 15 mm spacing compared to 10 mm spacing for both 20 and 40 PPI. At Re of 20000, Nu for 15 mm spacing increase 66.3 % and 71.5 % for 20 and 40 PPI respectively. Early hypotheses expected that the Nusselt number for 10 mm spacing is higher than 15 mm spacing due to the increase of surface area for heat transfer

due to the increase of number of fins. However, Feng et al. have found that there is an optimum amount of open slot width that gives maximum heat transfer coefficient. Heat transfer coefficient will increase with the increase with the increase in open slot width until optimum then, it will decrease gradually. This is due to the increase of difficulty for the air to pass through the heat exchanger.

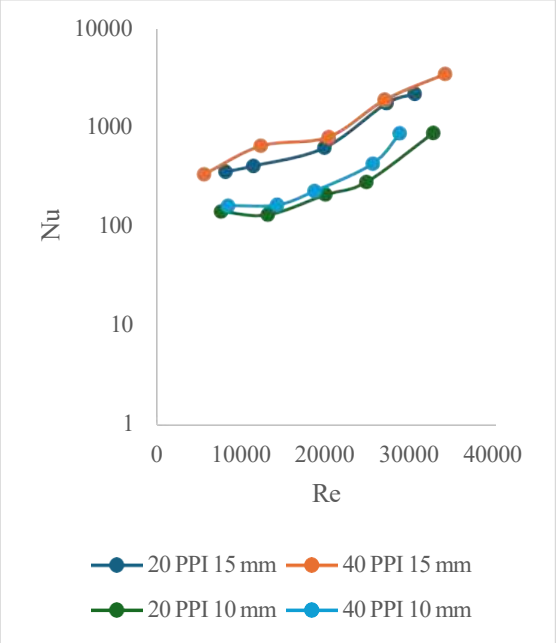

Figure 0.1: *Graph Nusselt number VS Reynolds number for 20, 40 PPI and 10-, 15-mm spacing.*

Fig. 4.4 shows the pressure drop across the heat exchanger with Reynolds number. Fig. 4.5 shows the friction factor across different Reynolds numbers. In general, a heat exchanger with 10 mm spacing has a higher pressure drop and friction factor compared to a heat exchanger with 15 mm. However, the result is not highly accurate and may be due to the low accuracy of the pressure measurement device, which only measures 2 decimal points for hPa.

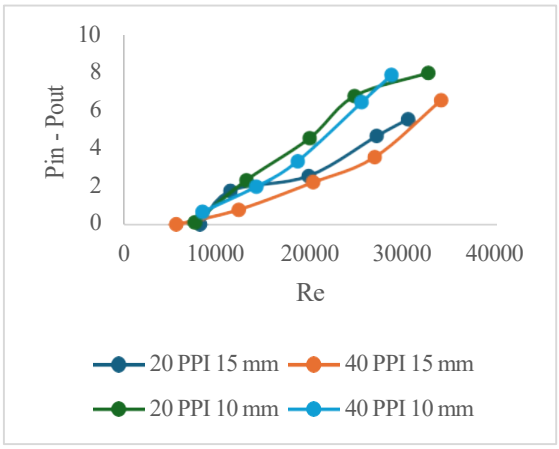

Figure 0.2: *Graph pressure difference VS Reynolds number for 20, 40 PPI and 10-, 15-mm spacing.*

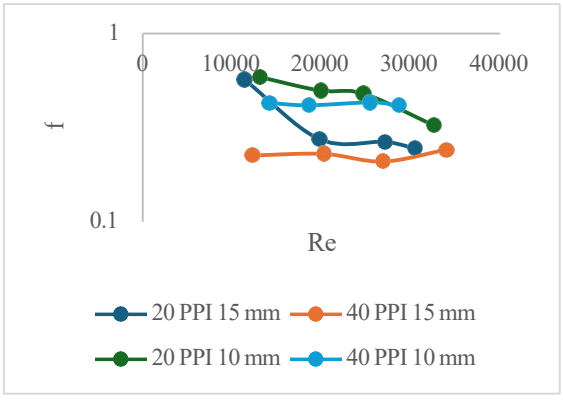

Figure 0.5: *Graph friction factor VS Reynolds number for 20, 40 PPI and 10-, 15-mm spacing.*

4. Conclusions

Heat transfer performance and pressure drop have been analyzed. Nu increases with the increase in PPI and increase in fin spacing. There is expected to have an optimum fin spacing that gives maximum Nu. Pressure drop and friction factor increases with the increase of PPI and decrease of fin spacing.

References

1. Kamble, S. J., & Katare, L. J. (2023). Self-Driving Electric Vehicle Market Size, Share, Competitive Landscape and Trend Analysis Report by Level of Automation, by Vehicle Type, by Type: Global Opportunity Analysis and Industry Forecast, 2021-2031. *Allied Market Research*.

CHAPTER 7

Energy Engineering

Implementation of Low Head In-Pipe Hydropower System for Building Cooling Water Network

Development and Implementation of A Novel Hybrid Evaporative- Radiative Cooling PV Module

Experimental Evaluation of Vacuum Insulated Panel in Thermoelectric Cooling

Analysing Semiconductor Wafer Annealing in Heated Furnace

Preface

As sustainability and efficiency take center stage in modern engineering, innovative solutions are needed to tackle energy challenges and optimize industrial processes. This collection of research explores cutting-edge approaches in renewable energy, thermal management, and semiconductor manufacturing, emphasizing the importance of innovation and precision in addressing contemporary technological demands. The first study introduces a novel low-head in- pipe hydropower system capable of harnessing energy from water flowing through pipes. By employing advanced design tools, 3D printing technology, and rigorous testing, this system achieves high efficiency, reaching up to 93.57% under optimal conditions. This research highlights the potential of such systems in sustainable energy generation for low-head applications. The second research focuses on enhancing the efficiency of photovoltaic (PV) modules, addressing the issue of thermal-induced performance decline. By evaluating various cooling techniques, the study identifies natural cotton cooling pads as the most effective, achieving significant temperature reductions. The findings contribute to developing adaptable and cost-effective cooling solutions for PV systems, improving their real-world applicability and energy output. In the third study, vacuum insulation panels (VIPs) are utilized to improve the thermal performance of thermoelectric cooling systems. Experimental results demonstrate that VIPs significantly enhance insulation, achieving a 27.44% reduction in heat transfer and lowering the minimum temperature in the cooling system. This work underscores the potential of advanced insulation technologies in boosting energy efficiency and cooling performance. Lastly, the fourth paper examines wafer deformation in semiconductor manufacturing, a critical challenge in producing reliable and high- performance devices. Using Finite Element Analysis (FEA), the study investigates the effects of copper thin film thickness and annealing temperatures on wafer deformation. The findings provide valuable insights for optimizing manufacturing processes to minimize stress-induced defects, ensuring better yield and reliability in the semiconductor industry. Together, these studies represent significant strides toward sustainable energy solutions, advanced thermal management, and precision in manufacturing, offering valuable contributions to diverse engineering fields.

IMPLEMENTATION OF LOW HEAD IN-PIPE HYDROPOWER SYSTEM FOR BUILDING COOLING WATER NETWORK

Abstract: This study introduces an innovative low-head in-pipe hydropower system designed to capture energy from water flowing through pipes efficiently. The test rig, tailored for low-head conditions, uses a variable speed drive (VSD) to adjust the water pump speed. The nozzle and turbine blades are designed using SolidWorks, with stress distribution analysis ensuring the PLA material's structural integrity. Fabricated with a 3D printer, the nozzle with a 0.5 diameter ratio is selected for its ability to exert the highest force while maintaining a stable flow. The turbine system, comprising twelve blades, operates with flow rates from 0.0891 L/s to 6.086 L/s. System parameters are measured using a digital tachometer, flowmeter, and pressure gauge. Results indicate that efficiency increases with flow rate, peaking at 91.85% at 3.981 L/s and 0.5 bar indicates the low-head applications, and reaching 93.57% at higher flow rates and pressures. Variations in efficiency may arise from flow condition changes or minor misalignments. Overall, the system demonstrates high efficiency and potential for sustainable energy generation under low-head conditions.

1. Research Background

This research explores the potential of In-Pipe Hydropower Systems (IPHS) to convert flowing water in pipelines into renewable energy. IPHS harnesses kinetic energy from water within pipes to generate clean electricity, integrating seamlessly with existing infrastructure [1]. Key design elements, like blade count and nozzle configurations, ensure optimal energy extraction. IPHS is versatile, suitable for agriculture, urban development, and cooling water network.

Low-head turbines increase the efficiency of the system and are useful in low-flow conditions [2]. In addition to lowering operating expenses and carbon footprints, IPHS supports international initiatives for sustainable energy. The usefulness and ecological advantages of IPHS in converting water distribution networks into renewable energy sources are highlighted in this study.

2. Methodology

A test rig simulating an IPHS with a 3"-inch PVC pipe and turbine was designed. Stagnation pressure, flowrate, and water velocity were measured using a Variable Speed Drive (VSD). Various nozzles and turbine blades were 3D printed from PLA. Tests determined the optimal nozzle, and experiments analyzed mechanical power, hydraulic power, and system efficiency.

Fig. 1. shows the setup of this research. Only within the red section is used in conducting the experiment.

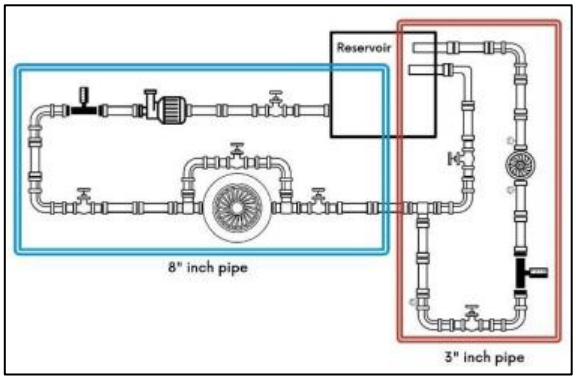

Fig. 1. Layout of experimental setup of low head system

The important parameters that significantly affect the turbine performance are flowrate,
Q, jet velocity, V_j and turbine velocity, u. Assuming incompressible flow and neglecting pipe and nozzle friction,

mechanical and hydraulic power can be calculated using these parameters, as shown in Equation 1 and Equation 2.

$$P_{mechanical} = [2\rho Q(V_j - u)]u \ldots (1)$$

$$P_{hydraulic} = \frac{1}{2}\rho Q V_j \ldots\ldots\ldots\ldots (2)$$

$$n_T = \frac{P_{mechanical}}{P_{hydraulic}} \times 100\% \ldots\ldots\ldots\ldots (3)$$

The overall efficiency, n_T of the turbine can be evaluated as the ratio between the mechanical power and hydraulic power using Equation 3.

3. Results and Discussions

The research aims to determine the most efficient nozzle and turbine design for low- head in-pipe hydropower systems and evaluate their mechanical power, hydraulic power, and system efficiency.

Fig. 2. shows that as the nozzle diameter ratio increases from 0.5 to 0.8, the force exerted decreases from 14.764 N to 6.533 N. The pressure before the nozzle stays at 0.2 bar, while the pressure after the nozzle is higher at a 0.5 diameter ratio (0.15 bar) compared to 0.1 bar for other ratios. The 0.5 diameter ratio nozzle is most effective, balancing force and downstream pressure efficiently.

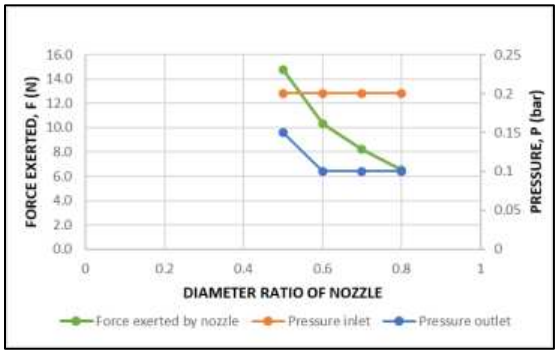

Fig. 2. Graph force exerted and pressure against diameter ratio of nozzle

Fig. 3. illustrates that mechanical power starts at 2.801 L/s (7.349 W) and peaks at 81.120 W at 6.086 L/s. Hydraulic power increases from 0 W to 86.691 W. Turbine efficiency rises from 0% at low flowrates to 93.57% at 6.086 L/s, with minor fluctuations. High efficiency at increased flowrates demonstrates the turbine system's viability for energy generation, highlighting the importance of optimizing flow conditions and turbine design for maximum efficiency.

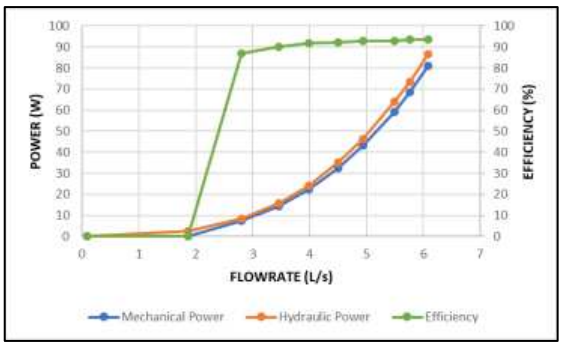

Fig. 3. Relationship between mechanical power, hydraulic power, efficiency and flowrate

4. Conclusions

In conclusion, this project identified the optimal 0.5 nozzle diameter ratio and turbine design for low-head in-pipe hydropower systems. Hydraulic power increased with flowrate, peaking at 81.120 W and 93.57% efficiency at 6.086 L/s. For low-head applications, the system achieved
22.285 W and 91.85% efficiency at 3.981 L/s and 0.5 bar pressure. These results underscore the importance of optimizing flow and nozzle design to maximize energy extraction, which supports the in-pipe hydropower's potential for sustainable energy. Future research should refine designs for improved performance.

References

1. Casini, M. (2015). Harvesting energy from in-pipe hydro systems at urban and building scale. *International Journal of Smart Grid and Clean Energy*, *4*(4), 316-327.
2. Date, A., Date, A., & Akbarzadeh, A. (2013). Investigating the potential for using a simple water reaction turbine for power production from low head hydro resources. *Energy Conversion and Management*, *66*, 257-270.